Title

Development of Simons Array Optics for Cosmic Microwave Background Polarimetry

Author

Jeong, Oliver

Publication Date

2021

Development of Simons Array Optics for Cosmic Microwave Background Polarimetry

by

Oliver Jeong

A dissertation submitted in partial satisfaction of the

requirements for the degree of

Doctor of Philosophy

in

Physics

in the

Graduate Division

of the

University of California, Berkeley

Committee in charge:

Professor Adrian Lee, Chair
Professor William Holzapfel
Professor Aaron Parsons

Fall 2021

Development of Simons Array Optics for Cosmic Microwave Background Polarimetry

Abstract

Development of Simons Array Optics for Cosmic Microwave Background Polarimetry

by

Oliver Jeong

Doctor of Philosophy in Physics

University of California, Berkeley

Professor Adrian Lee, Chair

Precision measurements of the cosmic microwave background (CMB) polarization anisotropies provide a powerful probe into the history and contents of the universe. Detection of degree-scale, odd parity B-modes polarization signal imparted from a stochastic gravitational wave background of the primordial universe would strongly confirm the theory of cosmic inflation. This requires a telescope which observes the sky with high sensitivity and optical fidelity over a broad frequency spectrum for foreground contamination removal. Simons Array is a new telescope array in the Atacama Desert of Chile, designed for simultaneous sensitivity to the large-scale primordial B-mode signal and the small-scale B-mode signal from gravitational lensing of the CMB by large-scale structure.

This thesis presents the development of the cryogenic optics of the Simons Array cameras and a new anti-reflection (AR) coating technology for precision CMB polarimetry. An overview of Big Bang cosmology and the CMB is first given as scientific motivation. Then a brief description of the basic principles of telescope optics is given as a background to the following discussion on Simons Array optics and AR coatings. Next, the development and validation of the Simons Array optics tubes, the sub-component of the camera which houses the optical components, are described. Finally, the developments and fabrication processes of AR coating technologies utilized by Simons Array and other experiments for CMB observation are discussed.

To my family

Contents

List of Figures

List of Tables

Acknowledgments

The work presented in this thesis is the product of many years of effort with help from many wonderful people. I must first thank my advisor, Adrian Lee, who welcomed me into his group in 2014 and has supported me since. Being in your research group, I've had the chance to become involved in the Simons Array, Simons Observatory, South Pole Telescope, LiteBIRD, and CMB-S4 collaborations and learn so much along the way. I've also had the privilege of working with Toki Suzuki from whom I've learned most of what I know about CMB instrumentation. You were patient but honest in your guidance when I came into the group with little knowledge of cosmology or what it meant to be a member of a large collaboration. Thank you to Bill Holzapfel who was almost a second advisor for anything regarding optics, especially in the early days of my graduate career.

The other resources throughout my PhD have been my fellow graduate students, post-docs, and engineers of past and present who helped and taught me so much, including Ben Westbrook, Yuji Chinone, Chris Raum, Shawn Beckman, Charles Hill, Neil Goeckner-Wald, John Groh, Ari Cukierman, Kevin Crowley, Darcy Barron, Praween, Aashrita Mangu, Yuyang Zhao, Nick Huang, Jessica Avva, and Sam Guns. Dick Plambeck has also been a great resource in driving and critically analyzing my work on anti-reflection coating development.

I'd like to thank the wonderful people of the UC Berkeley physics machine shop, Warner Carslisle, Abel Gonzalez, Tommy Gonzalez, and Gordon Long. You accommodated so many high precision and high priority jobs over the years, especially as we were building up the Simons Array receivers.

To my friends Daniel Toker, Michael Newman, Minnie Tantiphipop, Colin McNally, Robert Kealhofer, and Serei Panh. From our Friday night hangouts to random texts, you reminded me that life wasn't all about work.

That leaves my family, who loved and supported me through this very long PhD. You made sure I could stay grounded and driven through the highs and lows of graduate school. Dad, you have always been and always will be my role model as a physicist and human being. Mom, your love and care allowed me to focus solely on my work. I could always eat your home cooked meals in my freezer when I felt down or homesick. Kyle, we've supported each other for all of my life. You have always been and always will be my best friend. Sophie, your wisdom in navigating work and family as a graduate student and loving daughter and sister continues to amaze me. I've learned so much from you. Gyeoul, you hold a special place in my heart as my baby brother and I couldn't have gotten through the pandemic without your silly and lovable antics. And finally, my fiancé, Nicole, you are the love of my life and you've made these last four years unforgettable. I continue to be amazed by your drive and brilliance.

Thank you, everyone.

Chapter 1

Introduction

1.1 Standard Model of Cosmology

Modern cosmology is rooted in the axiom of the Cosmological Principle, which asserts that the properties of the observable universe is the same for all observers on sufficiently large scales - our universe is both homogeneous and isotropic. The observational breakthroughs of Edwin Hubble in the 1920s showed galaxies were receding from us with velocities that increased the further away they were, now known as Hubble's Law [39]. Georges Lemaître further deduced from rewinding the cosmological clock that the expanding universe must have originated from a single point, thus establishing the Big Bang model of cosmology [46]. This eventually led to the development of our current Standard Model of cosmology, also called the ΛCDM model, which uses the theoretical frameworks of the Standard Model of particle physics and general relativity to parameterize the Big Bang model with three components of the universe: the cosmological constant, non-relativistic matter, and radiation. This parameterization begins by imposing the Cosmological Principle with the Friedmann-Robertson-Walker (FRW) metric,

$$ds^2 = -c^2 dt^2 + a(t)^2 \left(\frac{dr^2}{1 - kr^2} + r^2 \left(d\theta^2 + \sin^2 \theta d\phi^2 \right) \right) \tag{1.1}$$

where r, θ, ϕ are spherical coordinates, $a(t)$ is the scale factor, and k is the curvature of space. k has possible values 0, +1, and -1 corresponding to flat, closed, and open curvature of space, respectively. Scale factor, whose present value is set to unity, describes the relative expansion of space by relating the constant co-moving distance between points to the increasing physical distance between points.

As galaxies and other matter recedes from our frame of reference in an expanding universe, emitted light is Doppler shifted to longer wavelength, a phenomenon known as redshift. Redshift is defined as,

$$\frac{1}{a_e} = \frac{\lambda_o}{\lambda_e} = 1 + z \tag{1.2}$$

where a_e is scale factor when light was emitted, λ_o and λ_e are wavelengths of light when it was observed and emitted, respectively, and z is redshift. Redshift is often used interchangeably to denote both age of observed photons and the distance to their source. Equation 1.2 shows that as scale factor increases monotonically with time, redshift decreases towards zero at present time.

The Einstein field equations relate the metric of spacetime to the distribution of matter and energy within it. Using the FRW metric to compute the Ricci tensor, $R_{\mu\nu}$, and solve the time-time component of the Einstein field equations of general relativity yields the Friedmann equations[1],

$$\left(\frac{\dot{a}}{a}\right)^2 = \frac{8\pi G}{3}\rho - \frac{k}{a^2}, \tag{1.3}$$

$$\frac{\ddot{a}}{a} = -\frac{4\pi G}{3}\left(\rho + 3p\right) \tag{1.4}$$

where G is the gravitational constant, ρ is energy density, and p is the pressure of a perfect isotropic fluid. Equation 1.3 is typically written with $H(t)$, the Hubble parameter, defined as

$$H(t) = \frac{\dot{a}(t)}{a(t)}. \tag{1.5}$$

In the ΛCDM model, energy density $\rho(t)$ consists of three components that scale differently with time: dark energy (constant in time), radiation ($\propto a^4(t)$), and non-relativistic matter ($\propto a^3(t)$). For the instance of a flat universe, an empirically proven statement to be discussed in more detail, $k = 0$ and Equation 1.3 yields the solution for critical energy density,

$$\rho_{cr}(t) = \frac{3H^2(t)}{8\pi G}. \tag{1.6}$$

Critical energy density is thus defined as the density at present required for the universe to be flat. It is useful to define the dimensionless quantity Ω_i when discussing the density parameterization of the ΛCDM model, given by

$$\Omega_i(t) = \frac{\rho_i(t)}{\rho_{cr}(t)} \tag{1.7}$$

and thus,

$$\Omega(t) = \sum \Omega_i(t) \tag{1.8}$$

where values of $\Omega(t)$ is equal to 1, less than 1, or greater than 1, for a flat, closed, or open curvature, respectively.

Expanding on each density contribution to the Friedmann equation, we describe each component in greater detail and our current knowledge of their densities. Matter consists of non-relativistic particles and its energy density is given by the usual definition with rest

---

[1] We set $c = 1$ in this chapter

mass energy multiplied by number density. As such, its number density and consequently energy density dilutes as the universe expands given by

$$\rho_m(a) = \frac{\rho_{m,0}}{a^3} \tag{1.9}$$

$$\Omega_m(a) = \frac{\Omega_{m,0}}{a^3}. \tag{1.10}$$

Matter consists of two sub-components: cold dark matter (CDM) and baryonic matter. CDM only interacts via gravitational force and makes up 85% of all matter, while baryonic matter consists mainly of protons, neutrons, and electrons[2]. Current measurements show matter density to be $\Omega_m = 0.315 \pm 0.007$ and constrain their individual densities to be $\Omega_{CDM}h^2 = 0.1200 \pm 0.0012$ and $\Omega_b h^2 = 0.02237 \pm 0.00015$ [30]. Radiation is made up of relativistic particles whose energy density contribution comes from their kinetic energy. Its energy density dilutes more strongly with expansion of spacetime than that of matter as not only its number density decreases, its energy does as well as wavelength stretches. Thus, its energy density scales with time as

$$\Omega_r(a) = \frac{\Omega_{r,0}}{a^4}. \tag{1.11}$$

In the early universe, there are two main sub-components of radiation: photons and neutrinos, with neutrinos having already become non-relativistic in present time. Photons have been measured to an extraordinary degree with current measurements showing $\Omega_r h^2 = 2.473 \times 10^{-5} \left(T_0/2.7255\right)^4$ with present-day temperature $T_0 = 2.7255 \pm 0.0006$ K. Neutrino density is constrained at $0.0013 \leq \Omega_\nu < 0.016$ [7], where neutrino mixing and cosmic microwave background (CMB) measurements provide the lower and upper limits, respectively. Dark energy is the least understood component of the cosmological inventory but contributes the majority of the present-day energy density of the universe. Little is known other than that it is homogeneous and an intrinsic energy of the vacuum of spacetime. Also called the cosmological constant, first coined by Einstein in order to achieve a static universe, it is thus constant with time

$$\Omega_\Lambda(a) = \Omega_{\Lambda,0}. \tag{1.12}$$

Current measurements of energy density show $\Omega_\Lambda = 0.6847 \pm 0.0073$ [30]. Using Equations 1.14, 1.5, and 1.7, we can write

$$1 - \Omega(t) = -\frac{k}{a(t)^2 H^2(t)} = \Omega_k. \tag{1.13}$$

This shows that measurement of present-time energy density Ω_0 can constrain the spatial curvature. Current measurements show $\Omega_k = 0.0007 \pm 0.0019$ [30].

Now incorporating the different components with their scaling to Equation 1.3, it becomes

$$H^2 = H_0^2 \left(\frac{\Omega_m}{a^3} + \frac{\Omega_r}{a^4} + \Omega_\Lambda + \frac{\Omega_k}{a^2} \right). \tag{1.14}$$

---

[2] A misnomer since electrons are not baryons, but rather leptons

1.2 Cosmic Microwave Background Radiation

When the temperature of the universe was greater than 13.6 eV, the ionization energy of hydrogen, there were no bound nuclei and the universe was ionized. Photons undergo frequent scattering with electrons and thermal equilibrium is established between photons and baryons with this tight coupling. Baryon density is far lower than photon density, leading to photons dominating the thermodynamics of the photon-baryon fluid and both species are diluted in temperature by expansion as $T = T_0/a$. As the universe continues to expand and cool until $z \sim 1100$ or $t \sim 380,000$ years or $T \sim 1$ eV, neutral hydrogen is formed and the scattering cross-section of media for photons to scatter is significantly reduced. Photons decouple from baryonic matter at the surface of last scattering and the mean free path of photons is greatly increased. Interactions between photons and matter become so infrequent that the universe becomes transparent for photons to free-stream on large scales. These photons are the CMB and redshift until the present temperature of $T_0 = 2.7255$ K. They provide a snapshot of the universe at recombination, and while there is no direct observation before this epoch, primordial information is imprinted in the temperature and polarization anisotropies of these photons.

Blackbody Spectrum

When photons were in equilibrium with baryons, their number density was governed by Planck's law,

$$n_\nu = 8\pi \frac{\nu^2}{e^{h\nu/T} - 1}. \tag{1.15}$$

After recombination, these photons are no longer in thermal contact with baryons and each other, thus retaining the spectral shape of Equation 1.15 with its evolution determined solely by volumetric dilution and redshifting of their wavelength. Photon energy density is given by,

$$\rho_\gamma = 2 \int \frac{d^3p}{(2\pi)^3} \frac{1}{e^{p/T} - 1} p = \frac{\pi^2}{15} T^4, \tag{1.16}$$

and having deduced that ρ_γ scales as a^{-4}, this shows that for photons $T \propto a^{-1}$. Note that this calculation is done within the context of a perfectly smooth universe, which is empirically false given the observed anisotropies of the CMB and can be analytically calculated by introducing perturbations to the Einstein field equations.

First discovered in 1965 by Arno Penzias and Robert Wilson of Bell Laboratories, they used a 20 ft horn antenna to characterize an excess antenna temperature of 3.5±1.0 K at 4 GHz that was isotropic, unpolarized, and constant [65]. Their discovery of the CMB was published alongside a companion paper by R. Dicke, P. Peebles, P. Roll, and D. Wilkinson who correctly postulated the origin to be the blackbody afterglow of the Big Bang, redshifted to the measured temperature [35]. This was a huge leap forward in Big Bang cosmology, but the spectral shape of the CMB was not characterized as Penzias and Wilson were operating

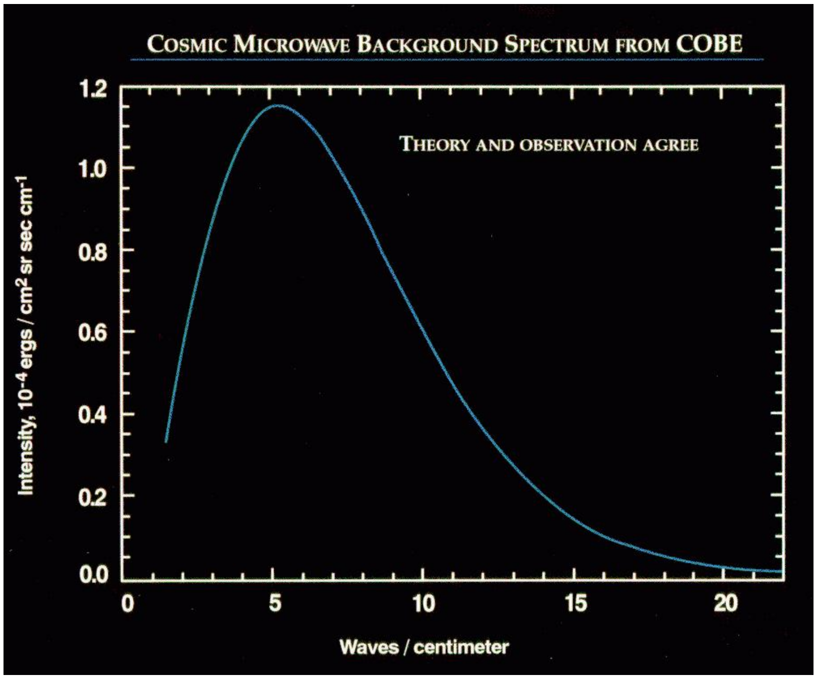

Figure 1.1: The measured intensity spectrum of the CMB, showing a perfect blackbody spectrum [8].

in the Rayleigh-Jean limit by measuring at 4 GHz. Following Wien's displacement law, photons of $T = 2.7255$ K have a peak frequency of $\nu_{peak} = 160$ GHz. Given this fact, the CMB had to be sampled up to its peak frequency to show its blackbody spectral shape and break the degeneracy between temperature and emissivity. 30 years after its discovery, FIRAS of the COBE satellite measured its intensity spectrum, shown in Figure 1.1, and measured its temperature to be $T_0 = 2.728 \pm 0.004$ K [8].

1.3 Cosmic Inflation

The Standard Model of cosmology is not consistent with certain observed characteristics of the universe without resorting to enforcing very specific initial conditions, which is referred to as the fine-tuning problem. These apparent paradoxes can be solved by going beyond the ΛCDM model with the theory of cosmic inflation [37][62][43].

Beyond the Standard Model

The CMB displays a remarkably uniform temperature across the entire sky, to 1 part in 10^5. Puzzling is the fact that points separated by distances larger than what light could have traveled since the beginning of the universe seem to have been in causal contact, given the observed uniformity of the CMB. The comoving horizon, η, is defined as,

$$\eta = \int_0^a \frac{da'}{a'} \frac{1}{a' H(a')} \tag{1.17}$$

which is the maximum comoving distance traveled by photons since the beginning of the universe and largest distance separating points in causal contact. We observe in the CMB that points separated by more than $\sim 2^\circ$, the comoving horizon, are the same temperature. This is called the horizon problem and is not explained solely by the ΛCDM model.

Physical cosmology has empirically shown the universe is currently nearly flat, but the standard model implies the universe was flat to an arbitrarily high number of decimal points in the early universe. After rewriting using Equation 1.5, Equation 1.13 becomes

$$\Omega_k = -\frac{k}{\dot{a}^2} \tag{1.18}$$

and for the curvature parameter at points in time t_i and t_0 denoting initial and present time, respectively,

$$\frac{\Omega_{k,0}}{\Omega_{k,i}} = \left(\frac{\dot{a}_i}{\dot{a}_0}\right)^2. \tag{1.19}$$

The problem lies in that the curvature density parameter has been growing rapidly for most of cosmological history. During the period of time in the universe where radiation density dominated, $\dot{a} \propto t^{-1/2}$ and thus $\Omega_{k,0}/\Omega_{k,i} = t_0/t_i$. During the matter density domination, $\dot{a} \propto t^{-1/3}$ and thus $\Omega_{k,0}/\Omega_{k,i} = (t_0/t_i)^{2/3}$. Finally, during dark energy domination, $\dot{a} \propto \exp(H_0\sqrt{\Omega_\Lambda} t)$ and thus $\Omega_{k,0}/\Omega_{k,i} = \exp(-2H_0\sqrt{\Omega_\Lambda}(t_0 - t_i))$. We see from these curvature ratios that curvature increased during both the radiation and matter dominated eras and decreased during the recent dark energy dominated era. Since $t = 1$ sec, Ω_k has grown by $\sim 10^{16}$ and since Planck time, Ω_k has grown by 10^{60}. This would suggest an aribtrarily fine-tuned initial condition in the early universe to achieve today's flatness. This is called the flatness problem.

An elegant solution to these problems is cosmic inflation, which is the theory of exponential expansion of space in the early universe, lasting from $\sim 10^{-36}$ to $\sim 10^{-32}$ sec. Furthermore, it explains the origins of large scale structure of the universe with quantum fluctuations in the metric that expands to cosmic scales to become the gravitational seed for growth of structure. With regard to the horizon problem, inflation allows points in causal contact to be in extremely close proximity compared to the horizon until exponential expansion increases the distance between them to beyond the distance to the horizon until the radiation dominated era. This means that the entire observable universe is in causal contact in the early universe and thermal equilibrium is established before standard model cosmology begins. With regard to the flatness problem, we saw before that space expands exponentially during the dark energy dominated era and flatness is reduced. Exponential expansion before radiation dominated era can reduce flatness to arbitrary number of decimal places and thus remove the sensitive dependence on the initial value. For a model where the Hubble rate is nearly constant during inflation,

$$\frac{da}{a} = Hdt \tag{1.20}$$

and thus

$$a(t) = a_e e^{H(t-t_e)} \tag{1.21}$$

where a_e is the scale factor at the end of inflation and $t < t_e$. For this scale factor, we see using Equation 1.19 that $\Omega_{k,e}/\Omega_{k,i} = \exp(-2H(t_i - t_0))$. This model can allow for this value to be arbitrarily small by allowing a very large number of e-folds, the natural log of the exponential factor, to occur during inflation.

Scalar Field

So what is the mechanism behind cosmic inflation? Unfortunately, there is yet to be a concrete model and the source of inflation has to be discussed in terms of a general scalar field which we call the inflaton. We want a mechanism which produces accelerated expansion, which means

$$\frac{d^2a/dt^2}{a} = -\frac{4\pi G}{3}\left(\rho + 3P\right) > 0. \tag{1.22}$$

Therefore, $P < -\rho/3$ and the inflaton field is not ordinary matter or radiation and must produce negative pressure, but has some familiarity in that Dark Energy is another hypothetical form of energy which produces negative pressure. More specifically, the prevailing model of inflation is called slow-roll inflation and describes a scalar field rolling down a potential energy hill very slowly compared to the Hubble rate [48][27]. Like Dark Energy, there is a period in which constant energy density with negative pressure causes the accelerated expansion of space. The inflaton eventually undergoes a phase transition of reheating to fill the universe with the hot and dense plasma. This model first begins with a vacuum state, a state of quantum fields at a local minimum potential, which has a very large energy from non-zero vacuum expectation value of the inflaton scalar field. However, it is initially at a false vacuum which changes very slowly as the field falls slowly towards the true minimum, slowly enough for energy density to be approximately constant. At the true vaccuum, the inflaton can decay to give rise to standard model particles.

The equation of motion for this field is given by

$$\ddot{\phi} + 3H\dot{\phi} + V'(\phi) = 0 \tag{1.23}$$

where ϕ is the scalar field and $V(\phi)$ is the potential for the field. Given that potential energy is much larger than the kinetic energy, the Friedmann equation is given by

$$H^2 \simeq \frac{V(\phi)}{3M_P^2} \tag{1.24}$$

where M_P is the Planck mass.

The energy scale of inflation, which is $\sim 10^{16}$ GeV, is nearly the Planck scale, and thus the quantum fluctuations of the inflaton field will couple to the metric of spacetime. These perturbations to the metric stretch to large scales through inflation and become the source of CMB anisotropies and the seeds of large scale structure. Some of the observables of inflation will be discussed in a later part of this chapter.

1.4 CMB Anisotropies

Up to this point, descriptions of the CMB have only been on zero-order distribution of photon energy density, assuming a perfectly smooth universe. In reality, CMB anisotropies of less than 100s of μK have been measured and have been an integral tool for modern CMB research as a scope into the early universe. As briefly discussed in Section 1.3, inhomogeneities in the inflaton field are hypothesized to couple to the metric and particles of the early universe, which evolve into these anisotropies of the CMB.

There are two kinds of perturbations to the metric of interest: scalar and tensor. We first discuss scalar perturbations, given by

$$\begin{aligned} g_{00}(\vec{x},t) &= -1 - 2\Psi(\vec{x},t) \\ g_{0i}(\vec{x},t) &= 0 \\ g_{ii}(\vec{x},t) &= a^2(t)\delta_{ij}(1+2\Phi(\vec{x},t)) \end{aligned} \tag{1.25}$$

where Ψ and Φ are perturbations to the Newtonian potential and spatial curvature, respectively. These perturbations are then incorporated into Einstein's field equations to relate the metric to density perturbations. Because these perturbations are small, these equations remain linear, which is of great convenience as it allows the Fourier modes of photon density perturbations to evolve independently through time. This results in the following equation for perturbed Einstein equations of the photon-baryon fluid,

$$\begin{aligned} k^2\Phi + 3\frac{\dot{a}}{a}\left(\dot{\Phi} - \Psi\frac{\dot{a}}{a}\right) &= 4\pi G a^2\left(\rho_m\delta_m + 4\rho_r\Theta_0\right) \\ k^2\left(\Phi + \Psi\right) &= -32\pi G a^2 \rho_r \Theta_2 \end{aligned} \tag{1.26}$$

where Θ_n is the n-th moment of the radiation field perturbation, $\delta T/T$, and δ_m is the ratio of matter overdensity. Lower order moments of perturbation dominate as higher order moments are washed out from strong coupling of Compton scattering. Equations 1.26 determine how these perturbations evolve until recombination to leave behind anisotropies in the CMB. These Fourier modes are acoustic oscillations of the photon-baryon fluid as scalar perturbations in the metric lead to over- and under-dense regions in the plasma. Over time, matter falls into over-dense regions and form gravitational wells that attract baryons. Photons, in equilibrium with matter will oppose baryons with pressure. This push and pull will create sound waves on the photon-baryon fluid which get "frozen-in" on the photon distribution by

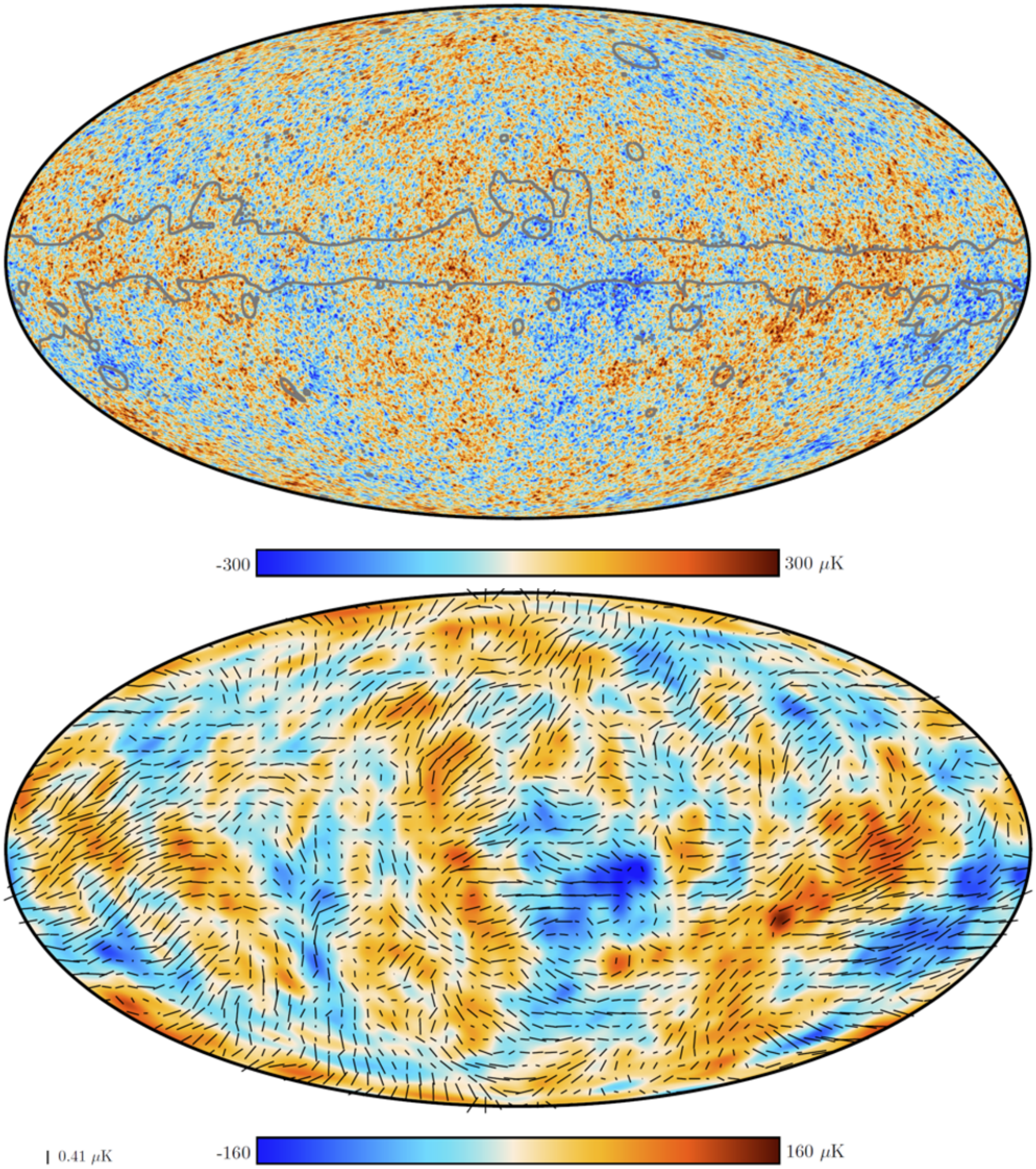

Figure 1.2: Full-sky maps of the CMB temperature (*top*) and polarization (*bottom*) anisotropies from Planck's 2018 data release [29].

recombination. Some modes of oscillation enter the horizon before decoupling, called sub-horizon modes, and some modes enter after decoupling, called super-horizon modes. As these modes enter the horizon and thus begin being affected by causal physics, they oscillate and change over time. Thus amplitude of perturbation modes differ based on the time of entry, where generally the earlier a mode enters, the more they will have decayed. Super-horizon modes remain unchanged and their primordial characteristics remain for CMB cosmologists to study the early universe. The sum of power of these modes at a range of angular scales at decoupling determines the anisotropy signal.

In addition to scalar perturbations, inflation also produces tensor perturbations to the spacetime metric which we call gravitational waves. They can be represented mathematically by

$$\begin{aligned} g_{00} &= -1 \\ g_{0i} &= 0 \\ g_{ij} &= a^2 \begin{pmatrix} 1+h_+ & h_\times & 0 \\ h_\times & 1-h_+ & 0 \\ 0 & 0 & 1 \end{pmatrix} \end{aligned} \tag{1.27}$$

where the perturbation terms h_+ and $h_\times$ are chosen to be in the xy-plane. The result of the tensor-perturbed Einstein equation is

$$\ddot{h}_\alpha + 2\frac{\dot{a}}{a}\dot{h}_\alpha + k^2 h_\alpha = 0 \tag{1.28}$$

where $\alpha \in \{+, \times\}$. Equation 1.28 is a wave equation for gravitational waves. This solution shows that small-scale modes decay rapidly when their wavelengths become comparable to the horizon, and therefore anisotropies on small angular scales are not affected by gravitational waves. Large scale anisotropies are, however, affected by gravitational waves.

Deriving the Einstein equations with tensor perturbations leads to the revelation that there are no tensor contributions to the time-time component of the Ricci tensor and the Ricci scalar. This fact is important as it leaves density perturbations solely coupled to scalar perturbations to the metric, which do indeed contribute to the time-time component of the Ricci tensor and the Ricci scalar. Tensor perturbations do not affect the formation of large scale structure. This is named the decomposition theorem, which states that perturbations to the metric evolve independently. A fundamental prediction of inflation is the production of a stochastic background of gravitational waves. Specifically for slow-roll inflation, gravitational waves are generated by vacuum fluctuations of the scalar field and metric during inflation. Along with the decomposition theorem, this makes the measurement of primordial gravitational waves a powerful channel into the confirmation and study of cosmic inflation.

Power Spectrum

The CMB is a Gaussian field and thus the statistical properties of its fluctuations are fully contained within its power spectrum, which is directly related to the 2-point correlation function of fluctuations. Conventionally, CMB anisotropies are written in terms of spherical harmonics as,

$$\Theta = \sum_{\ell=0}^{\infty} \sum_{m=-\ell}^{+\ell} a_{\ell m} Y_{\ell}^{m} \left(\hat{n}\right) \tag{1.29}$$

where $\hat{n}$ is also typically written as (θ, ϕ), and ℓ is a representation of angular scale on the sky as $\theta \propto 180^{\circ}/\ell$. Since we are working with Gaussian random fields, $a_{\ell m}$ is drawn from a Gaussian distribution with mean of zero and some finite variance. The CMB's statistical isotropy means that the 2-point correlation function only depends on the angular distance and not the exact coordinates, and,

$$\left\langle \Theta\left(\hat{n}\right) \Theta\left(\hat{n}'\right) \right\rangle = \frac{1}{4\pi} \sum_{\ell=0}^{\infty} \left(2\ell+1\right) C_{\ell}^{TT} P_{\ell}\left(\hat{n} \cdot \hat{n}'\right) \tag{1.30}$$

where P_{ℓ} are Legendre polynomials and C_{ℓ}^{TT} is defined by

$$\left\langle a_{\ell m} a_{\ell m}^{*} \right\rangle = \delta_{\ell \ell'} \delta_{m m'} C_{\ell}^{TT}. \tag{1.31}$$

One may notice from Equation 1.30 that calculations of C_{ℓ} are limited by the finite number of ℓ modes to sample from, that number being $(2\ell + 1)$. The number of samples is further reduced when only a fraction of the sky, f_{sky}, is observed. This leads to a sample variance limit called the cosmic variance, given by

$$\Delta C_{\ell} = \sqrt{\frac{2}{\left(2\ell+1\right) f_{sky}}} C_{\ell}, \tag{1.32}$$

where we have dropped the TT superscript as these equations apply generally to the power spectra of different kinds of anisotropies, as will be discussed in the following sections.

1.5 Polarization

CMB anisotropy signal also contains polarized light from Thompson scattering which is more than an order of magnitude smaller than the unpolarized, temperature anisotropy signal. Thompson scattering can generate linear polarization if incident photons have nonzero quadrupole moment, which as shown with Equation 1.26, is very small due to higher order moments being suppressed in the tight coupling limit. A diagram illustrating the production of linear polarization from scattering of two photons of differing energy from perpendicular incidence angles is shown in Figure 1.3. This leads to a polarization power that is subdominant to temperature power in CMB anisotropy signal. Measurements of polarization anisotropy are characterized by Stokes parameters, defined as

$$\begin{aligned} I &= \left|E_x\right|^2 + \left|E_y\right|^2 \\ Q &= \left|E_x\right|^2 - \left|E_y\right|^2 \\ U &= 2\mathrm{Re}\left\langle E_x E_y^{*} \right\rangle \\ V &= -2\mathrm{Im}\left\langle E_x E_y^{*} \right\rangle, \end{aligned} \tag{1.33}$$

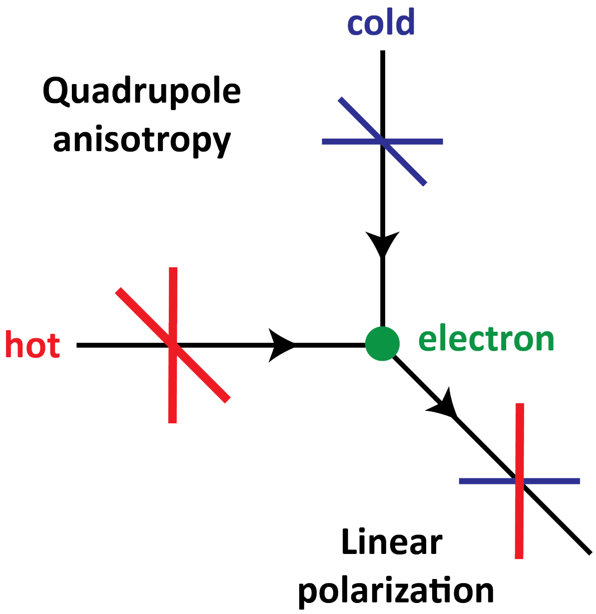

Figure 1.3: A schematic diagram showing quadrupole moment of incident photons due to temperature anisotropies generating linear CMB polarization.

where for a wave propagating along the z-direction, E_x and E_y are amplitudes of the electric field in the x- and y-directions, respectively. I is the total intensity, Q is the polarization component along 0° and 90°, U is the polarization component along ±45°, and V is the circular polarization component. V can be produced post-recombination via Faraday rotation but is yet to be measured as nonzero [50]. A diagram showing Q and U patterns are shown in Figure 1.4. Any linear polarization signal can be fully described by a linear combination

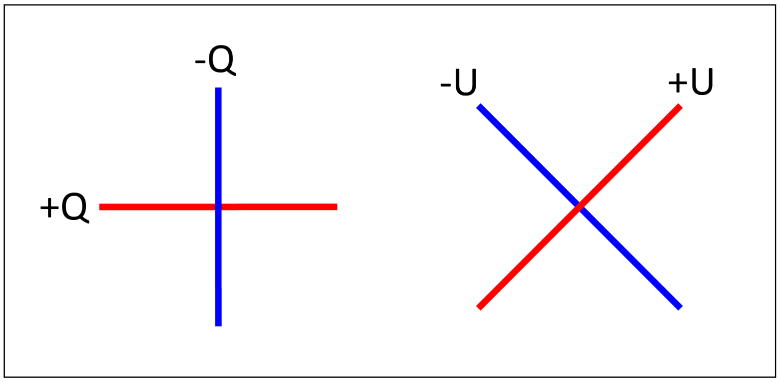

Figure 1.4: Graphic illustration of linear polarization components, Q and U, of the Stokes parameters.

of measured Q and U at any point in the sky. Some more useful quantities in discussing measured polarization are,

$$\begin{aligned} I_p &= \sqrt{Q^2 + U^2} \\ \theta &= \frac{1}{2}\tan^{-1}\left(U/Q\right), \end{aligned} \tag{1.34}$$

where I_p is the total intensity of linearly polarized signal and θ is the angle of polarization.

Due to their coordinate dependent definition, we re-parametrize the Stokes parameters into coordinate invariant quantities, E- and B-modes [59][58]. E-modes are the even parity, curl-free component of the field and B-modes are the odd parity, divergence-free component of the field. As Figure 1.5 shows, they can be distinguished by their behavior under parity transformation, $\vec{r} \rightarrow -\vec{r}$. Since B-modes contain handedness, they change signs under this transformation. E- and B-modes are non-local quantities and do not represent polarization at any single point in the sky, and instead represent the global polarization properties.

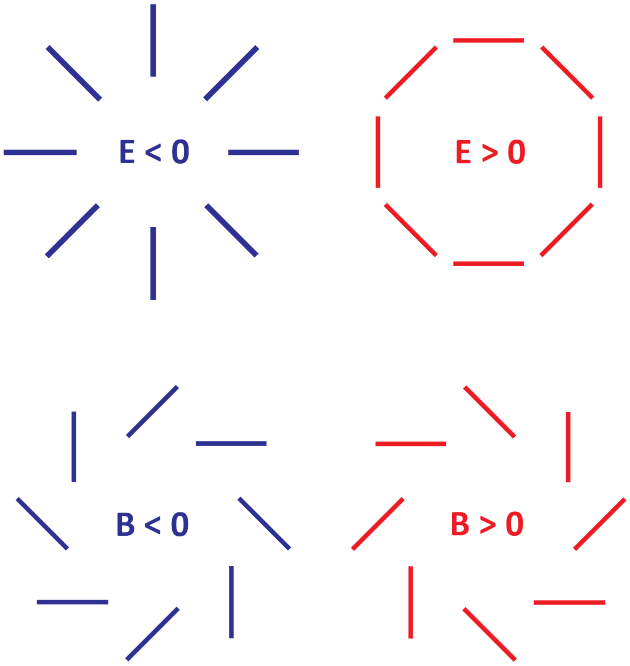

Figure 1.5: Graphic illustration of the even parity E-mode and odd parity B-mode.

Polarization is decomposed into spin-2 spherical harmonics, given by

$$Q \pm iU = \sum_{\ell=0}^{\infty} \sum_{m=-\ell}^{+\ell} \left(a_{\ell m}^{E} \mp a_{\ell m}^{B}\right)_{\mp 2} Y_{\ell m}, \tag{1.35}$$

where $a_{\ell m}^{X}$ coefficients are written separately for E- and B-modes denoted by $X \in \{E, B\}$. Given that the same statistics apply to polarization as temperature anisotropy, we can write the power spectra

$$\left\langle a_{\ell m}^{X} a_{\ell m}^{Y*} \right\rangle = \delta_{\ell\ell'}\delta_{mm'}C_\ell^{XY}, \tag{1.36}$$

where $X, Y \in \{T, E, B\}$. C_ℓ^{TT}, C_ℓ^{EE}, C_ℓ^{BB} are auto-correlation power spectra for T, E, and B respectively, but they can correlate with each other as well. Cross-correlation functions C_ℓ^{TB} and C_ℓ^{EB} are expected to be zero according to the standard model. C_ℓ^{TE} is expected to be nonzero as T and E signals are both sourced from the same physical mechanisms and have even parity. C_ℓ^{BB} is subdominant to C_ℓ^{EE} as shown in Figure 1.6 at all angular scales but is of great scientific interest at all angular scales with contributions from two components: primordial gravitational waves and weak lensing from large scale structure. We now explore the physics of angular power spectra.

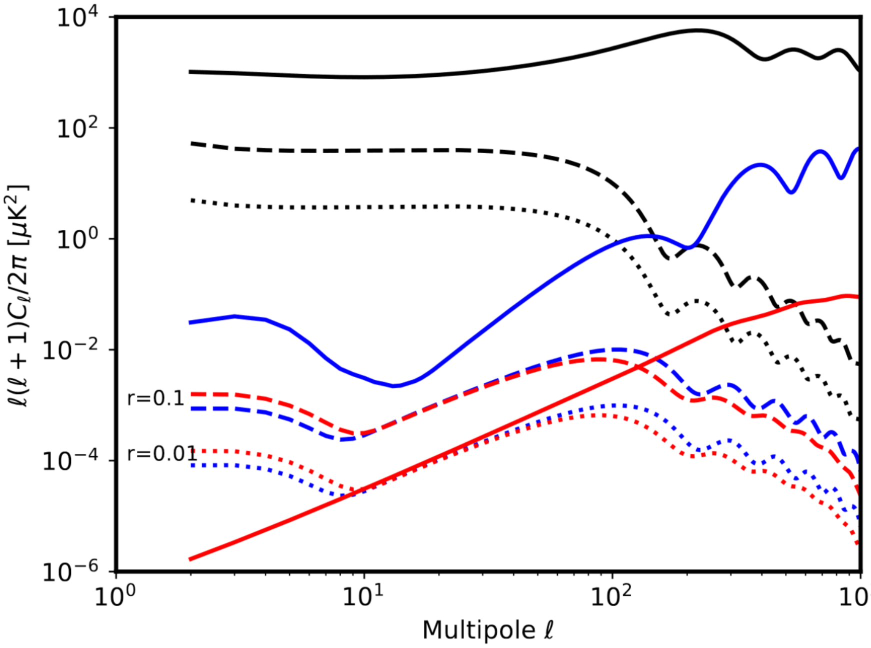

Figure 1.6: Theoretical angular power spectra of temperature (*solid black*), E-mode (*solid blue*), lensing B-mode (*solid red*), and primordial B-mode (*blue* and *red*, *dotted* and *dashed*) signals. Primordial B-mode signal is plotted for two different values of r, to be phenomenologically constrained [18].

1.6 Physics of Angular Power Spectra

Temperature

At $\ell \lesssim 100$, the temperature power spectrum is nearly flat as seen in Figure 1.6. This is due to the Sachs-Wolfe effect where CMB photons redshift as they climb out of potential wells from the surface of last scattering before traveling to us. With a stochastic distribution of potential wells, this creates temperature anisotropy. At these low ℓ's, large scale modes of anisotropy remain outside of causal physics and consequently, acoustic effects, until the era of radiation domination, allowing them to remain unchanged from their early universe states. When we observe anisotropies on these scales, we observe perturbations in their most pristine form when they were set at early times during inflation. The very subtle tilt at $\ell \lesssim 10$ is due to the integrated Sachs-Wolfe effect, which is the gravitational redshift caused by time-varying gravitational potential. When these potentials vary with time-scales similar to the free-streaming photons that move in and out of them, the photons are redshifted.

In contrast to these super-horizon modes, sub-horizon modes have acoustic signatures at $100 \lesssim \ell \lesssim 1000$. On sub-degree scales, the photons are causally affected by gravity-driven acoustic oscillations and the phases of these sound waves are frozen-in, producing the aniostropy at the surface of last scattering. The characteristics of these acoustic peaks directly reflect on the Fourier modes of perturbation that have undergone half-integer number of periods of oscillation by recombination which leaves photons in states of maximal compression and rarefaction inside potential wells. For example, in the first half period, the fluid is pulled and maximally compressed in the potential wells to create an overdensity of photons. Any integer number period added to this first half period creates overdensity of photons by the same physics and correspond to the odd-numbered peaks of the temperature power spectrum. For the even-numbered peaks, the fluid has undergone maximal rarefaction in the potential wells from pressure, which creates maximal compression and thus overdensity on the potential hills. The relative height and angular location of each peak is determined by the baryonic and cold dark matter content of the universe. The angular location of each peak is also determined by the curvature of the universe as it affects the observed length scale.

The power spectrum decays in amplitude at $\ell \gtrsim 2000$ due to Silk damping where photons diffuse on angular scales comparable to their mean free path, washing out acoustic structure. The finite thickness of the surface of last scattering also washes out acoustic structure on comparably small scales.

Polarization

Polarization power spectra also has acoustic peaks but is exactly out of phase with those of the temperature power spectrum. Quadrupole moment in perturbation to the primordial plasma generated by diverging and converging fluid velocities which cause the photons to redshift and blueshift, respectively, along the wavevector. Maximum velocity corresponds to odd number of quarter periods in acoustic standing waves, causing acoustic peaks in polarization, most visible in the E-mode power spectrum, to be out of phase with acoustic peaks in temperature. This relationship is apparently from the non-zero C_ℓ^{TE}. The B-modes are discussed as two separate components, shown in Figure 1.6.

Gravitational wave B-modes, the component discussed in Section 1.4, have yet to be detected and peak at large angular scales near $\ell \approx 100$. Scalar perturbation generates symmetric $m = 0$ quadrupole moment which generates polarization parallel or perpendicular to the direction of density perturbation wavevector. This rotationally symmetric perturbation produces E-modes and not B-modes. Tensor perturbation generates $m = 2$ quadrupole with spin-2 azimuthal symmetry. Equation 1.27 contains h_+, which describes spacetime stretching parallel and perpendicular the perturbation wavevector, and $h_\times$, which describes the spacetime stretching ±45° relative to the wavevector. Because the quadrupole moment of tensor perturbations lacks the rotational symmetry, which is a signature of E-modes, it can also produce B-modes. The fact that B-modes can only be created by tensor perturbations from gravitational waves, which are a unique signature of inflation, makes the detection of large angular scale, primordial B-modes a powerful evidence of inflation. Their amplitude is proportional to the energy scale of inflation as

$$V^{1/4} = 1.06 \times 10^{16} \times \left(\frac{r}{0.01}\right)^{1/4} \text{GeV} \tag{1.37}$$

where V is the aforementioned inflaton potential and r is the tensor-to-scalar ratio. It is defined as

$$r = \frac{P_t}{P_s} \tag{1.38}$$

where P_t and P_s are tensor and scalar perturbation power spectra amplitudes, respectively. Figure 1.6 illustrates the sensitivity of the B-mode power spectrum to the value of r. r is an observable of great scientific impact as a measurement of nonzero r not only provides proof of inflation, its measurement gives the energy scale of inflation. Equation 1.37 shows that inflation occurs at the energy scale of grand unified theory (GUT), with weak dependence on the value of r. A precise value of V can be extracted from a relatively imprecise measurement of r. This detection would open a window into the physics of energy scales at 12 orders of magnitude above what is created by the Large Hadron Collider.

Lensing B-modes are sourced from the weak gravitational lensing of CMB photons by large scale structure, which can be mathematically described as a remapping of the unlensed CMB field from source to image plane as following,

$$\begin{aligned} T(\hat{n}) &= T(\hat{n} + \nabla\phi(\hat{n})) \\ (Q \pm iU)(\hat{n}) &= (Q \pm iU)(\hat{n} + \nabla\phi(\hat{n})), \end{aligned} \tag{1.39}$$

where the deflection angle is written as the gradient of the lens potential, ϕ. Large scale structure in the line of sight between us and the surface of last scattering deflects photon trajectory due to gravity. This effect smears the sharp features in power spectra and converts E-mode signal into B-mode signal as the E-mode rotational symmetry is broken. This deflection of primordial CMB photons can be measured via CMB in combination with other tracers of large scale structure to construct the lensing power spectrum, $C_{\ell m}^{\phi\phi}$, which is a tracer of the matter power spectrum. Unlike primordial B-modes, lensing B-mode signal peaks at small angular scale of $\ell \sim 1000$ as lensing occurs after recombination at low z. This signal is a channel into studying neutrino physics as it is correlated with the matter distribution of the universe from decoupling until present. For relativistic massive neutrinos of the early universe where $T_\nu/a > m_\nu$, their energy is dominated by their momenta and they behave like radiation. Thus they free streams out of gravitational wells and do not participate in the gravitational collapse of CDM and baryons, instead contributing to the attenuation of scalar perturbations by driving the expansion of space as radiation[3]. Thus for a fixed Ω_m, massive neutrinos effectively suppress the amplitude and growth of matter perturbations, relative to neutrinos which are massless. The heavier the sum of neutrinos, the more suppression occurs. The neutrino density is related to the sum of neutrino masses by,

$$\Omega_\nu h^2 = \frac{1}{93\ \text{eV}} \sum_i m_{\nu_i}. \tag{1.40}$$

More specifically, the lens potential estimator $\hat{\phi}_\ell$ and lensing power spectrum can be extracted via lens reconstruction technique which statistically inverts Equation 1.39 from the measured, lensed CMB signal. This is possible as the lensed B-mode signal is highly correlated with the E-mode signal, measured via C_ℓ^{EB}, with a correlation whose shape depends on the lens potential. Figure 1.7 shows the sensitivity of the lensing power spectrum to sum of neutrino masses.

In addition to measurements from neutrino mixing, which provides a lower bound on the sum of neutrino masses, CMB lensing provides constraints on the upper bound and on the neutrino mass hierarchy, for which there are two possible models: inverted and normal. Furthermore, lensing B-mode signal obscures primordial B-mode signal, especially for lower values of r, and thus several methods of delensing have been developed.

1.7 Foregrounds

Given the CMB is the furthest possible light to reach us, there are numerous other sources of light along the line of sight that we must distinguish from CMB signal.

Atmosphere

Ground-based CMB polarimetry experiments are obscured by photons from the atmosphere. Figure 1.8 shows the atmospheric transmission for microwave frequencies in the Atacama Desert of Chile, observed at an elevation of 60° for different levels of precipitous water vapor (PWV) levels.

The narrow lines where transmission drops completely are the characteristic emission lines of hydrogen and oxygen molecules of the atmosphere. Some emission lines of interest to CMB experiments are the oxygen emission line at 60 and 120 GHz and water emission line

---

[3] An effect called "Hubble friction."

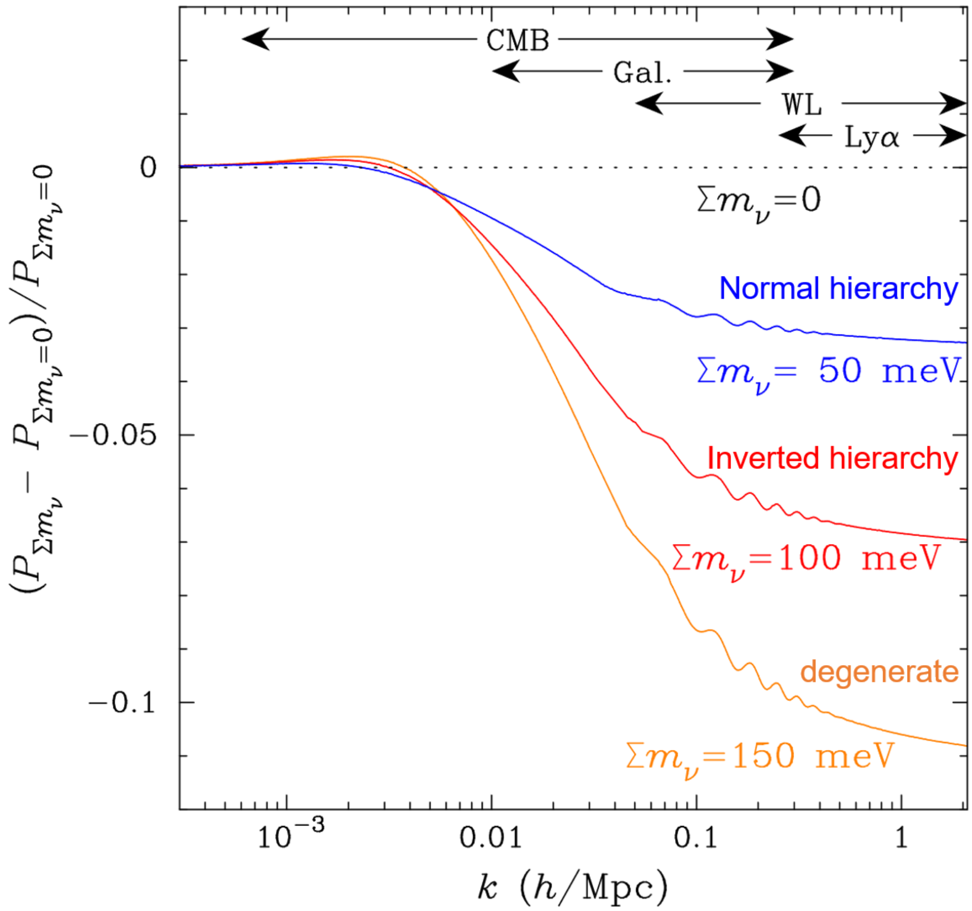

Figure 1.7: Sensitivity of lensing power spectrum to the sum of neutrino mass. Upper bounds on the sum of neutrino mass from CMB measurements also constrains the possible neutrino mass hierarchy models [15].

at 180 GHz. We design the instruments to be sensitive in between these atmospheric windows where observation of cosmic photons is possible from the ground. Thermal emission from the atmosphere is also problematic as it contributes extra thermal loading to the detectors and reduces their sensitivity due to photon noise. Sky brightness temperature is given by

$$T_{\mathrm{ATM}} = \varepsilon_{\mathrm{ATM}} T \tag{1.41}$$

where $\varepsilon_{\mathrm{ATM}}$ is the emissivity of the atmosphere and T is its physical temperature. This relation is valid for mm-wave astronomy operating in the Rayleigh-Jean limit, $h\nu \ll k_B T$, and the sky's optical power is given by

$$P_{\mathrm{sky}} = k_B T_{\mathrm{ATM}} \Delta\nu, \tag{1.42}$$

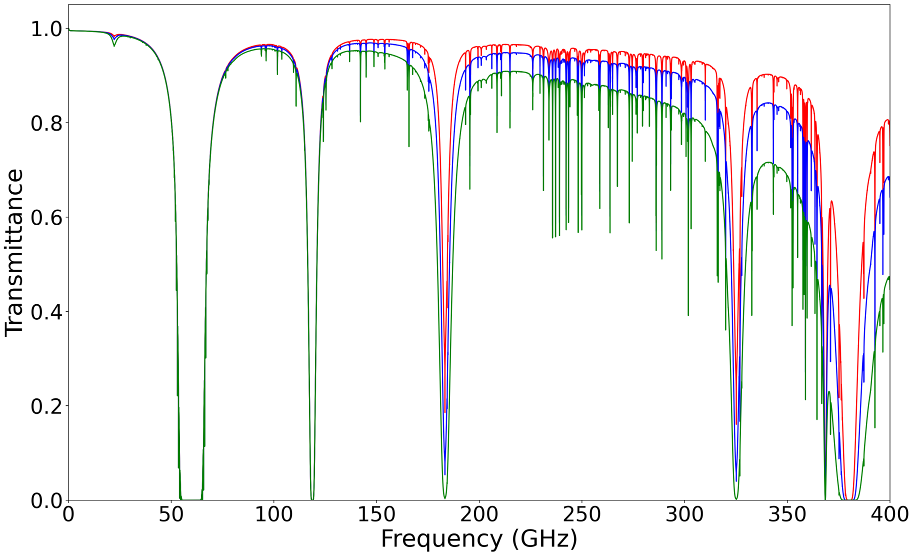

Figure 1.8: Theoretical atmospheric transmittance in the Atacama Desert of Chile for observation at elevation of 60° and PWV values of 0.5 (*red*), 1.0 (*blue*), and 2.0 (*green*) mm. These models are generated using AM [53].

where $\Delta\nu$ is the detector bandwidth. This power contributes on parasitic thermal loading on the detectors and limits sensitivity. Atmospheric absorption increases with frequency [64] as seen in Figure 1.8 and as we will discuss in Section 2.3, thermal emissivity increases as well, limiting sensitivity. Observing in atmospheric windows and PWV levels where transmission is maximized is equivalent to minimizing emissivity and thus thermal loading. The solution is to observe at sites with inherently lower PWV levels, most notably in the Atacama Desert or the South Pole.

Galactic Foregrounds

Figure 1.9 shows the major sources of polarized contamination from space. Polarized emission from interstellar dust dominates at frequencies above 90 GHz. It is hypothesized that dust emission is due to dust grains in interstellar medium which re-emit polarized photons after absorbing light from other astrophysical sources [36]. Net polarization can be emitted if these dust grains become aligned due to galactic magnetic fields. While this dust is strongly concentrated at the galactic plane, it is bright enough to fill the rest of the sky. A simple power law scaling of $T \propto \nu^{\alpha_{dust}}$ is assumed to estimate dust contamination along with measurements of polarized foreground maps from experiments such as Planck at 353 GHz [28]. As dust contamination signal near its minimum of ~100 GHz is larger than pri-

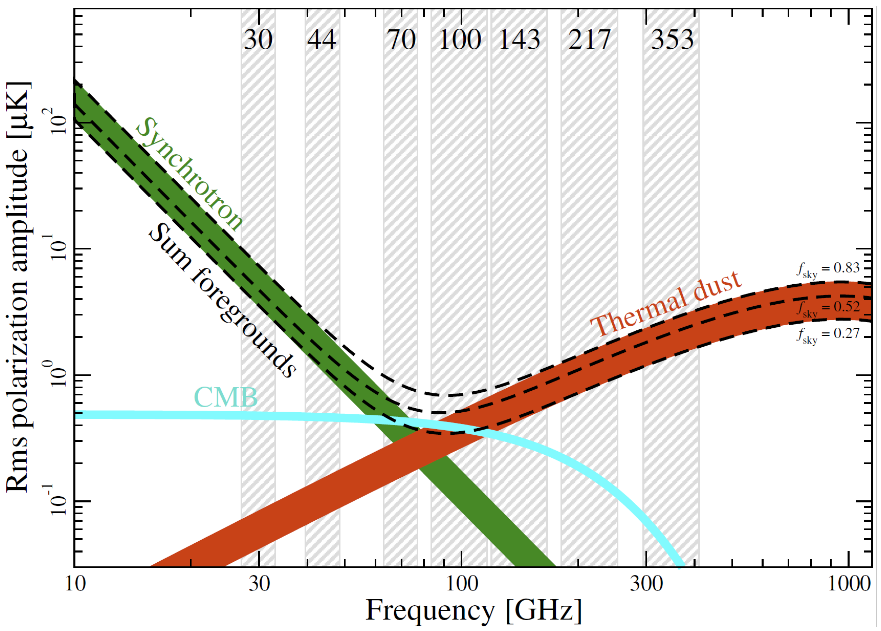

Figure 1.9: Spatially averaged brightness temperature spectra of galactic foregrounds compared to the CMB spectrum [29].

mordial B-mode signal for r $\leq$ 0.1 [31], its removal is critical. Polarized contamination from synchrotron radiation dominates at low frequencies. Synchrotron radiation is the emission from accelerated electrons, in this case, relativistic cosmic ray electrons in galactic magnetic fields. Synchrotron radiation is also governed by a simple power law of $T \propto \nu^{-\alpha_{synch}}$ where the spectra index is hypothesized to be $\alpha_{synch} \sim 2.7 - 3.0$ [34], with polarization power depending on the magnetic field shape. While measurements of sychrotron radiation are limited, it has not been shown to be the dominant galactic foreground contaminant in the CMB observation windows. To characterize and subtract these galactic foreground signals from CMB polarization signal, they must be observed with broad frequency coverage. It will be important for precision CMB measurements to have existing measurements of polarization properties of these foregrounds.

Chapter 2

Principles of Telescope Optics

The core design philosophy of an optical system in modern CMB polarimetry is to image the sky with high fidelity and high optical throughput. As CMB experiments utilize scanning beam-type system, the optics must form a well-defined beam without sidelobes across the large focal plane to prevent systematics, which can contaminate the B-mode channel with signal from the temperature and E-mode channels of much greater power. Additionally, unlike many fields of astronomy where instrumentalists can utilize commercial vendors, CMB instrumentalists are limited by the lack of availability in mm-wave compatible components. Therefore, we build our hardware in-house, from the design level, all the way to fabrication and validation. We expand on some of the basic principles that play a major role in the design process of CMB telescope optics.

2.1 Geometric Ray Optics

Geometric optics is a model of light propagation as rays and is a useful abstraction for approximating the propagation path of light. In this paradigm, the ideal system takes collimated plane waves as input and produces a perfectly focused beam at the detector as output. The degree to which this focus deviates from a single point is called aberrations and leads to the image being blurry or distorted. In CMB optics, the optical chain, down to the detector, is designed in such a way that collimated rays from different angular locations on the sky focus to different detectors. The plane at which the rays come to a focus and thus where the detectors are placed is called the focal plane. Each detector on the focal plane observes a unique location on the sky. The total angular area which a telescope can simultaneously observe is called its field of view (FOV). As Maxwell's equations obey time-reversal symmetry, we can equally describe the propagation of light through an optical chain in both forward-time and reverse-time paradigms. When time moves forward, light rays propagate from the sky and are focused onto the detectors. When time is reversed, light rays propagate out from the detectors and open up towards the sky. It is often convenient to think in this paradigm when designing the optics of a CMB experiment.

F-number, F, is a parameter often used to describe the speed or focusing strength of an optical system, defined as

$$F = \frac{f}{D} \tag{2.1}$$

where f is the focal length and D is the size of the primary aperture. It can also be defined as,

$$F = \frac{1}{2\tan\theta_r} \approx \frac{1}{2\theta_r} \tag{2.2}$$

where the approximation is valid for the paraxial limit. θ_r is the opening half angle, which is defined by a cryogenic aperture stop for the Simons Array receiver[1] which is most easily visualized in reverse-time for what is seen by the detectors. Low F-number optics are referred to as fast optics as light rays converge quickly and vice-versa. Because F-number describes the speed of focusing, it can be measured at any point the in the optical chain. Low F-number is achieved using optics with a combination of high curvature and high index of refraction, both of which lead to technical challenges in achieving high fidelity and high throughput optics. High curvature leads to higher levels of aberrations such as astigmatism and coma from more obtuse incidence angles. High index of refraction requires more technically challenging anti-reflection (AR) coatings to prevent high levels of reflection at a vacuum-optic dielectric boundary. This is expanded upon in Chapter 5.

2.2 Diffraction-Limited Optics

Geometric ray optics do not fully encapsulate the behavior of light that is rooted in its physical nature. Even with a perfectly unaberrated system, it will not be able to observe a single point in the sky due to diffraction, a phenomena which is classically described as the bending of light rays around corners and edges. It leads to an inherent limitation in the resolving power of optics as each detector will observe a finite angular region in the sky, rather than a point. The detector will see an Airy pattern in absence of aberrations and the smallest possible angular size is given by the central peak,

$$\theta \sim 1.22\frac{\lambda}{D} \tag{2.3}$$

where D is the size of the primary aperture. The sky resolution is often referred to as the beam of the telescope. Diffraction can be best explained in full detail as a quantum mechanical phenomenon with Heisenberg's uncertainty principle, given by Equation 2.4. As seen in Figure 2.1, given a single slit in the path of a photon, it localizes the x-position of the photon.

$$\sigma_x \sigma_p \geq \frac{\hbar}{2} \tag{2.4}$$

---

[1] as well as many other receives in CMB polarimetry

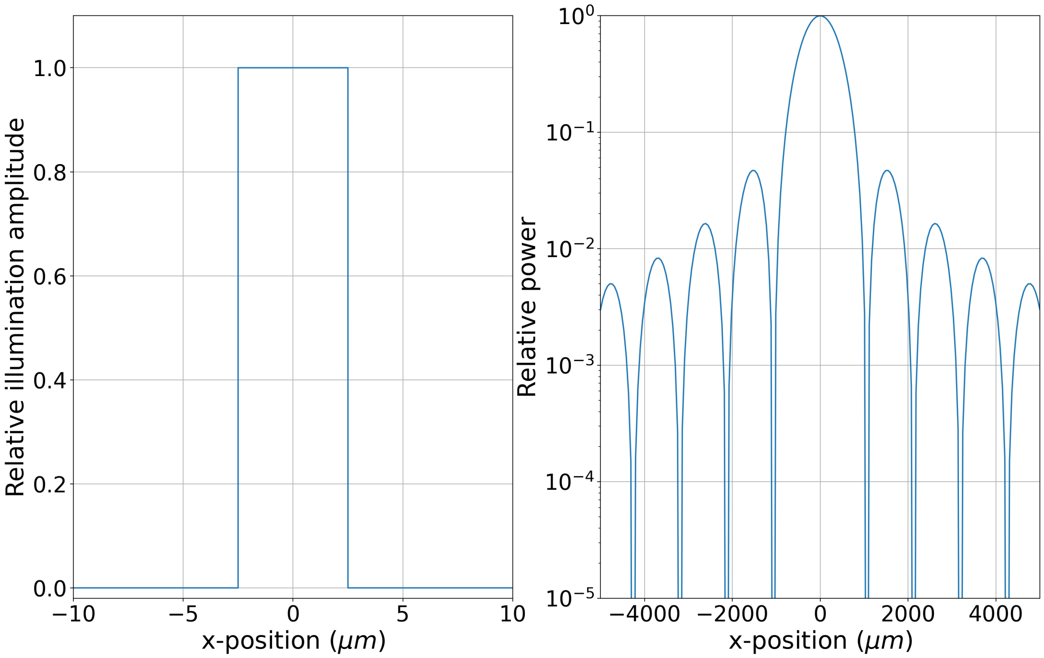

Figure 2.1: Diffraction through a single-slit. Diffraction takes a coherent beam which uniformly illuminates the slit and produces an image containing a main beam of finite size and multiple sidelobes of lower relative power.

Position and momentum are conjugate observables, which means a precise localization of x-position is accompanied by a delocalization of x-momentum. Take a single slit of width, w, which is illuminated with a coherent beam of light. The coordinate-space wave function at the slit is given by,

$$\Psi(x, w) = \begin{cases} \frac{1}{\sqrt{w}} & \text{if} - \frac{w}{2} \leq x \leq \frac{w}{2} \\ 0 & \text{otherwise} \end{cases} \tag{2.5}$$

where w is the width of the slit. A Fourier transform of $\Psi(x, w)$ gives the momentum-space wave function,

$$\Phi\left(p_x, w\right) = \int_{-w/2}^{w/2} \frac{1}{\sqrt{2ip\hbar w}} \exp\left(-\frac{ip_x x}{\hbar}\right) dx = \sqrt{\frac{2\hbar}{\pi w}} \frac{\sin\left(\frac{p_x w}{2\hbar}\right)}{p_x} \tag{2.6}$$

where p_x is the x-momentum. According to quantum mechanics, the diffraction pattern on the conjugate focal plane is $|\Phi\left(p_x, w\right)|^2$, which is the expected sinc function with diffraction fringes or sidelobes arising from the spread in x-momentum. This is an example of a departure from geometric optics, utilizing physical optics, which introduces the use of Fourier transforms to better model the behavior of light between object and image planes.

The is analogous to the Airy pattern which is the conjugate space diffraction pattern of the circular aperture of a telescope. We approximate the central peak of the Airy pattern as a Gaussian, called the main beam, and any deviating characteristics are referred to as sidelobes. Note that Equation 2.3 is accurate for uniform illumination while a real aperture is illuminated by a Gaussian beam profile. As image plane distances of the optics are far greater than pixel size and λ, we work in the far-field regime where Fraunhofer diffraction equation can be used to great accuracy in determining the conjugate image planes in both directions of time. We take a Gaussian illuminated aperture and calculate its conjugate image at the focal plane in the Fraunhofer diffraction regime, given by

$$E\left(x, y, z\right) \propto \int_A A(x', y') e^{-i\frac{2\pi}{\lambda}(lx' + my')} dx' dy' \tag{2.7}$$

where A is the aperture, $A(x', y')$ is the complex aperture function containing information about spatial intensity and phase of the incoming field, and l and m are directional cosines. As one may infer, this is a Fourier transform of the aperture function. This an an instance illustrating why far-field diffraction patterns are easier to model and work with than aberrations since there will be symmetry in the image from the inherent properties of the Fourier transform.

Figure 2.2 shows that beam size scales with non-uniform illumination and that a Gaussian beam which is truncated by an aperture has a larger beam but less power in the diffraction rings. This can be conceptually understood as Gaussian illumination utilizes a smaller portion of the primary aperture to give a smaller effective aperture size. Furthermore, diffraction power scales with power of the beam at the diffracting edge, thus a truncated beam at the edge will consequently send less power to the sidelobes. An careful assessment of the illumination profile relative to the primary aperture of an optical system must be carried out to produce a tight beam for resolving power, while minimizing power in the sidelobes.

To understand the coupling between the telescope and receiver optics, we work in reverse-time starting from the detectors. We approximate the far-field beam intensity with a Gaussian function, assumed to be a TEM mode solution to the paraxial Helmholtz equation in the small angle limit given by[2],

$$I\left(\vec{r}\right) \propto \exp\left(-\frac{1}{2}\frac{x^2 + y^2}{w(z)^2}\right) \tag{2.8}$$

where $w(z)$ is the beam width given by,

$$w(z) = w_0\sqrt{1 + \frac{z}{z_r}}. \tag{2.9}$$

---

[2] The expression given only shows the decaying transverse exponential, not the leading phase and amplitude terms and parabolic approximation to the spherical wave in the full solution

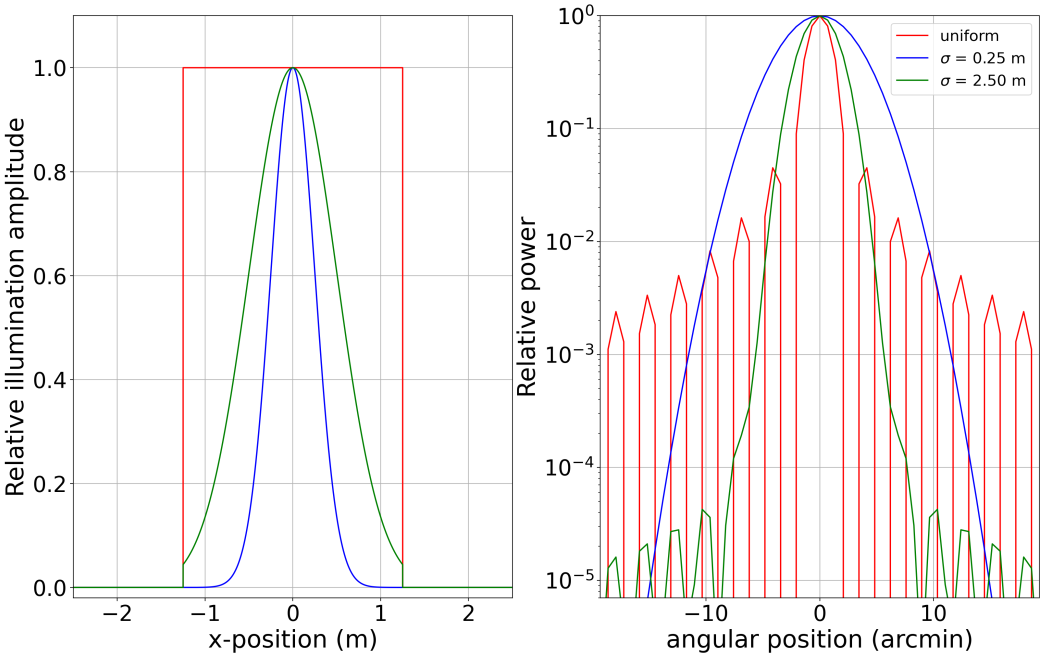

Figure 2.2: Aperture function (*left*) and the resulting far-field beam (*right*), calculated using Equation 2.7. A variety of different illumination profiles on a 2.5 m aperture are shown, including uniform illumination (*red*) and Gaussian illumination of $\sigma = 0.25$ m (*blue*) and 0.5 m (*green*). While uniform illumination produces the tightest beam, it also produces sidelobes of much larger power relative to Gaussian illumination. Gaussian illumination which is truncated by the edge of the aperture produces sidelobes of larger power relative to that which is not, since it utilizes a larger portion of the aperture. In determining the primary aperture illumination profile of an optical system, an optimization must occur to utilize the majority of the aperture area without truncating the beam at high power.

In the expression above, w_0 is the beam waist and z_R is the Rayleigh range given by $z_R = \pi w_0^2/\lambda$. Equation 2.8 shows that the field is parameterized solely by the beam waist, the size at the focus of the optical system and intriguingly, the tighter the beam waist, the more rapidly it diverges. This divergence is characterized by,

$$\theta_0 = \frac{w_0}{z_R} = \frac{\lambda}{\pi w_0}, \tag{2.10}$$

the $1/e^2$ irradiance diameter and $1/e$ diameter of the field amplitude[3].

---

[3] This diameter is different from σ used to define a Gaussian spread in Figure 2.2. A $1/e^2$ irradiance diameter contains 86% of the power while 1-σ contains 68% of the power.

To understand how the optical elements affect the light rays, we start with the beam waist to determine how the beam propagates towards the optical chain and then combine with physical optics simulations. Any real world optical system will produce aberrations. A system which has suppressed the effects of aberrations to below that of diffraction is considered diffraction-limited. A diffraction-limited system is preferred since modeling diffraction is significantly more straightforward than aberrations. As shown, Airy patterns are well approximated by a Gaussian beam profile and are typically characterized by symmetries that are well understood from the nature of Fourier transforms. In contrast, effects of aberrations are dependent on the specific optical element which alter the beam properties asymmetrically across the focal plane without a sufficient model and compromises the optical resolution. Strehl ratio, S, is a measure of the quality of an image formed by an optical system and is a commonly used figure of merit which defines a diffraction-limited system. It takes a value between 0 and 1, where a perfectly unaberrated system is characterized by $S = 1.0$. It is common practice to consider a lens to be diffraction limited when the $S > 0.8$. Strehl ratio is traditionally defined as the ratio of the peak intensity of the aberrated source image to the peak intensity of an image produced by an ideal optical system, limited only by diffraction, from its aperture, as illustrated in Figure 2.3. For example, aspheric lenses of Simons Array are manufactured with surface errors that affect the image beam profile and will degrade the Strehl ratio. Strehl ratio is more practically defined using the transmitted wavefront offset δ from an on-axis point source compared to the wavefront of an unaberrated system over an aperture, $A(x, y)$. Using Fourier optics to compare the phase terms,

$$\begin{aligned} S &= \left| \int_{\mathrm{A}} e^{i 2\pi \frac{\delta(x,y)}{\lambda}} dA \right|^2 \\ &\approx e^{-(2\pi\sigma)^2} \end{aligned} \tag{2.11}$$

where σ is the RMS phase deviation over the entire aperture and is used to statistically approximate the Strehl ratio. This approximation is used by ZEMAX[4], a popular physical optics simulation software used by Simons Array.

There are varying levels of aberrations dependent on the FOV and focal plane position. The area of the focal plane and its corresponding FOV on the sky in which the effects of aberrations are sub-dominant to those of diffraction such that $S > 0.8$ is called the diffraction-limited field of view (DLFOV). The detectors are only placed within this area to sustain high fidelity imaging performance of the optical system.

2.3 Optical Power

We outline some measurement quantities which describe how optical power from the sky, ground, and receiver travels through the optical elements to be seen by the detector. Assuming the elements of the optical chain are blackbody emitters in thermal equilibrium,

---

[4] https://www.zemax.com

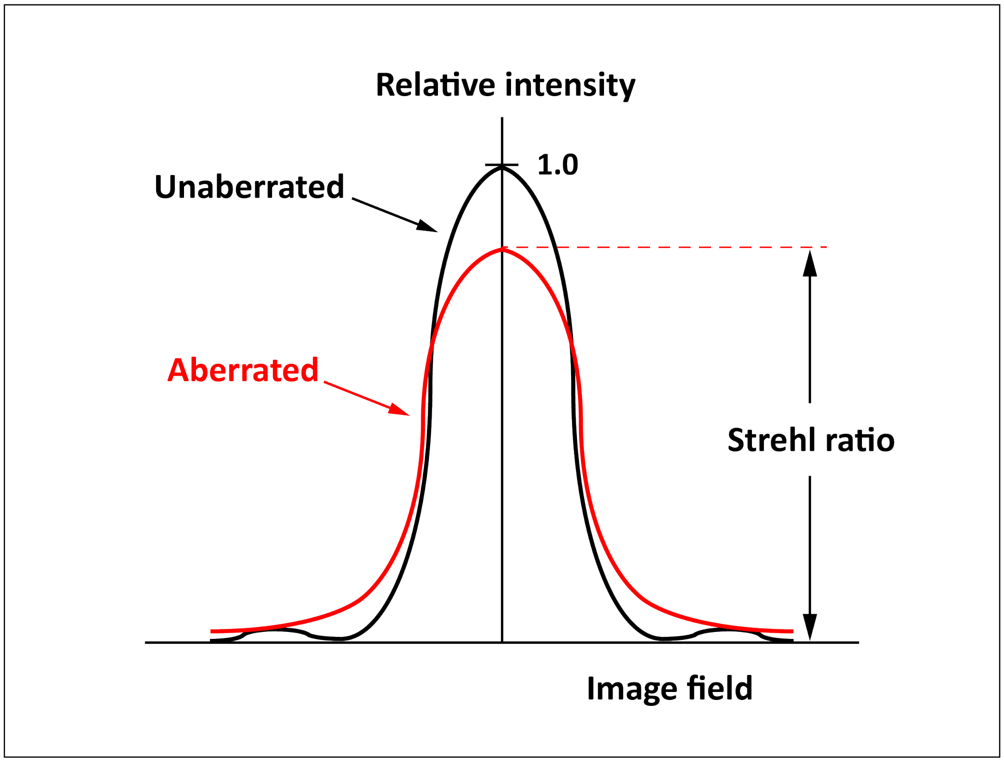

Figure 2.3: Illustration of a definition of Strehl ratio showing the degradation of the peak amplitude of the main beam with respect to that of a perfectly unaberrated beam. The y-axis is scaled to the intensity of the unaberrated, Airy pattern peak (*black*) such that Strehl ratio is defined as the peak amplitude of the aberrated beam on the image plane. Strehl ratio > 0.8 is typically defined as characterizing a diffraction-limited optical system.

we describe the four primary contributors to the detector's optical load. Figure 2.4 illustrates these contributors.

Emission and Absorption

Emissivity is the measure of a surface and its effectiveness in emitting energy through thermal radiation. A dielectric is an insulator, characterized by its complex permittivity, given by

$$\hat{\epsilon} = \epsilon' - i\epsilon'' \tag{2.12}$$

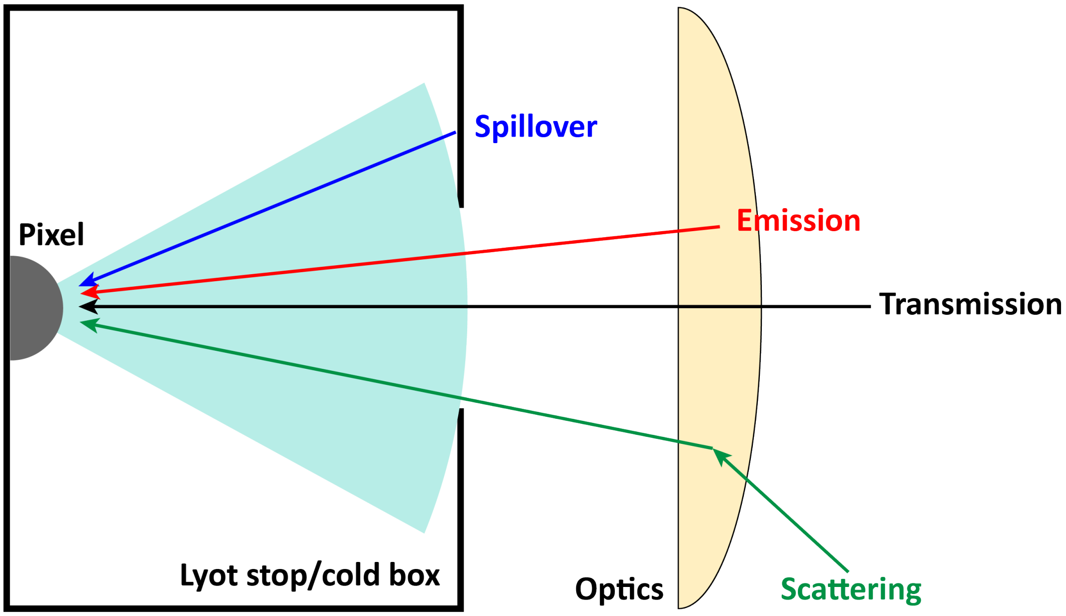

Figure 2.4: An illustration of the contributors to the detector's optical load in a forward-time sense. Emission (*red*), spillover (*blue*) and scattering (*green*) are mechanisms in which photons from sources other than the sky are seen by the detector. Transmission (*black*) is the propagation of CMB photons through the optical chain.

where ϵ' is the dielectric constant[5]. It relates to the loss tangent, tanδ, which denotes the dissipative loss of electrical energy through a dielectric in the following way,

$$\begin{aligned}\tan\delta &= \frac{2\pi\nu\epsilon'' + \sigma}{2\pi\nu\epsilon'} \\ &\approx \frac{\epsilon''}{\epsilon'}\end{aligned} \tag{2.13}$$

where σ is the conductivity and the approximation is valid for $\sigma/2\pi\nu\epsilon'' \ll 1$. The dielectric constant also relates to the index of refraction by $n = \sqrt{\epsilon'}$ for dielectrics[6] [7].

Under the assumption that these optical elements are blackbodies in thermal equilibrium, both absorption and emission are caused by the same thermodynamic excitations of a dielectric's molecules such that their fractional effect on input power are equivalent,

$$\alpha(\nu) = \frac{P_{\text{abs}}(\nu)}{P_{\text{in}}(\nu)} = \frac{P_{\text{emit}(\nu)}}{P_{\text{in}}(\nu)} = \varepsilon(\nu) \tag{2.14}$$

---

[5] Also referred to as the permittivity.

[6] After this section, the ' is dropped and the dielectric constant is simply referred to as ϵ.

[7] The dielectric constant is also often referred to as ϵ_r

where $\alpha(\nu)$ is absorptivity, $\varepsilon(\nu)$ is emissivity, $P_{\mathrm{abs}}(\nu)$ is power absorbed, $P_{\mathrm{emit}}(\nu)$ is power emitted, and $P_{\mathrm{in}}(\nu)$ is input power. As such, loss tangent parameterizes both absorption and emission as

$$\alpha(\nu) = 1 - \exp -\frac{2\pi\nu\sqrt{\epsilon'}t}{c}\tan\delta \tag{2.15}$$

where t is optical thickness. Thus, emissivity leads to both signal attenuation through absorption and parasitic detector loading through thermal emission, therefore is minimized at the design level to maximize optical throughput and minimize noise of the detectors. The emission power of a surface and the absorption of CMB photons scales with temperature, requiring the dielectric optical elements to be cryogenically cooled to 4 K and below.

Scattering

Scattering describes a broad category of physical processes in which photons interact with localized non-uniformities in the medium through which they propagate and deviate from their initial trajectories. Among this broad category and its many mechanisms of scattering, CMB instrumentalists are primarily concerned with the scattering of light from inhomogeneities of the dielectric media known as Mie scattering and from surface irregularities of the reflectors, governed by the Ruze equation. Just as we did with emissivity and absorptivity, we characterize the scattering fraction as

$$\gamma(\nu) = \frac{P_{\mathrm{scat}}(\nu)}{P_{\mathrm{in}}(\nu)}. \tag{2.16}$$

Mie scattering in which the scattering inhomogeneity is much smaller than λ, a good approximation for mm-waves and the characterized inhomogeneities of Simons Array's dielectrics, reduces down to the Rayleigh approximation. For a dielectric medium with index of refraction, n_1, and inhomogeneities of index of refraction, n_2, and diameter, d, the scattering cross-section is given by

$$\sigma_{\mathrm{Rayleigh}} = \frac{2\pi^5}{3}\frac{d^6}{\lambda^4}\left(\frac{n_2^2 - n_1^2}{n_2^2 + 2n_1^2}\right)^2. \tag{2.17}$$

The fractional attentuation of input power due to this scattering cross-section is given by,

$$\gamma(\nu) = 1 - e^{-\sigma_{\mathrm{Rayleigh}}Nt} \tag{2.18}$$

where N is the number density of scattering inhomogeneities and t is the optical thickness of the dielectric medium. Unlike absorption loss, scattering is not suppressed through cryogenic cooling of the optics and thus is critical to minimize at the design level. An analytical calculation of potential scattering power from re-imaging lens coatings are assessed in Section 5.4.

The Ruze equation describes the fractional scattering of light from reflectors as

$$\gamma(\nu) = 1 - \exp\left[\left(\frac{4\pi\delta\nu}{c}\right)^2\right] \tag{2.19}$$

where δ is the RMS surface error. This term is often negligible for terrestrial experiments where it is typically sub-dominant to other sources of loading on detectors.

With respect to detector loading, it is best imagined in the reverse-time paradigm. The vectors shown in Figure 2.4 can be reversed such that power propagates out from the detectors towards the sky but some rays terminate elsewhere, such as the ground or cryostat shell wall, due to scattering. because the detector sees a non-optical surface, photon power from those surfaces within the detector's FOV are detected and dissipate non-CMB power on the bolometer, contributing to the detector's noise level. Furthermore, scattering through the optical chain can generate undesirable sidelobes and degrade the resolving power of the system.

Spillover

Spillover describes incident light rays on surfaces outside of the optically viable area which sees the sky. We quantify the fraction power of spillover as

$$\beta\left(\nu\right) = \frac{P_{\text{spill}}(\nu)}{P_{\text{in}}(\nu)} \tag{2.20}$$

where $P_{\text{spill}}(\nu)$ is spilled power. Just as we discussed with respect to the scattering fraction, $\gamma(\nu)$, spillover is best conceptualized in reverse-time. Some fraction of light rays from a detector falls outside an optical element's optically viable surface, as seen in Figure 2.4, and terminates elsewhere such as the mounting flange of a lens. This means that the non-optical surface emits photons towards the detector and non-CMB power is dissipated on the bolometer. Typically, spillover power terminates on non-optical surfaces such as the inner wall of the cryogenic receiver, baffling surfaces, telescope structure, and the ground. Spillover power is calculated at every aperture in an optical system such that spillover on ambient temperature surfaces can be mitigated. Furthermore, cryogenic radio-frequency absorbers within receivers are utilized to prevent undesirable, ambient temperature spillover. As it will be shown in Section 4.1, we design the optics using physical optics simulation software such that the ray trace footprint has large margins within the optically-viable surfaces and away from everywhere else.

Reflection

Reflectivity quantifies the power reflected of the incident power by a dielectric, given by

$$\rho\left(\nu\right) = \frac{P_{\text{refl}}(\nu)}{P_{\text{in}}(\nu)} \tag{2.21}$$

where $P_{\text{refl}}(\nu)$ is reflected power. Reflection, similar to scattering, attenuates signal through the optical chain and produces sidelobes. We discuss this in more detail in Section 5.

Transmission

Transmissivity of a surface or dielectric describes its effectiveness in transmitting incident radiation, defined as

$$\eta\left(\nu\right) = \frac{P_{\mathrm{trans}}(\nu)}{P_{\mathrm{in}}(\nu)} \tag{2.22}$$

where $P_{\mathrm{trans}}(\nu)$ is reflected power. In terms of all the quantities described above, conservation law requires that

$$\eta\left(\nu\right) = \left[1 - \alpha\left(\nu\right)\right]\left[1 - \beta\left(\nu\right)\right]\left[1 - \gamma\left(\nu\right)\right]\left[1 - \rho\left(\nu\right)\right]. \tag{2.23}$$

As one may infer, a core design principle for astronomical optics is to maximize transmittance through every element of in-band photons by minimizing everything else as the sole contributor of detector loading[8].

Optical throughput is the total transmission through the entire telescope system, defined as

$$\eta_{\mathrm{thru}} = \prod_{i}^{N_{\mathrm{elements}}} \eta_i \tag{2.24}$$

where N_{elements} includes all optical elements starting with the detector. However, CMB receivers will typically implement an aperture stop to truncate the beam, which also reduces the throughput of the system. Optical efficiency takes into account this reduction, defined as

$$\eta_{\mathrm{eff}} = \frac{\eta_{\mathrm{thru}}}{\eta_{\mathrm{apert}}} \tag{2.25}$$

where η_{apert} is the aperture efficiency. This definition takes into account the beam truncation as

$$\eta_{\mathrm{apert}} = \frac{\int}{\int} = 1 - \exp\left[-\frac{r}{r}\right]. \tag{2.26}$$

While a system with perfectly efficient optical elements can have $\eta_{\mathrm{eff}} = 1$, optical throughput is still limited by beam truncation such that an identical system would be characterized by $\eta_{\mathrm{thru}} = 1 - \eta_{\mathrm{apert}}$.

---

[8] With the exception of the aperture stop which is introduced in the following chapter

Chapter 3

Simons Array

Precision measurements of CMB polarization anisotropies require polarimeters which can image the sky with high sensitivity and low systematic bias. Modern CMB detectors are photon-noise limited, meaning their sensitivity is bound by the arrival statistics of photons rather than from the internal noise of the instruments. Therefore signal-to-noise improvements have been driven by increasingly larger detector count whose signals are coadded to reduce background noise. As detailed in Section 1.7, instrumentalists must also enable broadband observation with a multichroic receiver for component separation of the CMB and its foregrounds. Illuminating a large format, multichroic detector array for high fidelity, low systematic mapping of CMB polarization presents a variety of instrumental challenges from the optics down to the readout electronics. Simons Array builds upon the foundation and accomplishments of POLARBEAR by upgrading its receiver and adding two more telescopes to form an array of three multichroic polarimeters: POLARBEAR-2a, POLARBEAR-2b, and POLARBEAR-2c. The observation bands of Simons Array are centered at 95, 150, 220, and 280 GHz within the atmospheric windows, as shown in Figure 3.1. Note that the POLARBEAR upgrade was originally referred to as POLARBEAR-2 and later referred to s POLARBEAR-2a within the context of Simons Array. Its sensitivity is concentrated at 95 and 150 GHz bands, with POLARBEAR-2a and POLARBEAR-2b both observing at 95 and 150 GHz and POLARBEAR-2c observing at 220 and 280 GHz. Simons Array occupies a unique position to observe at both the small angular scales of gravitational lensing of the CMB and the large angular scales of the primordial B-mode at the recombination bump.

The planned survey areas are designed to minimize foreground contamination from galactic disc emission, with particular focus on the southern galactic hole. These survey patches will be cross-correlated with surveys of overlapping fields such as the Simons Observatory Small Aperture Telescope [20] and Hyper Suprime-Cam of the Subaru Telescope [11].

Some projected 1-σ constraints from Fisher matrix forecasts are as follows [19].

- $\sigma(r) = 0.006$ and will measure down to r 0.01 with 5σ significance.
- $\sigma(\sum m_\nu) = 40$ meV when combined with DESI.

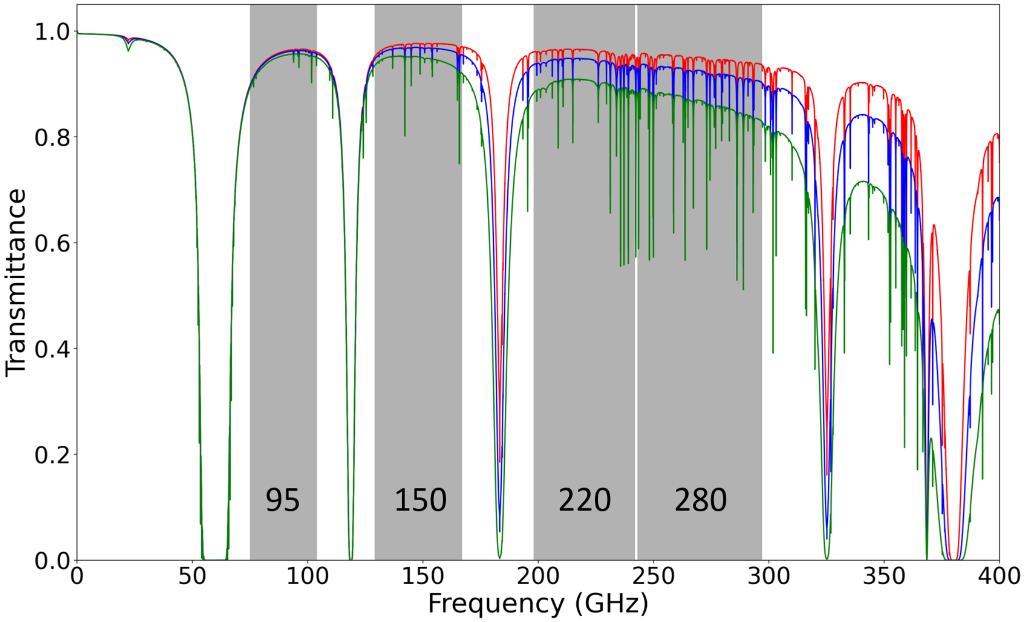

Figure 3.1: Simons Array observation bands are chosen within atmospheric windows.

- $\sigma(n_s) = 0.0015$ using its high fidelity EE power spectrum[1]

3.1 Observation Site

As discussed in Section 1.7, choosing a site with the minimum PWV level is crucial for minimum signal attentuation and thermal emission. Simons Array is located on the slopes of the Cerro Tocco in the Atacama Desert of Chile. Observing at an altitude of 5200 meter results in extremely dry conditions for CMB signal to reach the telescopes. Furthermore, its latitude of $\sim 23°$ allows Simons Array to see nearly 80% of the sky, reducing the constraints of cosmic variance and providing opportunities for cross correlation with other surveys. The median PWV value for POLARBEAR-1's second season was 1 mm [33].

3.2 Telescope

The POLARBEAR-2c receiver replaces the POLARBEAR receiver and is installed on the Huan Tran Telescope. The POLARBEAR-2a and POLARBEAR-2b receivers are installed

---

[1] n_s is the scalar spectral index of the slow-roll parameters describing the single-field slow-roll inflation model.

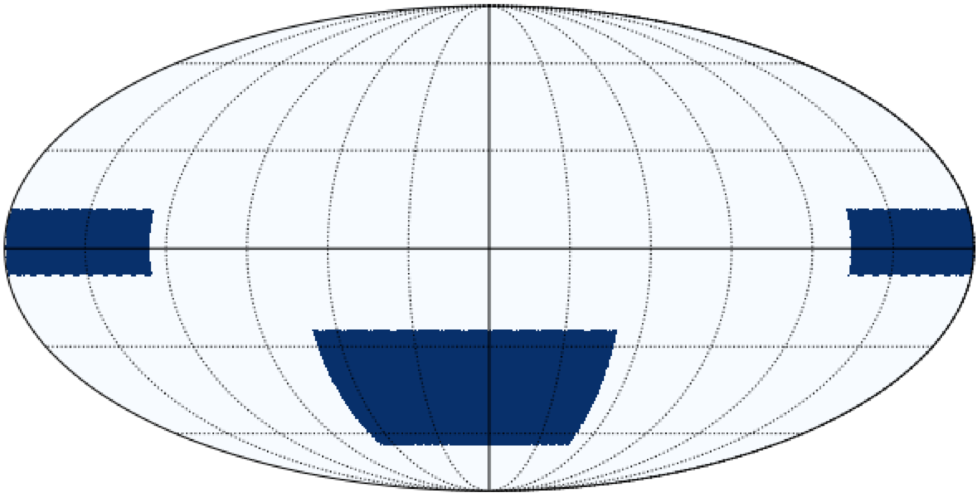

Figure 3.2: Approximate Simons Array survey maps, shown in equatorial coordinates, are chosen to avoid dusty regions of the sky and minimize polarized foreground contamination. Figure courtesy of Yuyang Zhou.

on the newly built Nicholas Simons Telescope and Paul Simons Telescope, respectively, which share identical reflector designs to that of the Huan Tran Telescope. The telescope design consists of a parabolic primary mirror and elliptical secondary mirror, arranged in an off-axis Gregorian Dragone configuration which satisfies the Mizuguchi-Dragone condition to minimize cross-polarization systematics and aberrations over a large FOV. The primary reflector has a 2.5 m diameter made of monolithic aluminum and machined to 53 μm accuracy. The surface roughness, while not the limiting factor for terrestrial telescopes, can induce unwanted sibelobes or parasitic loading on detectors from Ruze scattering, as discussed in Section 2.3. The FOV of POLARBEAR-2 is 4.5° [2] and the beam size is 5.2 and 3.5 arcsecond for 95 and 150 GHz bands, respectively, and 2.8 and 2.2 arcsecond for 220 and 280 GHz bands, respectively. The lower precision guard ring panels extend out to 3.5 m diameter. While the majority of the Gaussian-like truncated beam from the receiver illuminates the primary reflector, it also illuminates the guard rings at $\sim$ -10 dB power relative to the peak power. This spillover power is directed to the sky, mitigating potential spillover of this beam edge from seeing the ambient temperature ground. Thus the primary along with its guard ring results in a tight angular resolution on the sky while decreasing power in the diffraction sidelobes, a notion of optical design described in Section 2.2.

As seen in Figure 3.4, the telescope also contains a co-moving ground shield, prime focus baffle, and secondary mirror enclosure. The co-moving ground shield prevents the detectors from seeing the ground while the prime focus baffle and secondary mirror enclosure prevents

---

[2] As will be shown in later sections, FOV is technically larger for lower frequencies but vignetting by finite size of optical elements realistically sets FOV to be the same for all bands

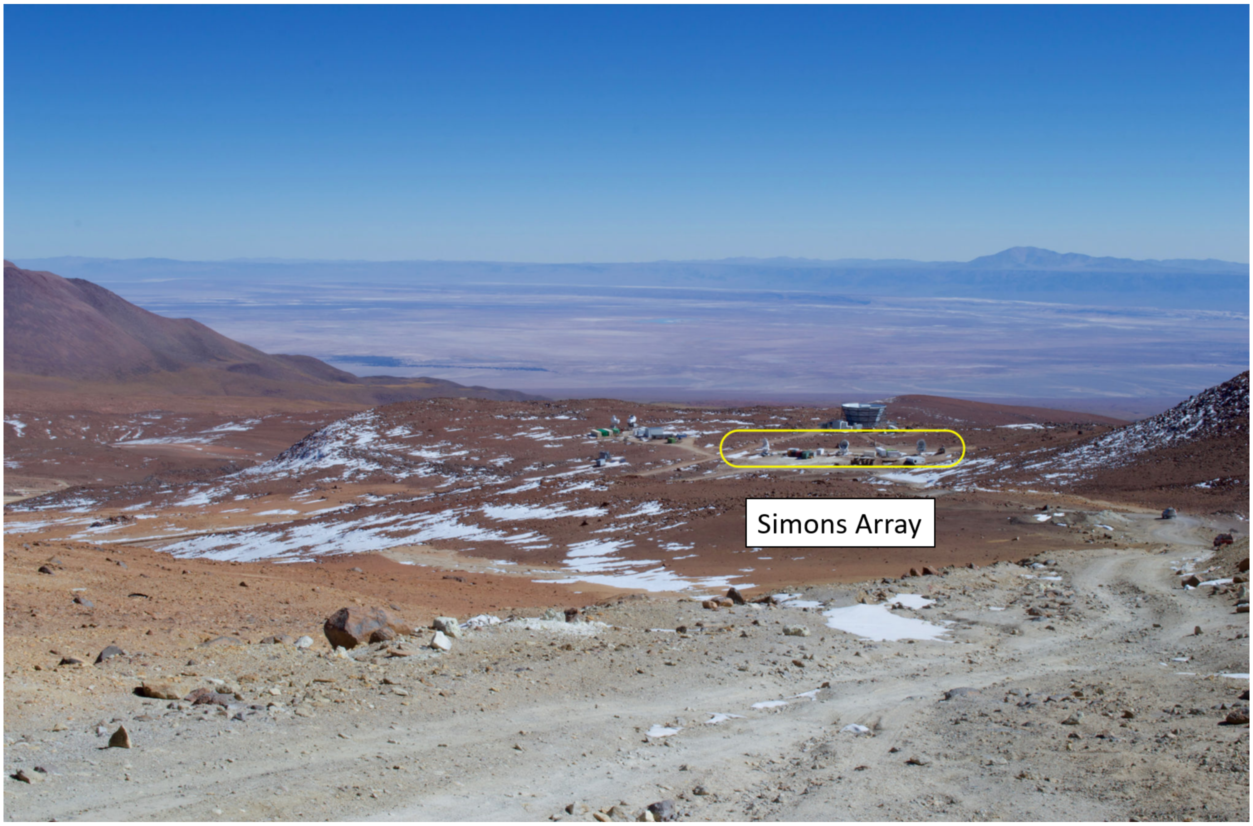

Figure 3.3: Simons Array at the Cerro Toco Atacama observation site. Photo courtesy of Tom Ayotte.

the detectors from seeing the surrounding environment through spillover from the receiver and secondary mirror.

3.3 Re-imaging Lenses

In order to produce telecentric rays spanning the width of the detector array, large format re-imaging lenses are placed at the output of the pair of reflectors. Three lenses - the field lens, aperture lens, and collimator lens - are used to form an image of the primary at the cold aperture stop, called the Lyot stop, and a high fidelity, telecentric image of the sky at the focal plane. These lenses are made of polycrystalline aluminum oxide Al_2O_3 which is characterized by its high index of refraction and low loss tangent. The Lyot stop is a black body, sharp aperture placed in the optical chain to define the beam of the receiver, as described in Section 2.2. The lenses and Lyot stop are cooled to $\sim$4 K to maximize optical throughput and minimize emissive thermal loading. In particular for the Lyot, this is critical as its cryogenic aperture hides ambient temperature telescope structure from the detector

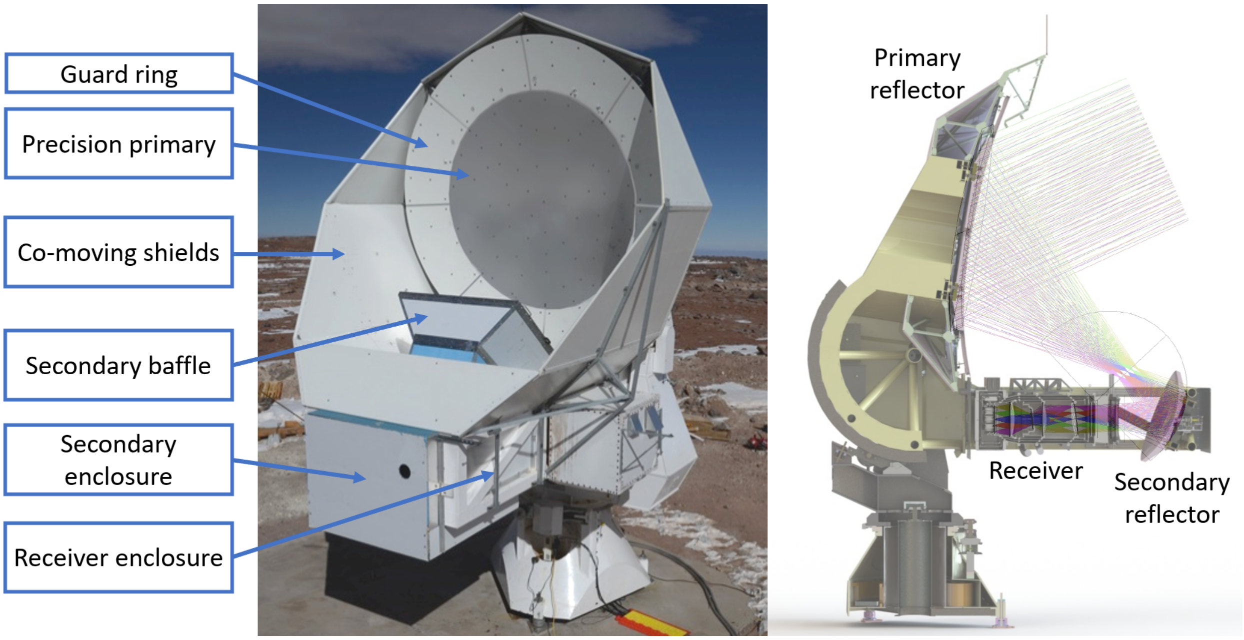

Figure 3.4: The Huan Tran telescope and a ray trace of a Simons Array optical system.

array's FOV. In order to suppress reflection at the dielectric boundaries of the lens surfaces, a 2-layer AR coating is applied on every surface, achieving ∼1% reflection per lens.

3.4 Cryogenic Design

A Simons Array receiver cools multiple lenses, filters, and detector array. As shown in Figure 3.5, the receiver consists of two cryogenic sub-components: the optics tube, the tubular section which houses the optical elements, and the backend, the detector box which contains the detectors and readout components. A pulse tube cryocooler (PTC) from Cryomech[3] is used to cool each sub-component at two temperature stages, 4 K and 50 K, with approximately 35 W and 1.5 W of cooling power, respectively. Adjacent aluminum shells, anchored to each temperature stage of the PTC, are utilized in the design to minimize radiative and conductive loads on each heat sink stage. Each shell is mechanically supported by the hotter adjacent shell using conductively insulating G-10 rods and covered with multi-layer insulation (MLI) blankets made of aluminized mylar to reduce radiative loading.

The optical chain of each receiver begins with a vacuum window which is transparent to in-band photons but also acts as the first infrared (IR) filter. POLARBEAR-2a and POLARBEAR-2b uses Zotefoam windows[4], an expanded high-density polyethylene (HDPE) foam,

---

[3] https://www.cryomech.com

[4] https://www.zotefoams.com

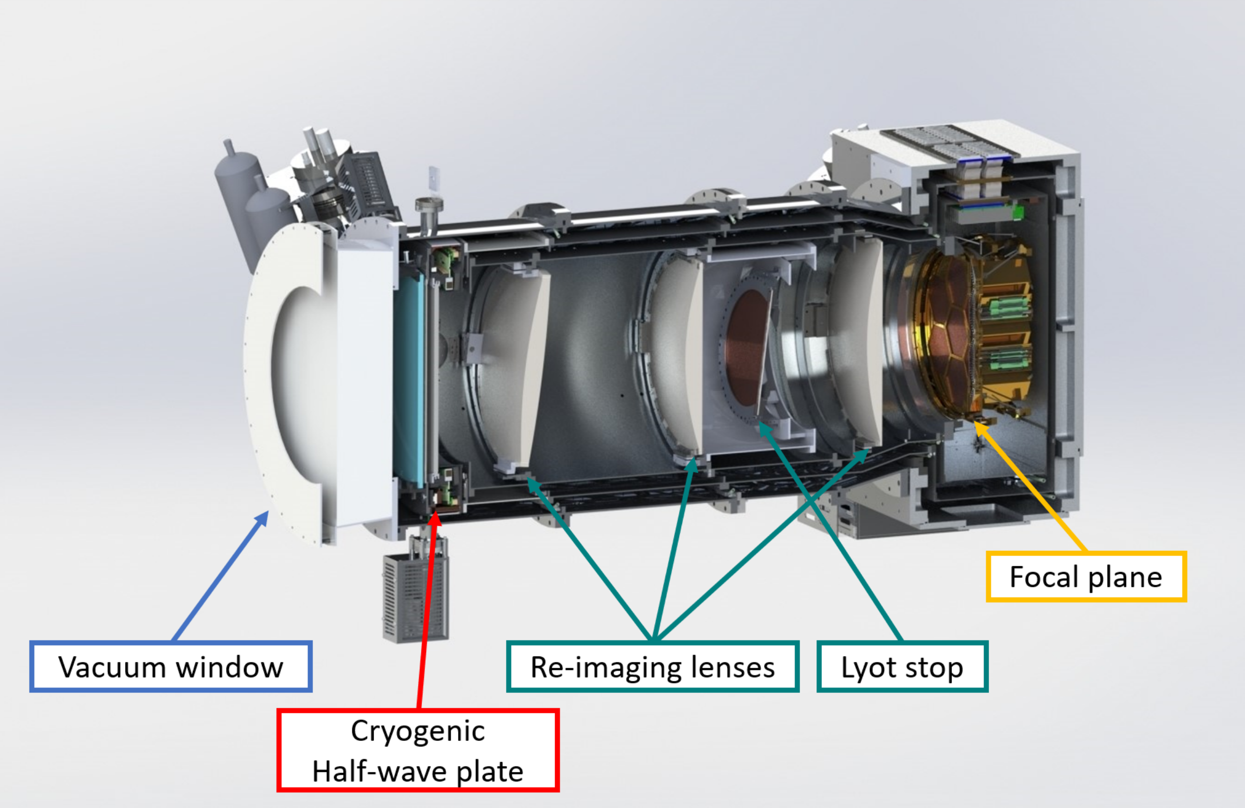

Figure 3.5: CAD cross-section of a POLARBEAR-2b receiver showing ambient temperature vacuum window and RTMLI infrared shader, 50 K alumina IR filter and half-wave plate system, 4 K re-imaging lenses and lyot stop, and the mK focal plane. In terms of components, the POLARBEAR-2a receiver is slightly shorter with an ambient temperature half-wave plate outside of the cryostat and the POLARBEAR-2b receiver utilizes a thin UHMWPE vacuum window.

and POLARBEAR-2c uses a thin ultra-high-molecular-weight polyethylene (UHMWPE) window due to the high scattering rate of commercially available polyethylene foams. Immediately behind the window is a stack of radio-transparent multi-layer insulation (RTMLI) for IR filtering which consists of layers of polystyrene foam. This low index of refraction foam is transparent to millimeter waves but acts as conventional multi-layer insulation to IR radiation [13] where each layer successively blocks more power. A 2 mm thick alumina filter, anchored to the sky-side of the 50 K shell, further filters out-of-band IR power. The alumina lenses provide additional IR filtering before the detector. Finally, multiple low-pass metal mesh filters (MMF), made of alternating layers of metal mesh and polyethylene with each metal mesh acting as a lumped circuit element in a free space transmission line, are placed at the Lyot stop and directly in front of the detector array. Determination of the number of RTMLI layers and low pass filter cutoff frequency of the MMF depends on the thernal environment of each cryostat and will be expanded upon in Section 4.3.

A multi-stage helium sorption refrigerator is placed on the 4 K PTC heat sink of the backend to provide additional cooling for the detector array and its MMF. This cooling system brings the temperature of the detectors down to $T = 300$ mK with intermediate heat sinks via a closed cycle adsorption pumping on liquid He-3 and He-4. The system periodically recycles helium buy using dissipative resistors and gas-gap heat switches on the adsorption pump. The sorption refrigeration systems are provided by Chase Research Cryogenics[5] with slight differences between each receiver. POLARBEAR-2a uses the Berkeley-10 design, POLARBEAR-2b uses the Gas-Lite 10 design with a custom single stage He-4 booster fridge, and POLARBEAR-2c uses the Gas-Lite 10 design with additional helium charging.

3.5 Detectors

Focal Plane Optics

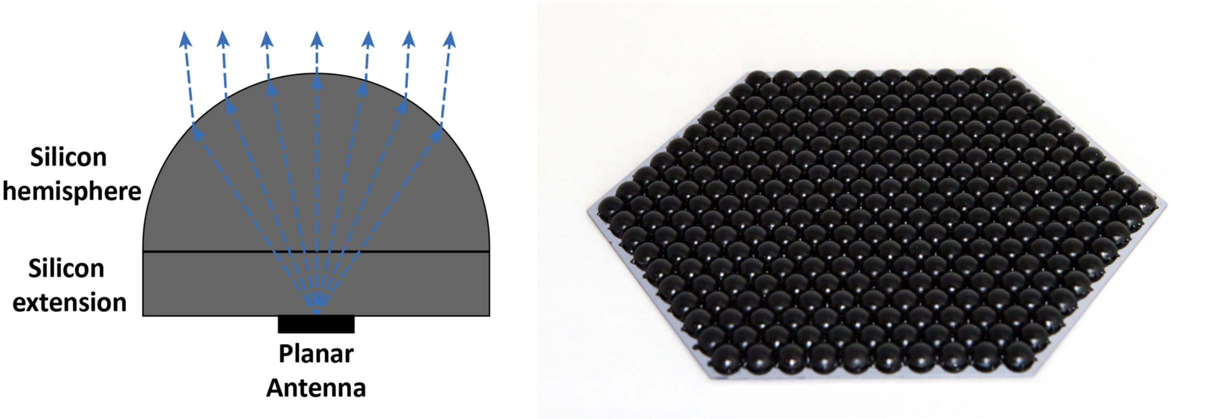

Figure 3.6: A schematic diagram showing the design of the extended hemispherical silicon lenslet (*left*) and a picture of a fully assembled POLARBEAR-2a lenslet array (*right*), courtesy of Praween Siritanasak.

The focal plane optics focuses and feeds the sky image, coming from the output of the re-imaging lenses, to the detectors. Each Simons Array detector array consists of seven detector wafers, each wafer containing 271 detector pixels. Each pixel is sensitive to two orthogonal polarization states and two frequency bands, or “colors,” of 95 and 150 GHz or 220 and 280 GHz. This means there are four optical detectors per pixel and 7,588 detectors per receiver. The detector pixel uses a planar sinuous antenna as its sensing element which

---

[5] https://www.chasecryogenics.com

is optically coupled to the telescope using an extended hemispherical silicon lenslet [21]. Combined with the silicon wafer containing the detectors and the spacing wafer, the silicon hemisphere approximately acts as an ellipsoidal lenslet, focusing the beam onto the antenna as shown in Figure 3.6.

The sinuous antenna is a broadband, log-periodic antenna whose overall size and smallest features determine the edges of its bandwidth. Signals from the antenna travels on microstrip lines through on-chip bandpass filters and then finally dissipated via Joule heating as thermal power on the bolometer thermistor [63].

Transition Edge Bolometer

The thermistor described above is a thin-film superconductor, called the transition edge sensor (TES) bolometer, which is voltage-biased such that the RMS electrical power on the bolometer is given by

$$P_{\text{bias}} = \frac{V_{\text{bias}}^2}{R_{\text{bolo}}} \tag{3.1}$$

where V_{bias} is the bias voltage and R_{bolo} is the operating resistance of the bolometer. As Figure 3.7 shows, the bolometer also receives optical power from the microstrip line such that

$$P_{\text{tot}} = P_{\text{bias}} + P_{\text{opt}} \tag{3.2}$$

where P_{opt} is optical power. For small signals, the behavior of the bolometer in response to the power input is linear and we can look at a single Fourier mode of the time-varying optical power from the sky. The power flow on a bolometer is then given by

$$P_{\text{tot}} + \delta P_{\text{opt}} e^{i\omega t} + \frac{dP_{\text{bias}}}{dT_{\text{bolo}}} e^{i\omega t} = G\left(T_c - T_b\right) + \left(g + i\omega C\right)\delta T_{\text{bolo}} e^{i\omega t} \tag{3.3}$$

where $g = \delta P / \delta T$ is the dynamic thermal conductance, C is the bolometer heat capacity, T_b is the bath temperature, and G is the conductivity of the weak thermal link to the bath, as shown in Figure 3.7. The first term on the right hand side is the saturation power, P_{sat}, which is the power dissipated to the thermal bath. The left hand side represents power from the sky and bias voltage, while the right hand side represents the power to the thermal bath and time-dependent energy of the bolometer island's thermal mass. Further re-writing Equation 3.3 with

$$\frac{dP_{\text{bias}}}{dT} = \frac{d\left(V_{\text{bias}}^2 / R_{\text{bolo}}\right)}{dT} = -\frac{V_{\text{bias}}^2}{R_{\text{bolo}}^2}\frac{dR_{\text{bolo}}}{dT} = -\frac{\alpha P_{\text{bias}}}{T_c} \tag{3.4}$$

where $\alpha \equiv dlnR/dlnT$ of the bolometer and $T_{\text{bolo}} = T_c$ for bolometer operation. With Equation 3.4, Equation 3.3 simplifies to

$$\delta P_{\text{opt}} = \left(\frac{\alpha P_{\text{bias}}}{T_c} + g + i\omega C\right)\delta T \tag{3.5}$$

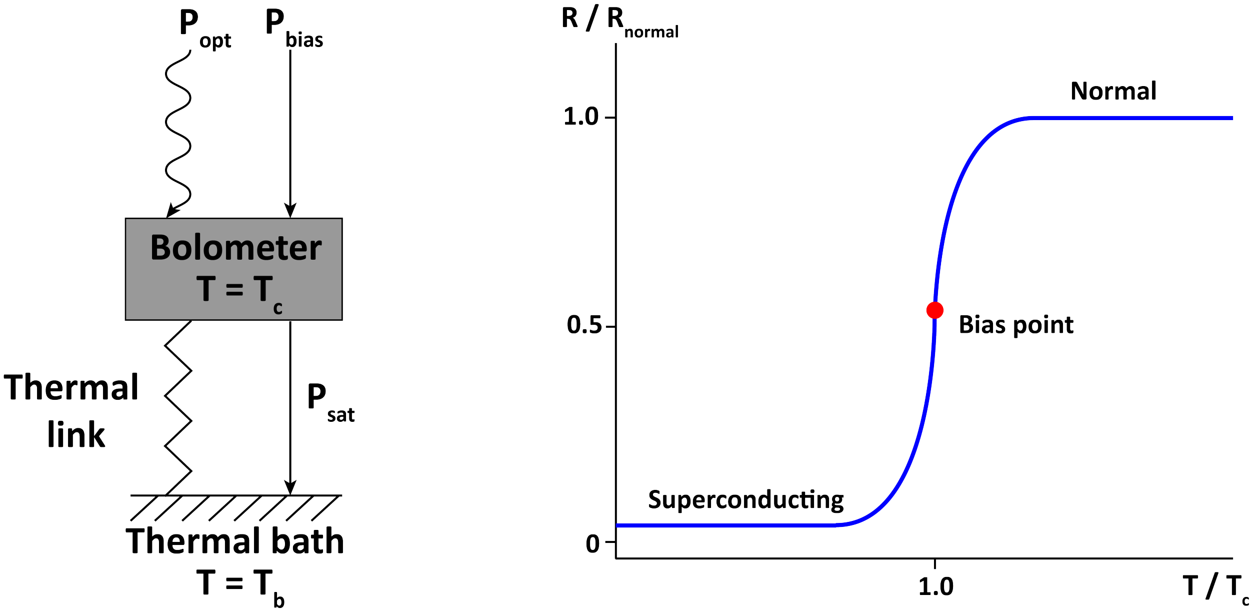

Figure 3.7: A schematic diagram of a voltage-biased antenna-coupled TES bolometer (*left*) and its R vs T curve for operation (*right*). The TES bolometer receives both optical power P_{opt} and electrical power P_{bias} while weakly thermally coupled to a bath of temperature, $T = T_b$. When P_{opt} increases to move the bias point towards the right, P_{bias} decreases to provide negative electrothermal feedback, and vice-versa. Thus, during normal operation, $P_{\text{opt}} + P_{\text{bias}} = P_{\text{sat}}$.

which shows how fluctuations in optical power is converted to fluctuations in bolometer temperature.

For stable bolometer operation, P_{bias} is tuned such that $P_{\text{tot}} = P_{\text{sat}}$ before observation. In the instance P_{tot} exceed P_{sat}, T_{bolo} exceeds T_c and the bolometer saturates, while for the reverse case, the bolometer latches and is inoperable. Equation 3.4 shows how this is achieved in practice via negative electrothermal feedback. The bolometer self stabilizes when $\alpha > 0$ as P_{bias} moves in the opposite direction of P_{opt} when R_{bolo} and T_{bolo} increases, and vice-versa. Figure 3.7 illustrates this design principle for TES bolometers, $\alpha > 0$ and P_{bias} is adjusted according to fluctuations in P_{opt} for stable operation of the bolometer.

Under a voltage bias, the TES converts fluctuation in optical power to fluctuation in current, characterized by its responsivity

$$S_I \equiv \frac{dI_{\text{bias}}}{dP_{\text{opt}}} = -\frac{\tilde{S}_{\text{fact}}}{V_{\text{bias}}} \frac{\mathcal{L}}{\mathcal{L}+1} \frac{1}{1+i\omega\tau} \tag{3.6}$$

where $\mathcal{L} \equiv P_{\text{bias}}\alpha / gT_c$ is the open loop gain, $\tau \equiv \tau_0 / \left(\mathcal{L}+1\right) = \left(C/g\right) / \left(\mathcal{L}+1\right)$ is the time constant, and $\tilde{S}_{\text{fact}}$ is the responsivity factor,

$$\tilde{S}_{\text{fact}} = \begin{cases} 1 & \text{if DC bias} \\ \sqrt{2} & \text{if AC bias.} \end{cases} \tag{3.7}$$

In the limit of high loop gain ($\mathcal{L} \gg 1$),

$$S_I \approx \frac{\tilde{S}_{\text{fact}}}{V_{\text{bias}}} \tag{3.8}$$

and responsivity becomes solely dependent on the electrical bias parameters, simplifying the task of creating a large detector array with uniform responsivity. The inherent stability provided by negative electrothermal feedback allows for a very steep α curve, which in turn enables very large responsivity.

Some details on the Simons Array detectors are as follows. The detectors of Simons Array and other modern CMB experiments are fabricated using silicon-based photolithography. Radiation from the telescope excites the broadband sinuous antenna, which is a slot in the niobium (Nb) ground plane, and sends the signal to be filtered to band defining frequencies by a pair of lumped element filters by Nb microstrip lines. The radiation power is terminated by titanium resistors and converted to heat by palladium thermal mass, which is a high heat capacity metal deposited on the bolometer island. The TES is made of aluminum doped with $\sim$ 4000 ppm manganese to tune the critical temperature from 1.2 K to 440 mK. Silicon nitride legs make up the weak thermal link to the thermal bath. More details are found on [4].

TES Readout

Simons Array uses the digital frequency-division multiplexing (DfMux) in order to digitize and readout signals from many detectors. With such a large detector count and their wiring complexity, it necessitated a multiplexed readout scheme which would reduce the number of wires and consequently, the thermal load on the mK fridge, complexity, and cost. Simons Array can readout 38 detectors seeing the sky with a single wire. Each detector is connected in series with an LC resonator, creating a set of 38 unique, non-overlapping frequency peaks between 1 - 5 MHz, as illustrated in Figure 3.8. These frequency channels are AC voltage biased with a matching frequency comb of AC sinusoidal waveforms. The signals are then carried in the channels of the comb and amplified at 4 K using a single superconducting quantum interference device (SQUID) which is a low impedance, high gain transimpedance amplifier. A SQUID senses small changes in current of a bolometer by using a superconducting loop containing Josephson junctions to measure change in flux. Their low input impedance allows for bolometer operation at their low resistance of $\sim 1\Omega$.

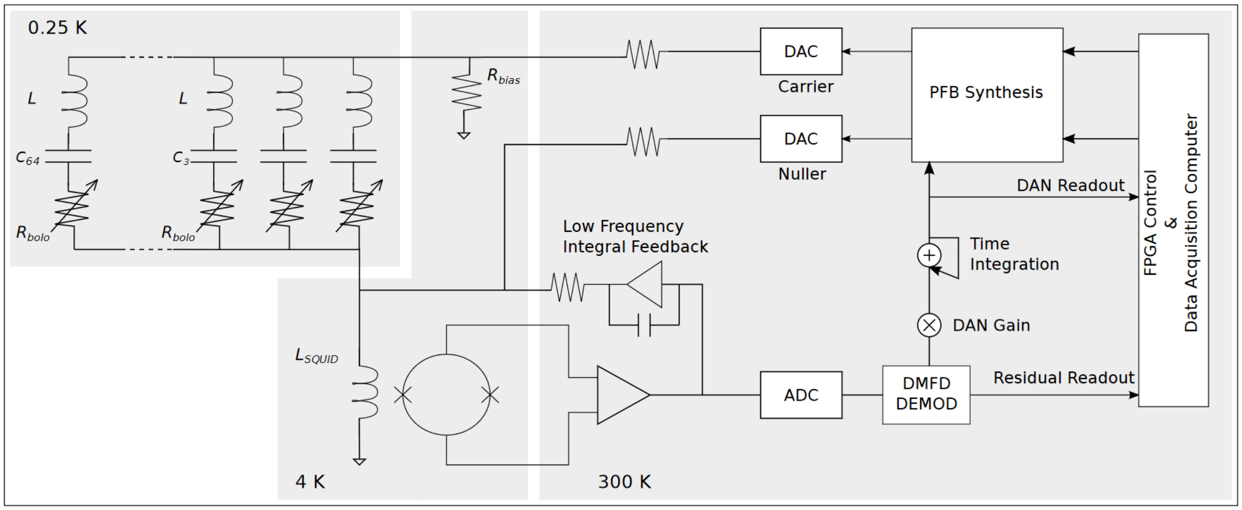

Figure 3.8: A schematic diagram of the dfMUX readout for Simons Array [1]. 38 bolometers are placed in series with matching LC resonators, each of which is tuned to a unique resonance frequency between 1 - 5 MHz to form a comb of peaks. These channels are AC voltage biased with a waveform of matching frequency whose output current waveforms are transimpedance amplified by a single SQUID to be further amplified and digitized with 300 K electronics.

3.6 Polarization Modulator

Building on the achievements of POLARBEAR which demonstrated the improvements in sensitivity over large angular scales of CMB polarization measurements by incorporating a continuously rotating half-wave plate (HWP) [23], Simons Array utilizes a birefringent sapphire stack as a polarization modulator at a focus of the telescope. This allows Simons Array's observation strategy to be flexible and sensitive over a large range of angular scales. While the inherent characteristics of a Simons Array telescope makes them very sensitive at small angular scales for lensing science, the HWP extends its accessible range of angular scales to $\ell \sim 50$ for inflationary science. One particular impediment is the presence of 1/f noise due to fluctuations of thermal emission from the atmosphere. The HWP modulates the polarized CMB signal to separate and up-sample to a frequency channel that is not contaminated with this low frequency noise. Furthermore, it allows Simons Array to avoid systematics which arise from beam-differencing pairs of orthogonal polarization sensitive detectors of the same pixel, as the HWP allows Simons array to measure both polarizations simultaneously. Simons Array achieves broadband polarization using an achromatic HWP with a Pancharatnam stack of monocrystalline sapphire plates [54].

There are major differences in the POLARBEAR-2a HWP and POLARBEAR-2b and -2c HWP designs. POLARBEAR-2a fields an ambient temperature HWP directly in front of the vacuum window. It is mounted on a ball bearing rotation stage, driven by a servo

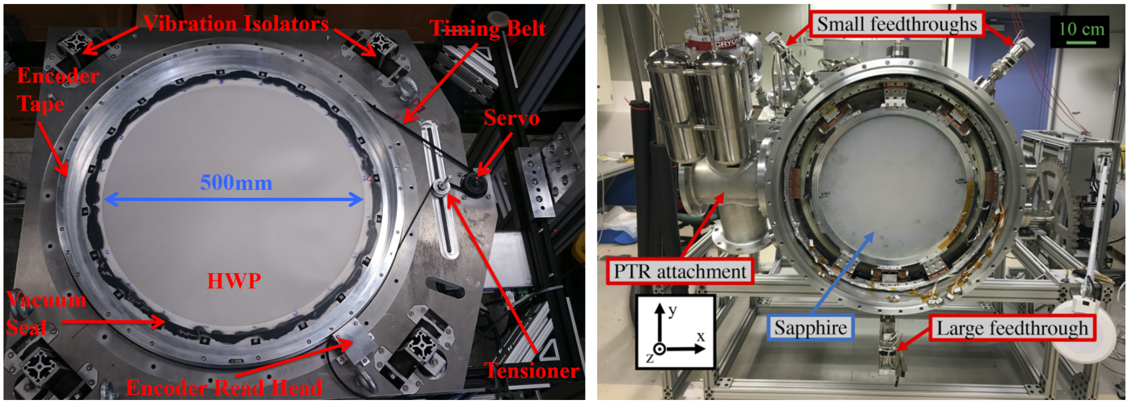

Figure 3.9: Pictures of the POLARBEAR-2a ambient temperature HWP (*left*) [6] and POLARBEAR-2b cryogenic HWP (*right*) [5], courtesy of Charles Hill.

motor coupled with a belt. The AR coating consists of 2 layers of plastic dielectrics, held in place with a co-rotating vacuum system to circumvent the use of glue layers which suppresses the HWP's transmittance and the receiver's sensitivity. POLARBEAR-2b and -2c implement a cryogenic HWP design to improve transmittance and reduce thermal emission. The sapphire plates and rotation mechanism are placed inside the receiver cryostat in front of the re-imaging lenses. The system is anchored to the 50 K stage of the optics tube for cooling. The rotation is driven by a magnetically levitating, super-conducting bearings, with retractable gripper arms designed to mechanically manipulate the HWP above the transition temperature.

3.7 Current status

The Simons Array telescopes been built and installed at the site in advance of the arrival of their receivers, with some receiver enclosure installations finished for the Huan Tran Telescope in 2021 and planned for the Nicholas Simons Telescope and Paul Simons Telescope. The validation and deployment of the cameras were planned in parallel for each optics tube and backend systems and in series following POLARBEAR-2a, then POLARBEAR-2b, and finally POLARBEAR-2c. The POLARBEAR-2a optics tube and backend were validated in KEK for deployment and commissioning in 2018. The remaining optics tubes were validated, as will be discussed in Section 4.3 in UC Berkeley while the backends were validated in UC San Diego. The POLARBEAR-2b receiver was integrated for deployment in UC San Diego in 2019 while the POLARBEAR-2c receiver integration is planned to occur in UC Berkeley.

The POLARBEAR-2a receiver went through a series of repairs throughout 2019 and 2020 until the COVID-19 pandemic halted any work, such that observations restarted in 2021. The POLARBEAR-2b receiver integration with its telescope was similarly halted in 2020 due to the COVID-19 pandemic. At the time of this writing, integration is underway and scheduled to finish for first light in October 2021. The POLARBEAR-2c receiver is ready for integration and commissioning at UC Berkeley.

Chapter 4

Simons Array Optics Tube

The Simons Array optics tube consists of the cryogenic shells and the optical elements within them. This chapter details the final design process, fabrication, and validation of the POLARBEAR-2b and POLARBEAR-2c optics and optics tubes.

4.1 Simons Array Optics

POLARBEAR-2 is an upgrade to the POLARBEAR receiver and shares the same telescope infrastructure, implementing an aggressive optical design with a larger DLFOV and detector count than its predecessor. This chapter details the design, fabrication, and testing of the Simons Array optics with focus on significant changes to the fiducial POLARBEAR-2 design. Figure 3.5 shows the cross-section of the optics tube, to be referenced throughout this chapter.

Alumina Optics

The POLARBEAR-2 receiver sees the sky with ~ 6 times as many detectors as POLARBEAR with 7,588 detectors and a 4.5° DLFOV compared to POLARBEAR's 3.0°. This design sustains the high fidelity optical performance across both the larger FOV and frequency range of the dual passbands at two different observation bands. As briefly discussed in Section 3.3, the re-imaging lenses couple to the dual reflectors of the telescope to produce a flat, telecentric[1] beam at the focal plane and a compact aperture stop across a larger FOV. In order to see a larger FOV, the throughput[2] of the optical system is increased, requiring larger format elements. Furthermore, the POLARBEAR-2 receiver is constrained in length by the structural framework of the telescope. Achieving a higher FOV with re-imaging lenses made of polyethylene, the POLABREAR lens material, was not possible within the structural limitation. Therefore, POLARBEAR-2 and Simons Array implemented faster

---

[1] Telecentricity is a measure of the uniformity of magnification and image quality across the image plane

[2] Also called etendue

optics using polycrystalline alumina[3] Al_2O_3 lenses with their higher dielectric constant of ~ 10. Alumina lenses have the additional benefit being characterized by low loss tangent at low temperature to reduce absorptive loss and high thermal conductivity to assist in cooling to lowest possible operating temperature.

A Simons Array receiver uses three lenses: field lens, aperture lens, and collimator lens. The field lens adjusts the speed of the optics at the Gregorian focus while the aperture lens and collimator lens form an image of the primary reflector at the aperture stop and an image of the sky at the focal plane. The position in the receiver, shape, and dielectric constant are set using ZEMAX to simulate the optical system's performance. Some values and tolerances are shown in Tables 4.1, 4.2,and 4.3. We detail their fabrication, characterization, and validation process.

Lens	**Thickness (mm)**	**Surface 1**		**Surface 2**	
		Radius (mm)	**Conic**	**Radius (mm)**	**Conic**
Field	50.00	3162.52	-10.026	1366.83	-10.258
Aperture	50.00	632.33	-2.873	∞	0
Collimator	44.64	799.86	-0.3898	∞	0

Table 4.1: Surface profiles of re-imaging lenses for POLARBEAR-2b and POLARBEAR-2c. Surface 1 describes the sky-side surfaces and surface 2 describes the detector-side surfaces.

Lens	**Thickness (mm)**	**Surface 1**		**Surface 2**	
		Radius (mm)	**Conic**	**Radius (mm)**	**Conic**
Field	±0.10	±5.0	±0.5	±2.5	±0.5
Aperture	±0.25	±1.5	±0.1	-	-
Collimator	±0.25	±2.0	±0.2	-	-

Table 4.2: Tolerance of shapes of re-imaging lenses for POLARBEAR-2b and -2c

Lens	**z-position (mm)**	**xy-position (mm)**	**Tilt (°)**
Field	±1.0	±1.0	±0.50
Aperture	±2.5	±1.0	±0.20
Collimator	±10.0	±5.0	±0.25

Table 4.3: Tolerance of position and tilt of optical elements with respect to Gregorian focus

---

[3] Another name for aluminum oxide

The Simons Array alumina lenses and filters are made by CoorsTek, Inc.[4], shown in Figure 4.1 using a process which involves producing cylindrical blanks from high purity (99.5%) alumina powder and machining them to conic lens shapes. A rigorous validation process was carried out in which we measured the shape and dielectric properties of each lens and used in a Zemax simulation, led by Frederick Matsuda, containing the POLARBEAR-2 optical chain to confirm sufficient optical performance. Smaller, 51 mm witness coupons are cut from these alumina blanks prior to machining for this validation step.

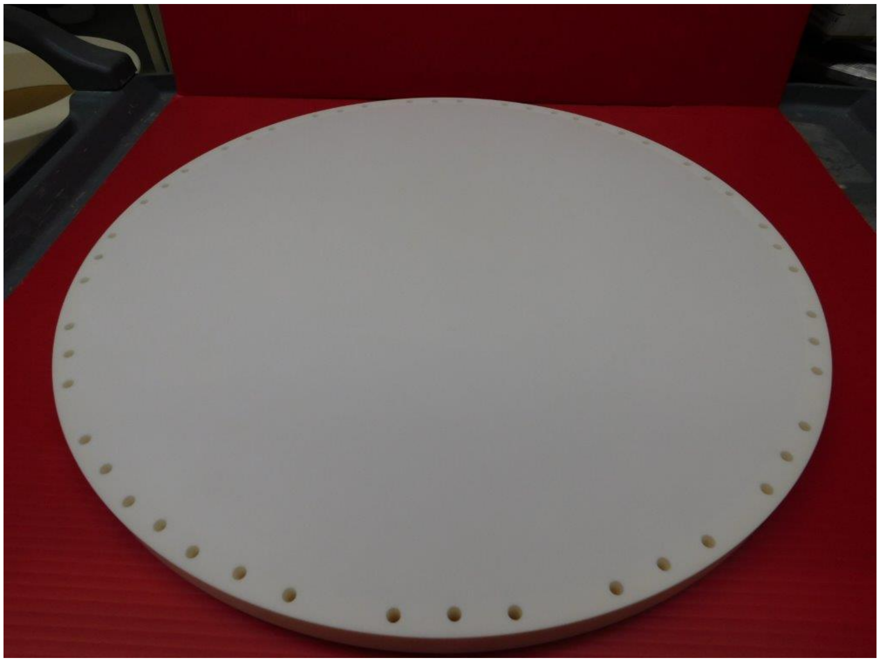

Figure 4.1: POLARBEAR-2b field lens.

Using a Michelson Fourier Transform Spectrometer (FTS) shown in Figure 4.2, the transmittance spectrum of a sample is measured to determine its dielectric properties, such as dielectric constant and loss tangent. The FTS uses the contrast between a 800 K ceramic heater behind a room temperature Eccosorb AN-72 absorber[5] aperture as a source. This source is collimated by a parabolic mirror with 150 x 150 mm cross-section and then fed to a 0.25 mm thick Mylar beam splitter with peak efficiency at 180 GHz. The fixed and moving mirrors are identical planar shapes with the same cross-section as the collimator. The beam is then focused onto a broadband detector inside a cryostat as it exits the FTS towards an ultra high molecular weight polyethylene lens. This detector is a filter-less, antenna-coupled transition-edge sensor bolometer which is read out using a superconducting quantum interference device (SQUID). This system provides sensitivity between 100 and 250 GHz with

---

[4] https://www.coorstek.com

[5] https://www.laird.com/products/microwave-absorbers/microwave-absorbing-foams/eccosorb-an

resolution set by the total travel of the FTS mirror. The sample is placed at the output of the FTS where the beam is still collimated using a holder, which has a 51 mm diameter aperture and coated with an Eccosorb absorbing screen. The transmittance spectrum of the sample is measured by dividing the spectral response of the detector with the sample (”closed”) in the optical path by the spectral response without the sample (”open”). In order to improve the signal-to-noise, we average over multiple pairs of open and closed measurements. Furthermore, to minimize the impact of gain drift on the normalization of an averaged transmission spectrum, the time ordering of an open and closed measurement is alternated from pair to pair.

Figure 4.2 shows a schematic diagram the cryogenic sample holder which cools the sample down to 100 K. This cooling system consists of a copper sample fixture which is coated with an Eccosorb absorbing screen around the sample aperture and partially immersed in liquid nitrogen. To prevent condensation on the sample, the sample fixture and liquid nitrogen can are placed in a chamber where dry nitrogen gas is continuously flown. In the cold measurement configuration, the sample holder is placed immediately after the collimating mirror due to space constraints.

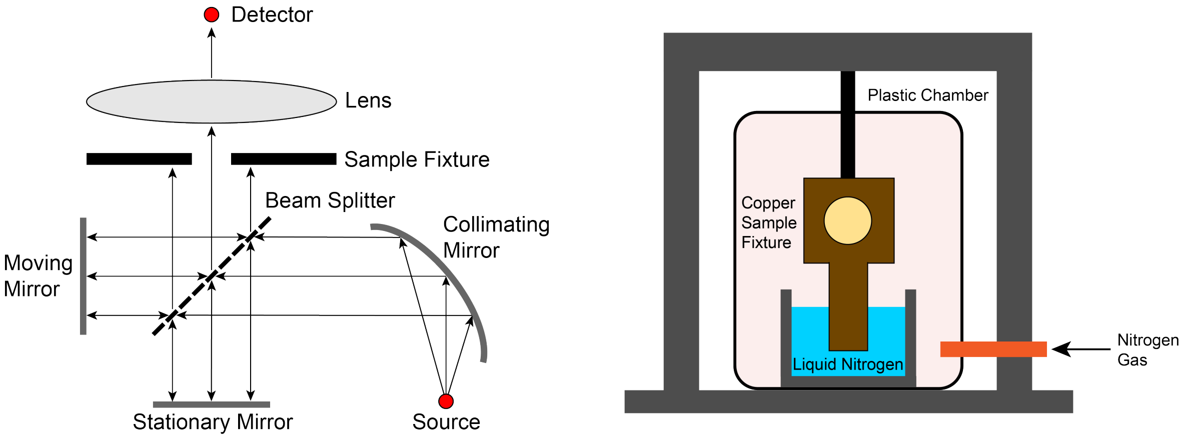

Figure 4.2: Schematics of the Michelson FTS measurement system (*left*) and of the cold sample fixture (*right*).

We report the measured dielectric properties of the POLARBEAR-2b and POLARBEAR-2c lenses in this section, as those of POLARBEAR-2a were measured by our collaborators at KEK. These lenses of both receivers were fabricated from two batches of cylindrical blanks: field and aperture lenses from Batch 1 and collimator lens from Batch 2. Figure 4.3 shows a transmittance spectrum measurement and fit of one such sample coupon.

Table 4.4 shows least squares fit values and 1-σ uncertainties of dielectric constant and loss tangent of Batch 1 and Batch 2 alumina, measured at 100 K for operational values. Ambient temperature values were first measured with results showing change in dielectric

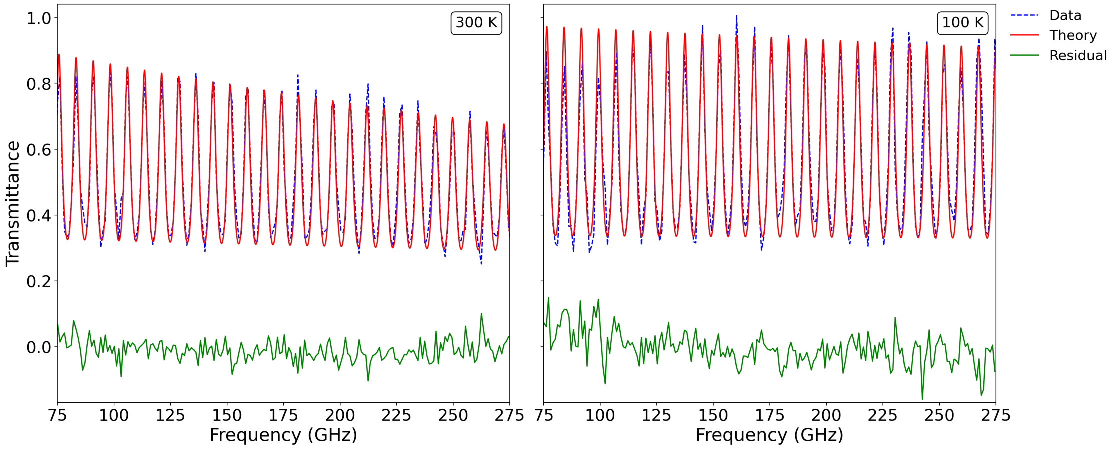

Figure 4.3: Representative FTS data (*blue*), fit (*red*), and residual (*green*) at 300 K and 100 K of a Simons Array witness coupon for dielectric characterization. The model used in this figure is described in Chapter 5.2.

Parameter	**Design**	**Batch 1**	**Batch 2**
ϵ_r	9.92	9.64 ± 0.05	9.66 ± 0.05
$\tan\delta$	$\sim 10^{-4}$	$(4 \pm 2) \times 10^{-5}$	$(8 \pm 2) \times 10^{-5}$

Table 4.4: Design and measured dielectric properties of the POLARBEAR-2b and POLARBEAR-2c re-imaging lens alumina.

constant to be within reported error bars and loss tangent reduction as expected. Based on literature values [14][52] of alumina loss tangent at 4 K, we expect a slight reduction from measured values at 100 K for operating temperatures.

Simons Array Optics Redesign

Compared to POLARBEAR, Simons Array's expansion of frequency coverage to the 95 and 280 GHz observation bands requires a complex optimization of optical performance. The lower frequency range motivates a careful re-examination of the optical clearances of each optical element to avoid strong diffraction ringing effects and spillover power. It is typical for optical clearances to be added with several cm of margin in radius between the optically viable surface and the outermost geometric ray. As seen with Equation 2.10, a Gaussian beam of lower frequency is characterized by relatively faster spreading of its opening angle. Faster spreading of the 95 GHz beam compared to the 150 GHz beam leads to relatively higher power at the edge for truncation, and thus higher spillover power and diffraction ringing as seen in Figure 2.2. The extra clearance margin for each optical element

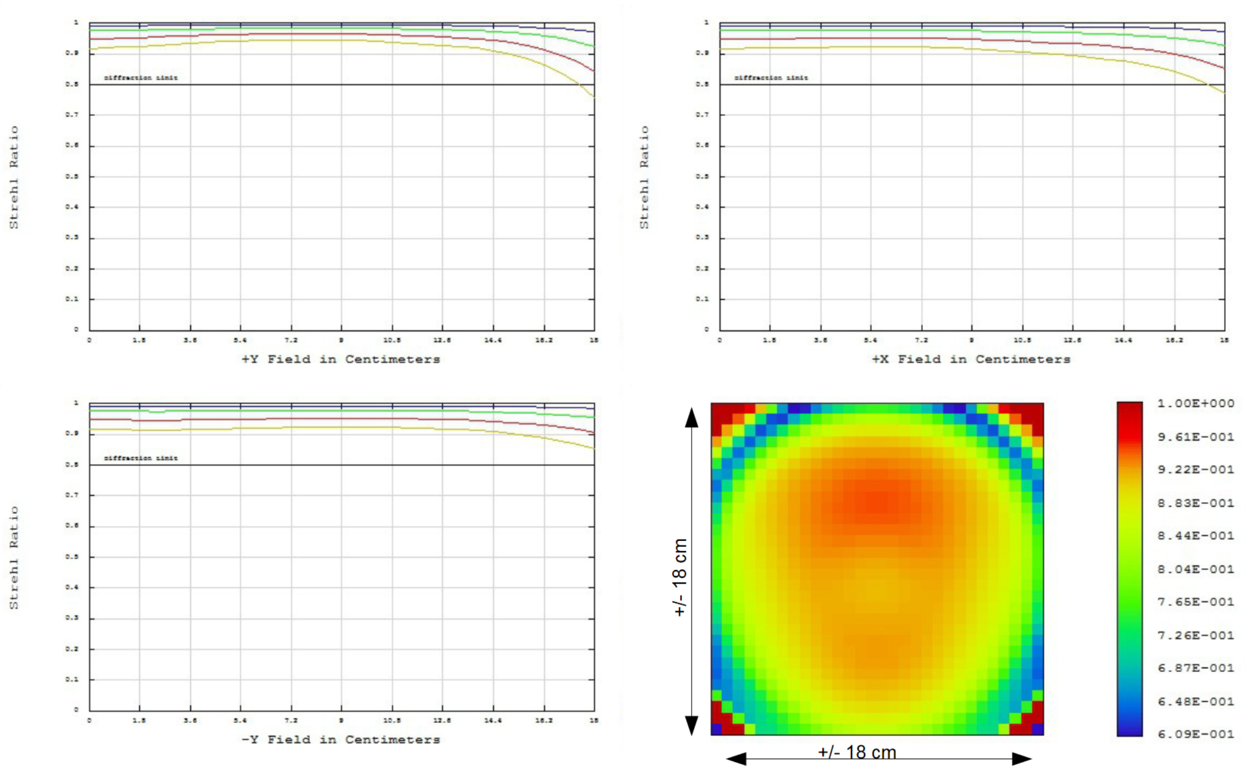

Figure 4.4: Strehl ratio as a function of focal plane position and DLFOV of of the redesigned Simons Array optical system. Strehl ratio is recovered for all but edge pixels at 280 GHz to above 0.8 [49].

is determined through physical optics simulations. The high frequency range presents a different optimization problem where the DLFOV becomes the crucial component of optical design. Strehl ratio decreases for higher frequency with all other things being equal, including constant wavefront error δ in Equation 2.11. Conceptually, this is due to the reduction in diffraction effect, as seen in the smaller beam size at higher frequency of the Airy pattern, while the effects of aberration remain unchanged. Thus Strehl ratio, the ratio of power in these two properties of the optical system, decreases. This is seen in Figure 4.4 where Strehl ratio scales in the opposite direction of frequency band.

The measured dielectric constant of re-imaging lenses of POLARBEAR-2b and -2c, $\epsilon_r = 9.64$, is lower than the original design value for POLARBEAR-2 and Simons Array, $\epsilon_r = 9.92$, leading to slower optics. This degrades the Strehl ratio at all angles and all frequencies with all else fixed. Pistoning the entire receiver away from the secondary, the simplest course of action, can recover Strehl ratio for all bands and angles, but cannot restore degradation of the image of the primary at the Lyot stop or telecentricity of the focal plane. Degradation in Lyot image results in variation of the beam shape on the sky across the FOV and nontelecentricity causes non-uniform beam truncation at the Lyot stop across the FOV. Both of these effects will cause an asymmetric beam to propagate towards the sky, resulting in a complicated relationship between the sky beam shape and focal plane position. Therefore, the shape of the collimator lens and the z-positions of individual optical elements are added as free parameters in the re-optimization problem for the optics of Simons Array. A detailed review of this process carried out by Frederick Matsuda using ZEMAX geometric ray tracing is shown in [49].

The following metrics are evaluated to assess the system's optical performance: Strehl ratio, Lyot image, primary illumination size, detector F-number, focal plane plate scale, aperture and collimator lens clearances, and receiver pistoning. The focal plane pistoning constraint is set to be $\leq$ 1 cm based on space constraints in the receiver backend. As described above, Lyot image and telecentricity have similar effects on the symmetry of the sky beam as a function of focal plane position. Primary illumination is that of the center pixel and is a proxy for sky resolution. Plate scale and detector F-number relates the angular separation on the sky to the linear separation on the focal plane, and effectively measures the angular FOV per focal plane size. The objective of this re-optimization is to preserve their fiducial design quantities.

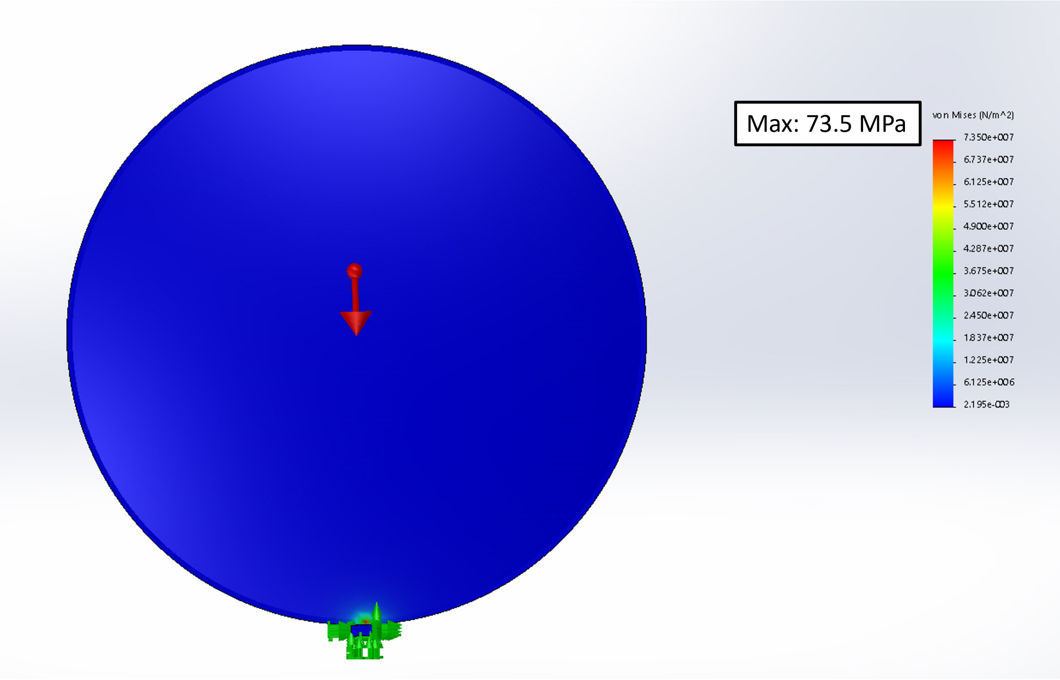

Figure 4.5: Stress study of redesigned collimator lens flange using Solidworks.

The redesigned optical system contains lens shapes listed in Table 4.1 and tolerances given by Tables 4.2 and 4.3, generated by Frederick Matsuda [49]. The DLFOV of the observation bands of POLARBEAR-2b and -2c are shown in Figure 4.4. In short summary, by pistoning the focal plane by 1.004 cm, reshaping the collimator lens to be more elliptical and ∼10% thinner, and individually pistoning the optical elements, the Strehl ratio is recovered across for focal plane for all frequency bands, including 280 GHz, while the Lyot image and telecentricity remain slightly worse than their fiducial values.

We carried out a stress study using Solidworks Simulation[6] software to ensure the thinner, 5 mm, flange of the redesigned collimator lens is not at risk of fracturing. The extreme case of the flange resting on one point was studied, as opposed to four points inside the receiver. The result of this study, shown in Figure 4.5, shows that the maximum stress from a single stress point is 73.5 MPa which results in a safety factor > 3.

Lens Fabrication

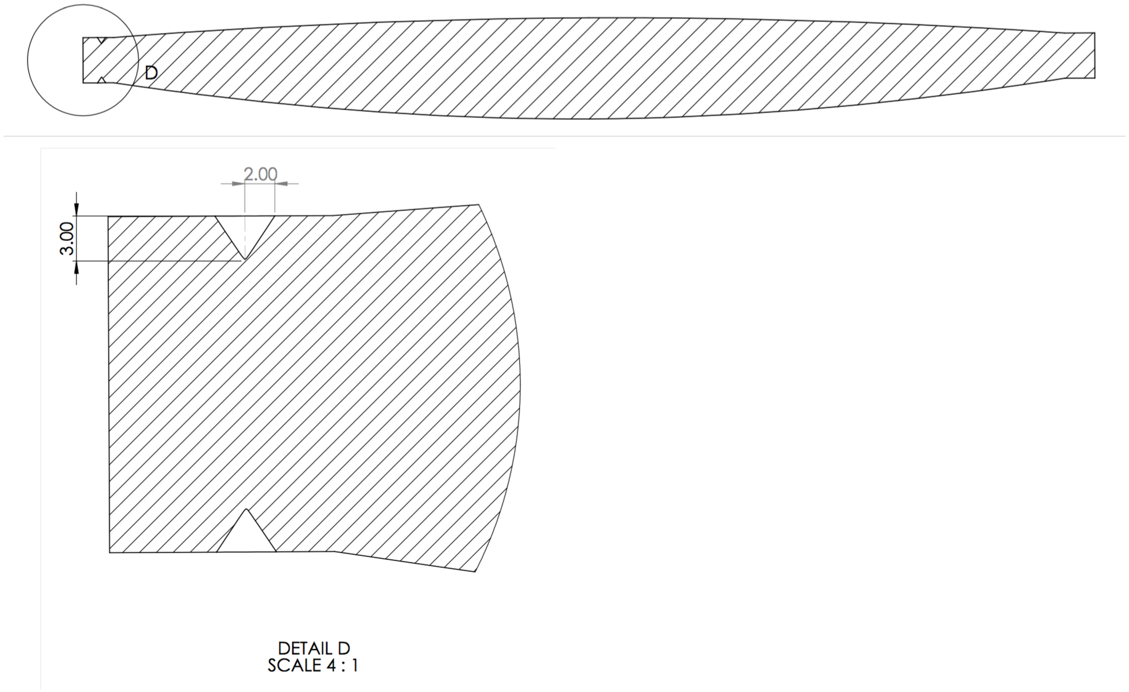

Figure 4.6: Cross section of Simons Array field lens CAD drawing, showing the precision indents designed for precision alignment of the optics.

Along with major redesign of the collimator lens, we added several features to each lens to assist the alignment process, guided by the positional tolerances shown in Table 4.3. These modifications include three precision divots per surface, shown in Figure 4.6, which define both the plane of reference for axial positioning and a circle whose center defines a point

---

[6] https://www.solidworks.com

of reference for lateral positioning. Additionally, precision through holes were added on the flange for repeatable alignment to the optics tube lens fixture. The alignment process, using these features, are discussed in more detail in Chapter 4.2.

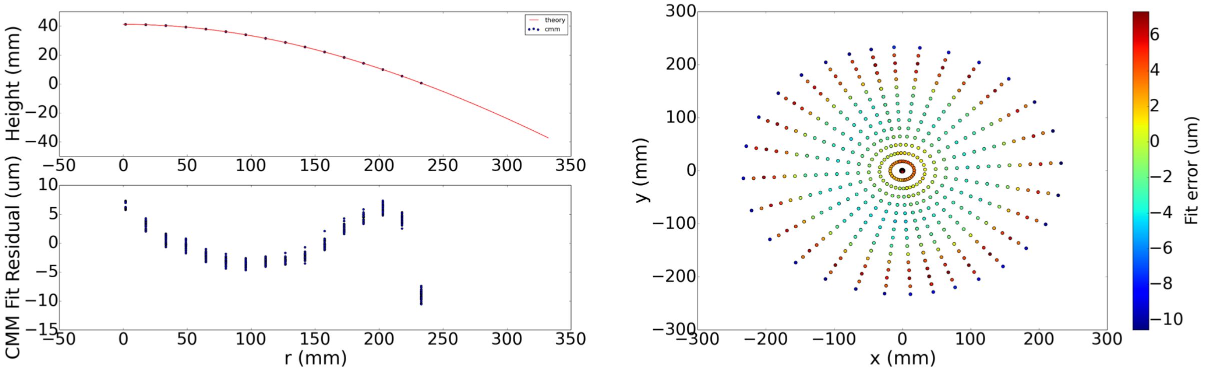

Figure 4.7: Representative least square fit and residuals to aspheric surface profile of a Simons Array lens.

Lens	Radius of curvature (mm)	Conic constant
Field (sky)	3132.7±2.9	-13.57±0.74
Field (detector)	1369.9±0.6	-10.32±0.01
Aperture	633.7±0.3	-2.90±0.02
Collimator	801.8±0.6	-0.38±0.03

Table 4.5: Measured radius of curvature and conic constant of each aspheric lens surface for POLARBEAR-2b.

Lens	Radius of curvature (mm)	Conic constant
Field (sky)	3157.4±2.3	-8.23±0.57
Field (detector)	1364.3±0.5	-10.89±0.01
Aperture	633.4±0.3	-2.91±0.01
Collimator	801.9±0.6	-0.38±0.04

Table 4.6: Measured radius of curvature and conic constant of each aspheric lens surface for POLARBEAR-2c.

The machined lens surfaces are measured on a coordinate-measuring machine (CMM) with attention given to thickness and shape. The CMM data is used for least square fitting to an aspheric surface profile, following Equation 4.1

$$z\left(r\right)=\frac{r^2}{R\left(1+\sqrt{1-\left(1+\kappa\right)\frac{r^2}{R^2}}\right)} \tag{4.1}$$

where $z(r)$ is the height with respect to the zenith of the surface profile, R is the radius of curvature, r is the radius in the cylindrical coordinate system, and κ is the conic constant. All thicknesses and flatness were measured to be within 25 μm of the specified quantity. Figure 4.7 shows a representative fit of a Simons Array lens. Tables 4.5 and 4.6 show the results of fitting with 1-σ uncertainties. While the shallow curvature, sky-side surfaces of both field lenses were out of tolerance, additional ZEMAX studies were carried out with measured lens shapes to ensure that only the pixels above the ±2° FOV along the X-axis were at risk of falling below Strehl ratio of 0.8 for 280 GHz and were sufficient for operation.

Lyot Stop

POLARBEAR-2a uses a Lyot stop made of a custom blackbody material called the KEK black, which is comprised of Stycast 1090, Catalyst 9, Carbon black, and plastic beads. This material is also used as the blackbody absorber of stray millimeter-wave light in the inner-wall of the 4 K optics tube. Based on KEK black's relatively poor absorptance in comparison with other commercial options such as TK THz RAM and Eccosorb HR-series and poor thermal conductance, we made design changes from that of POLARBEAR-2a to that which utilizes materials with higher millimeter-wave absorption and thermal conductivity. Figure 4.8 shows an image of the CAD cross-section and the redesigned Lyot stop, made of an aluminum 1100 knife-edge with Eccosorb HR-10 coating. With the Lyot

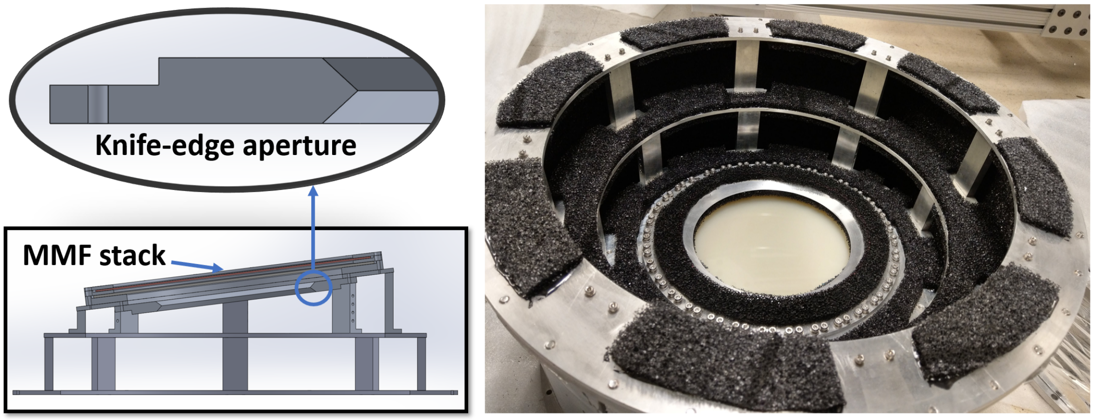

Figure 4.8: CAD cross-section of the knife edge apeture and Lyot stop tower (*left*) and picture of an assembled POLARBEAR-2b Lyot tower (*right*).

being the largest power emitter among the cold optical components of POLARBEAR-2a due to its relatively high temperature and intentional beam truncation [40], aluminum 1100 replaces KEK black as the bulk material of the Lyot for its high thermal conductivity. Eccosorb HR-10 is epoxied on both sides of the taper for beam truncation and the knife-edge is angled such that reflections are not seen by the detectors.

Receiver Window

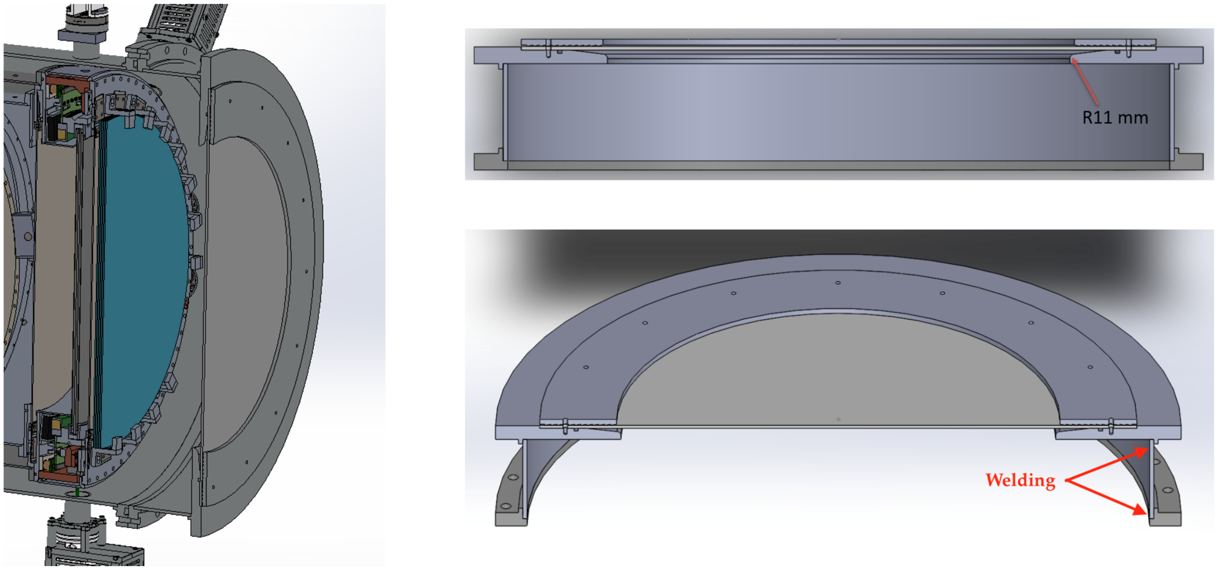

Figure 4.9: CAD cross-sections of the POLARBEAR-2c window and vacuum fixture.

POLARBEAR-2b utilizes an identical Zotefoam vacuum window design as POLARBEAR-2a. We designed a thin UHMWPE window and vacuum fixture for POLARBEAR-2c, seen in Figure 4.9, based on the work of the SPIDER window [51] due to the high level of measured loss at 220 and 280 GHz of Zotefoam. This is expected to be sourced by scattering with its large pore size relative to 1 mm photons. The thickness of the UHMWPE window is determined using a combination of Solidworks simulations and experimental stress tests for robustness against mechanical failure. An excessively thick window, while beneficial for mechanical robustness, would unnecessarily contribute to ambient temperature emissive loading on the detectors. The minimum thickness of 4 mm for a mechanically robust vacuum window, to be shown in this section, with an optimal AR coating contributes to 0.27, 0.43, 0.63, and 0.76% absorption loss and 0.76, 1.2, 1.8, and 2.2 K in-band loading for 95, 150, 220, and 280 GHz bands, respectively. Even for this minimum thickness, in-band loading is significant, in particular for the POLARBEAR-2c bands. The new vacuum fixture is designed to redistribute force from the edge of the aperture to a larger area which expands radially outward, whose cross-section is shown in Figure 4.9. A fixture clamp with serrated, concentric grooves sinks into the window to prevent vacuum failure from the slow creep of UHMWPE's fixture clearance holes into the O-ring surface.

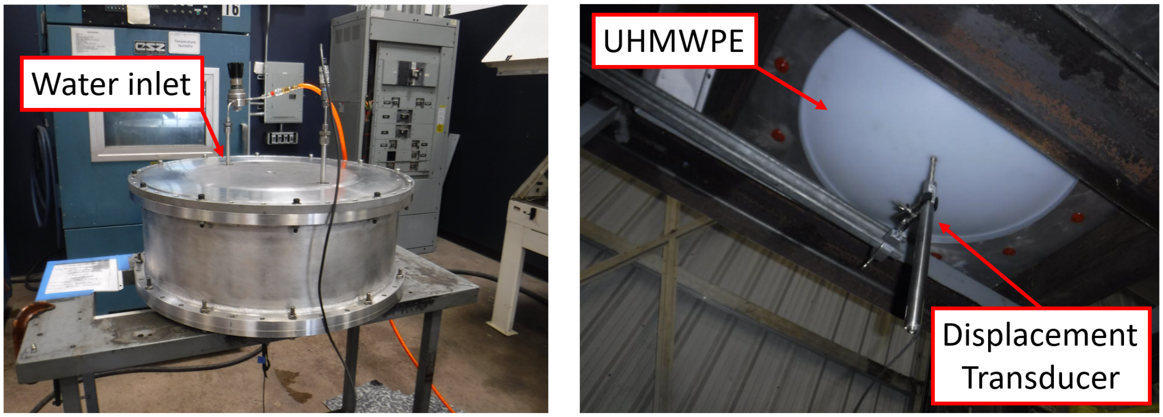

Figure 4.10: Pressure vessel of window test and displacement done at NTS, Inc.[7]

Window stress experiments are carried out on a 4 mm thick UHMWPE plate on the POLARBEAR-2a fixture to produce harsher test conditions. The POLARBEAR-2a window fixture, designed to hold the 200 mm thick Zotefoam window, has a 4 mm radius chamfered aperture without a taper, compared to the 11 mm radius chamfered aperture with a taper of the new fixture. A requirement of safety factor, defined as the ratio of yield strength to operating pressure, is set at $\gtrsim 2$ for these stringent stress tests. Figure 4.10 shows the pressure vessel in which these tests were carried out. Rather than vacuum pumping on the window and fixture assembly, we turned the assembly upside down and pumped water into the vessel. This allows uniform pressure exceeding 1 atm to be applied on the top of the UHMWPE plate. An electronic drop indicator is placed above the plate to measure its displacement at applied pressures and ensure against contact between the ambient temperature window and RTMLI at operating pressures.

Figure 4.11 shows the pressures applied on the UHMWPE and the respective displacement. 1.0, 1.1, and 1.3 atm were applied for 24, 48, and 48 hours, respectively, without signs of damage nor leakage. Displacement of 48 mm was recorded for 1.3 atm, which ensures against contact with RTMLI. Given the UHMWPE was robust against ×2.6 higher pressure than operating value on the sharper POLARBEAR-2a aperture, this test was considered a successful mechanical validation of the 4 mm thick window.

Figure 4.12 shows the stress analysis with 0.5 and 1.3 atm of pressure, used to estimate a conservative safety factor. While the plate withstood 1.3 atm of pressure in empirical testing, the maximum stress experienced by the plate at this pressure is used to calculate the lower

---

[7] https://nts.com

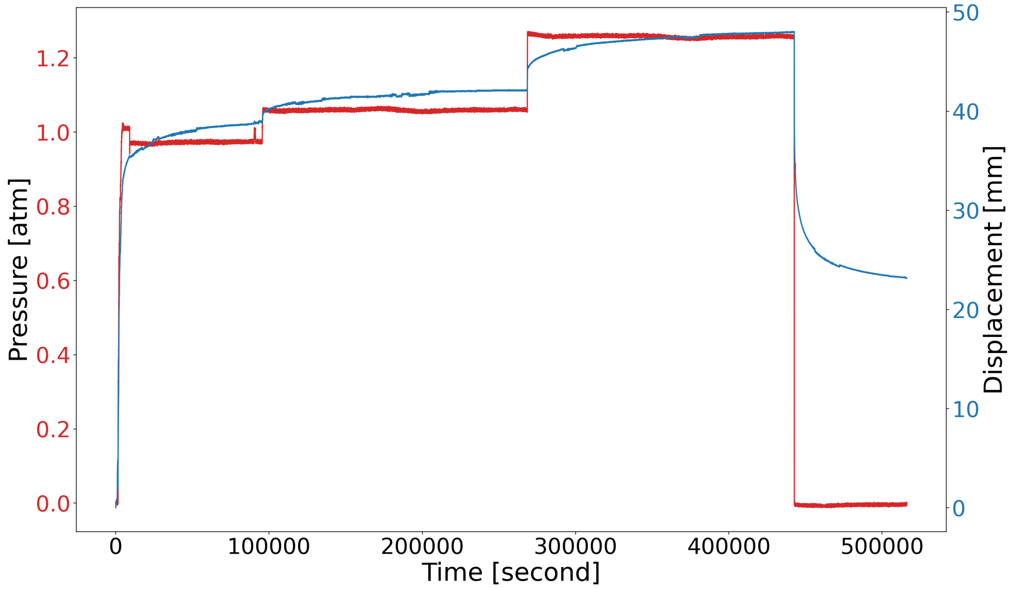

Figure 4.11: Measured pressure (*red*) and window displacement (*blue*) vs time curve.

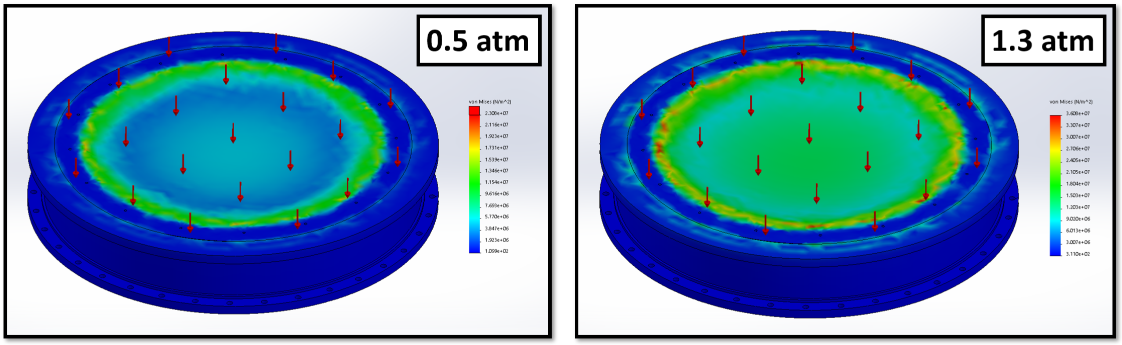

Figure 4.12: Solidworks simulation of 0.5 atm (*left*) and 1.3 atm (*right*) applied to a 4 mm UHMWPE window on the POLARBEAR-2c window vacuum fixture. Maximum values of pressure experienced by the window are 11 and 33 MPa at the aperture for 0.5 and 1.3 atm, respectively. These values are used to calculate a conservative lower limit of the safety factor > 3.

bound in safety factor[8]. This stress simulation shows a maximum pressure of 11 and 33 MPa at the edge of the aperture for 0.5 and 1.3 atm, respectively. Thus, the 4 mm UHMWPE

---

[8] A reliable literature value of yield strength of UHMWPE could not be found

used for the Simons Array window is characterized by safety factor > 3. UHMWPE window is AR coated with a single layer of PTFE foam and is extensively detailed in Chapter 5.7.

4.2 Alignment Procedure of Optical Elements

Position alignment of optical elements is a crucial for maintaining expected optical performance, motivating tolerance analysis whose calculated requirements are shown in Table 4.3. The Strehl ratio is calculated with a Monte Carlo simulation based on normal distribution variance around optimal positions to produce the required accuracy in aligning the optical elements with respect to the focal plane during assembly. The definitions for alignment, tilt, xy-plane, and z-axis are shown in Figure 4.13. We describe the optical alignment scheme which we designed and used for lab and site commissioning of the Simons Array receivers.

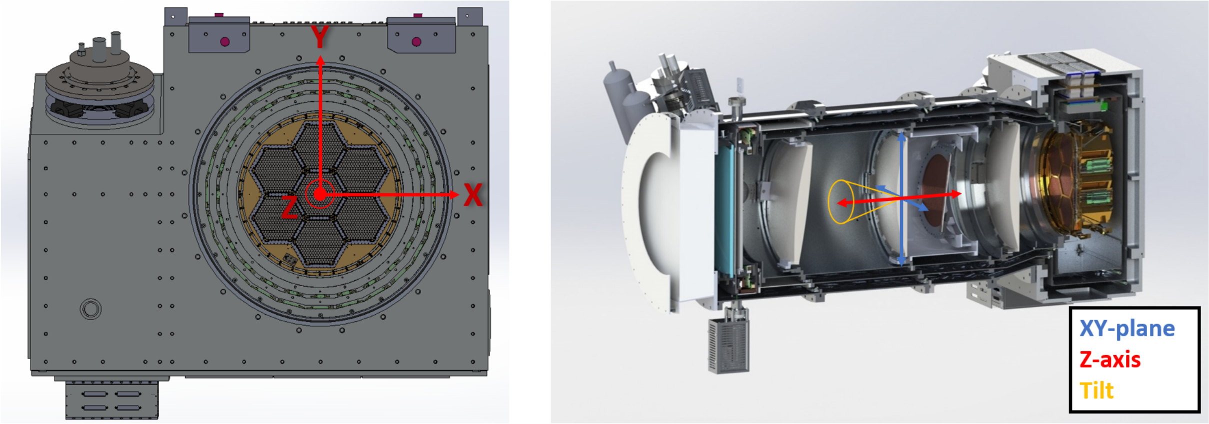

Figure 4.13: Lateral (xy-plane), axial (z-axis), and tilt coordinate systems referenced in Table 4.3.

A Microscribe MX portable CMM is used to measure and align the re-imaging lenses and Lyot with respect to the focal plane. Figure 4.14 shows the picture of the CMM and Table 4.7 shows its specifications. Its light weight, designed for portability, allows ease of

Parameter	**Specification**
Weight	12 lb
Accuracy	$\pm 50\ \mu$m
Reach	635 mm

Table 4.7: Microscribe MX specifications

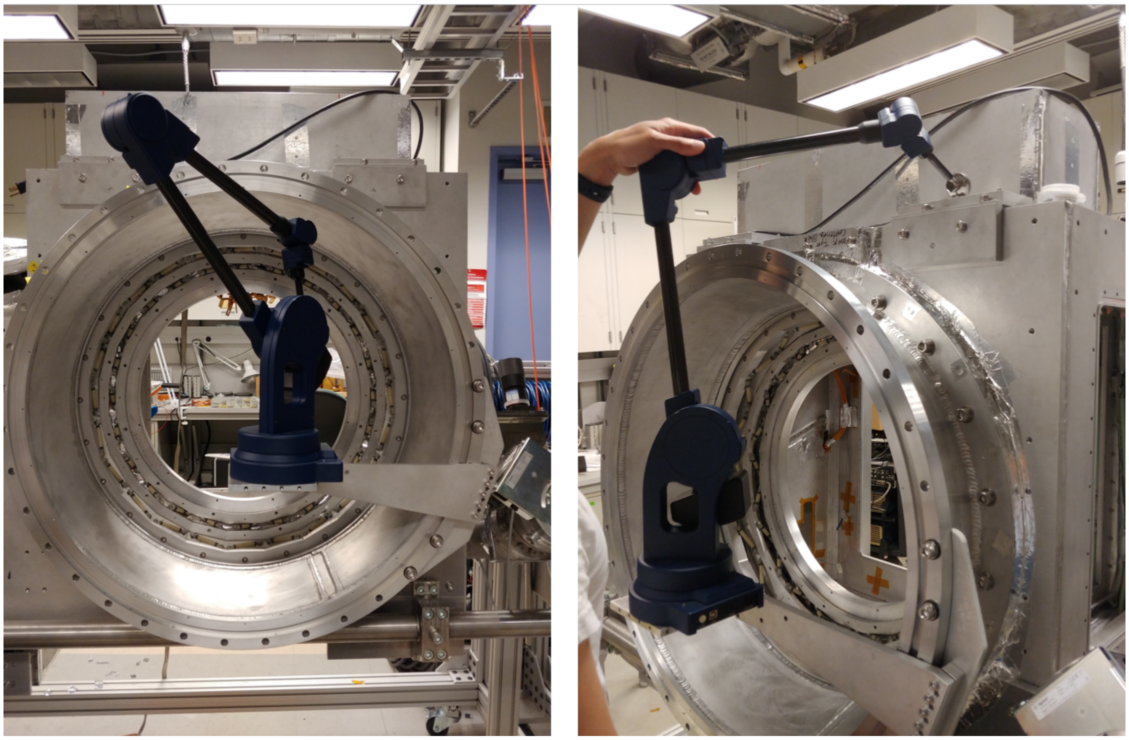

Figure 4.14: Pictures of the CMM alignment tool in action, measuring the 300 K tapered optics tube shell (*left*) and the backend photogrammetry target ((*right*)). Photo courtesy of Jennifer Ito.

use at the site and at different segments of the optics tube where it is mounted at different heights throughout the assembly without fear of safety to personnel or the receiver. Accuracy of ±50 μm is sufficient to meet a ±1 mm minimum uncertainty in optical element positions. Its working diameter is large enough for the longest travel required within the optics tube.

The lateral xy-position and tilt of the lenses and Lyot are extrapolated in this procedure by using the CMM to measure metrology targets on circular components of the backend, optics tube shells, and optical elements. A fitting code, written by Calvin Tsai[9], is then used to fit a 2D circle to a 3D point cloud of CMM measurements, whose geometric center is defined as the lateral xy-position of the element. Figure 4.6 shows the indents at 0°, 120°, and 240° of a lens flange, used to define a circle whose origin is taken as its xy-position. These indents are designed and machined with high precision for alignment. Lens lateral positions are measured with respect to the sky-side flange of its corresponding optics tube 300 K vacuum shell. The aperture lens and field lens lateral positions can be corrected on the spot by adjusting the alignment screws, shown in Figure 4.15, made of insulating G10 fiberglass.

---

[9] The code was further refined for deployment by Bryce Bixler, Jennifer Ito, and the author for site commissioning

These screws are tightened into the 4 K shell, pointing radially out to make contact against the 50 K shell to minimize thermal conduction between the 4 K and 50 K radiative shields. Three screws are located at 0°, 120°, and 240° to allow the necessary degrees of freedom for complete xy-positioning control of the lens and 4 K shell positions and aid in supporting the weight of the 4 K shells.

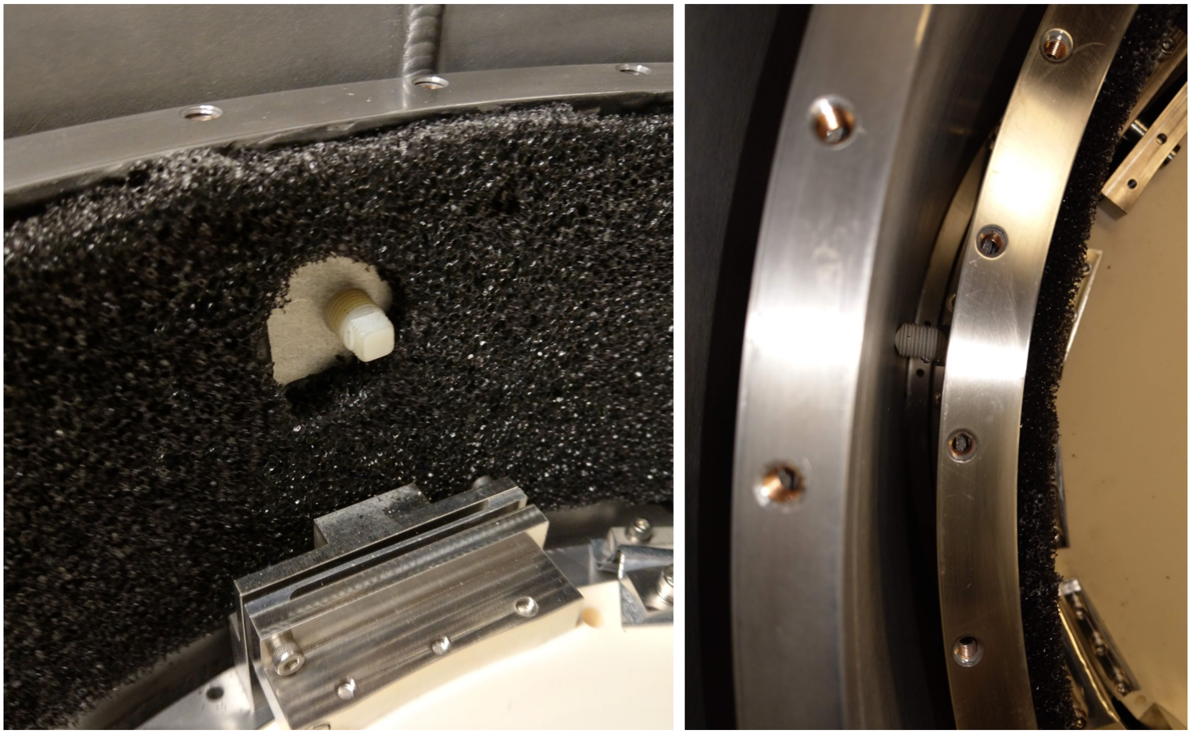

Figure 4.15: Photos of the G10 screws for alignment from the inside of the 4 K optics tube shell (*left*) and pushing on the 50 K optics tube shell for lateral alignment (*right*).

Optical z-axis of all optical elements, Lyot lateral, collimator lens lateral, and field lens tilt alignments are not adjustable and mounting parts must be machined to correct dimensions to meet specified tolerance. z-axis alignment is met by machining mounting parts with temperature-dependent coefficient of thermal expansion taken into account for all optics tube parts. Lyot and collimator lens lateral alignment is measured with the CMM during one iteration of assembly and mounting parts are altered according to measured deviation from fiducial values. With the Lyot assembled within the Lyot shell, the Lyot lateral position is calculated by measuring its outer-diameter and its concentricity with respect to the 4 K Lyot shell sky-side flange. The Lyot shell sky-side flange can be measured with respect to the 4 K aperture shell to further ensure concentricity to the greater optics tube assembly. The collimator lens lateral position is measured by measuring its flange concentricity with respect to the 300 K tapered shell sky-side flange. The field lens tilt is calculated by measuring the angle between the 2D planes of the flange and its mounting ring, as shown in Figure 4.16.

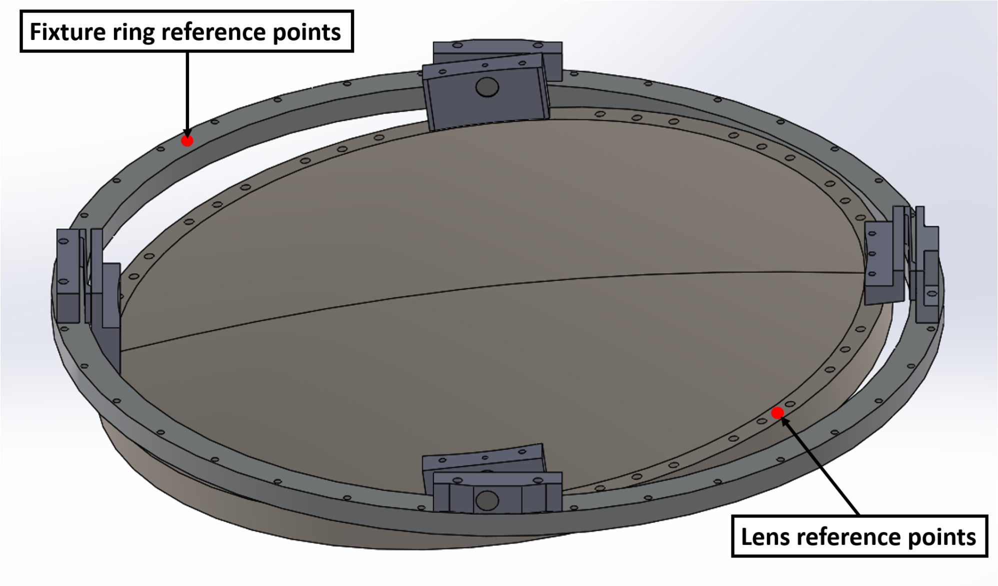

Figure 4.16: CAD image of the field lens and its fixture ring, showing in *red* the reference points to measure with the CMM for measurement of tilt.

As the optics tube is assembled beyond the collimator lens, active lens alignment procedure occurs using CMM measurements and the G10 screws. Initially, the CMM measures inner-diameter of the vacuum O-ring groove on the 300 K tapered shell and the photogrammetry targets on the backend. Knowing the focal plane position with respect to these targets, this initial measurement can be used as reference for subsequent optics tube lateral measurements. The aperture lens, upon assembling up to the 300 K aperture shell is aligned. The CMM measures its flange indents and then the inner-diameter of vacuum O-ring groove on the 300 K shell, as shown in Figure 4.17. The G10 screws are adjusted to align their geometric centers. An identical process is used for the field lens. Figure 4.18 shows one such alignment data for POLARBEAR-2b commissioning.

4.3 Optics Tube Cryogenics

The POLARBEAR-2b and POLARBEAR-2c optics tubes were cryogenically validated separately from their backend counterparts and then cryogenically validated as an integrated system. As a part of the validation process, we made design improvements at CAD level, worked with several machine shops to produce the optics tube parts, verified the 300 K vacuum shell to hold $<10^{-5}$ torr for sufficiently long times, performed iterative series of thermal cycles towards required operating temperatures, integrated with the independently validated half wave plate system, and full integrated the receiver system. This section details

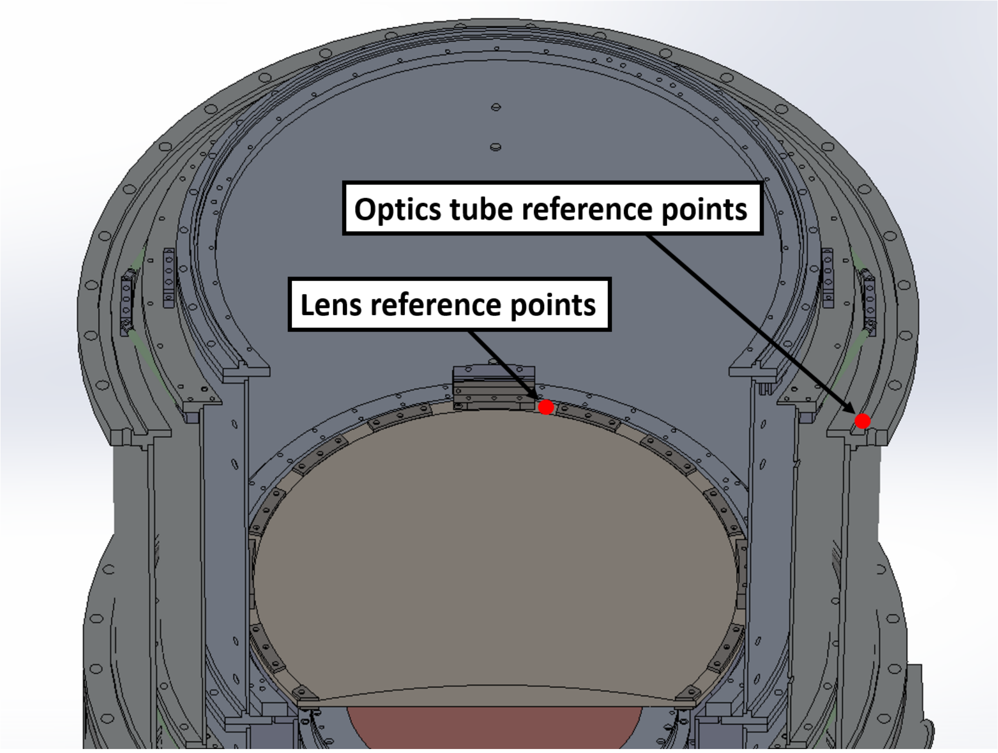

Figure 4.17: CAD cross-section image of the aperture lens within the optics tube, showing in *red* the reference points to measure with the CMM for calculation of concentricity and lateral xy-position.

design changes to the optics and cryogenic system, filtering schematic based on thermal modeling, and summary of the cooldowns of each optics tube.

Radiative Thermal Modeling

We model the radiative loads on the mK stages from the optics tube and backend shield. This calculation is motivated by the optical filtering scheme of the receiver and the budgeting of thermal loads based on the intercooler (IC) and ultra-cold (UC) fridge hold time requirements. In particular for POLARBEAR-2c, its expansion to higher frequency contributes to higher energy photons on the mK stages. Tables 4.8 and 4.9 shows the radiation load budget based on expected contributions to the mK stages from thermally conductive sources.

This problem is separated into two parts: radiation from the front and from the back of the focal plane. The front of the focal plane receives radiation from a complex chain of optical elements and blackbody-coated optics tube 4 K shell which is modeled using temperature-dependent emissivity values and measured transmission spectra. The back of the focal plane receives radiation from the backend 4 K shield through multiple reflections whose complexity

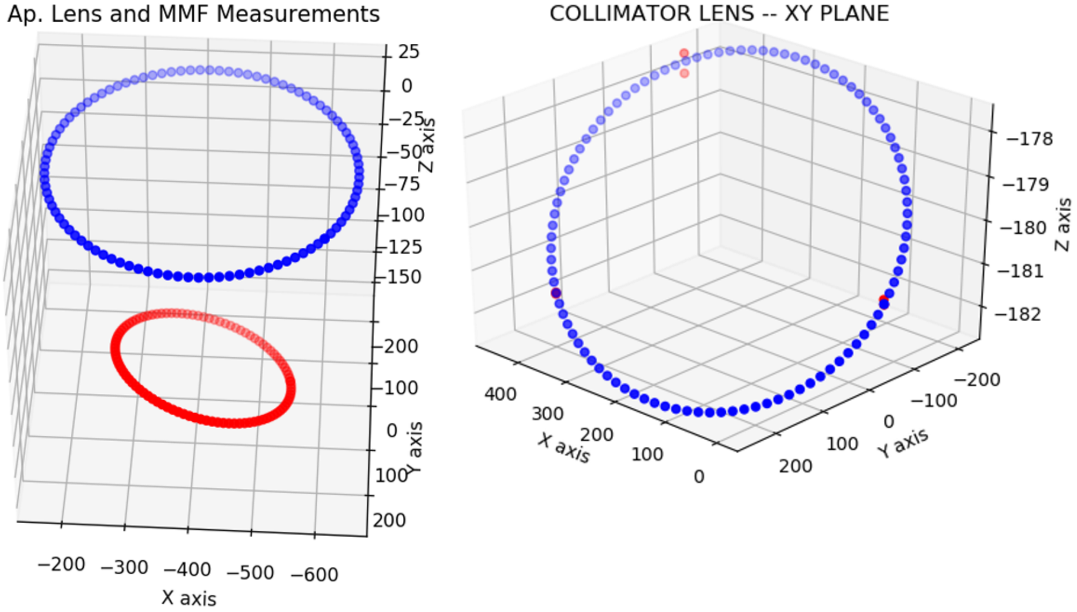

Figure 4.18: Optics tube alignment CMM data, courtesy of Calvin Tsai.

Stage	**Tower legs**		**Striplines**		**RF shield**		**Total budget**	**Radiation budget**	
	Min	Max	Min	Max	Min	Max		Min	Max
IC	0.8	1.4	1.2	2.2	0.7	1.4	18.0	13.0	15.3
UC	0.20	0.35	0.10	0.15	0.05	0.10	4.0	3.4	3.65

Table 4.8: Radiation budget for POLARBEAR-2b. All values are listed in units of μW. Minimum and maximum budget values are given due to uncertainties in the calculated conductive heat loads. Total budget is drawn from a sorption fridge requirement of 72 hours of hold time. Minimum values are used for a conservative assessment of the radiation loading requirement and maximum values are listed for reference.

is reduced to a thermal circuit model. The following assumptions are made in this model:

- Beam opening angle of 15° with Lambert's Law taken into account for angles away from zenith.
- Blackbody absorber temperature of 6 K on the 4K optics tube shell wall as a conservative assumption. Blackbody absorber temperature had been measured to be T = 5.4 K for POLARBEAR-2a KEK black.
- Circular focal plane diameter of 365 mm

Stage	**Tower legs**		**Striplines**		**RF shield**		**Total budget**	**Radiation budget**	
	Min	Max	Min	Max	Min	Max		Min	Max
IC	0.8	1.4	1.2	2.2	0.7	1.4	20.0	15.0	17.3
UC	0.20	0.35	0.10	0.15	0.05	0.10	5.0	4.4	4.65

Table 4.9: Radiation budget for POLARBEAR-2c. All values are listed in units of μW. Minimum and maximum budget values are given due to uncertainties in the calculated conductive heat loads. Total budget is drawn from a sorption fridge requirement of 72 hours of hold time. Minimum values are used for a conservative assessment of the radiation loading requirement and maximum values are listed for reference.

- Optical elements considered to be uniform temperature of measured center temperatures from POLARBEAR-2a comissioning runs. Temperature is highest at the center of optical elements as heat is drawn from the flange and edge, thus this is a conservative assumption.
- Optical elements have uniform transmittance and emissivity across optical areas based on measurements.
- Focal plane emissivity of 1.0 as a conservative assumption.
- Backend 4K shell emissivity of 0.1 as a conservative assumption since reflective mylar tape covers the backend 4 K shell's inner wall.
- Neglect stray light.
- Neglect HWP.

The front of the focal plane receives radiation from 2π steradian with the majority of the contribution coming from the 6 K blackbody. From the 15° opening angle, it sees power from the sky and optical elements, with significant power emitted from the ambient temperature window which is transmitted, filtered, and re-emitted at each element according to,

$$\begin{aligned} \int \varepsilon(\nu)P(\nu)d\nu =& \varepsilon_{300\mathrm{K}}\int_{300\mathrm{K}} P(\nu)d\nu + \varepsilon_{50\mathrm{K}}\int_{50\mathrm{K}} P(\nu)d\nu + \\ & \varepsilon_{4\mathrm{K}}\int_{4\mathrm{K}} P(\nu)d\nu + \varepsilon_{350\mathrm{mK}}\int_{350\mathrm{mK}} P(\nu)d\nu \end{aligned} \tag{4.2}$$

where

$$P(\nu) = \frac{2h\nu^3}{c^2}\frac{1}{e^{h\nu/k_BT}-1} \tag{4.3}$$

is the Planck's law spectral density. In Equation 4.2, we assume emissivity values are constant and taken at peak frequency of the spectrum for each temperature stage, as listed in Tables 4.10 and 4.11. The transmittance spectrum of each optical element is drawn from measured values up to 5 THz. For data not available, we assume best guess values.

Optical element	**Stage (K)**	**T (K)**	**Size (mm)**	**Emissivity**			
				300K	50K	4K	350mK
Window	300	230	490	0.9	0.4	0.05	0.01
RTMLI	300	170	500	0.9	0.4	0.05	0.01
IR filter	50	55	440	-	0.9	0.05	0.01
F. lens	4	5	500	-	-	0.1	0.1
A. lens	4	5	500	-	-	0.1	0.1
MMF 1	4	4	300	-	-	0.01	0.01
MMF 2	4	4	300	-	-	0.01	0.01
C. lens	4	5	530	-	-	0.1	0.1
MMF 3	0.35	0.5	365	-	-	-	0.01

Table 4.10: Input parameters of POLARBEAR-2b elements for thermal model.

Optical element	**Stage (K)**	**T (K)**	**Size (mm)**	**Emissivity**			
				300K	50K	4K	350mK
Window	300	290	510	0.9	0.4	0.05	0.01
RTMLI	300	170	500	0.9	0.4	0.05	0.01
IR filter	50	55	440	-	0.9	0.05	0.01
F. lens	4	5	500	-	-	0.1	0.1
A. lens	4	5	500	-	-	0.1	0.1
MMF 1	4	4	300	-	-	0.01	0.01
MMF 2	4	4	300	-	-	0.01	0.01
C. lens	4	5	530	-	-	0.1	0.1
MMF 3	0.35	0.5	365	-	-	-	0.01

Table 4.11: Input parameters of POLARBEAR-2c elements for thermal model.

The back of the focal plane receives radiation from the aluminum 4 K backend shield through multiple reflections which increases the effective emissivity beyond that of aluminum. We model this problem as a heat exchange circuit, as shown as a diagram in Figure 4.19, where $E_1 - E_2$ is the driving radiation power between the two surfaces, R_{1s} is the resistance of the focal plane surface, R_{2s} is the resistance of the backend shield surface, and R_{12} is the resistance of the free space between them. The last term requires the utilization of view factor which is a geometric quantity related to the fraction of radiation leaving surface 1 and enclosed by surface 2. When surface 1 is completely enclosed by surface 2, the view factor

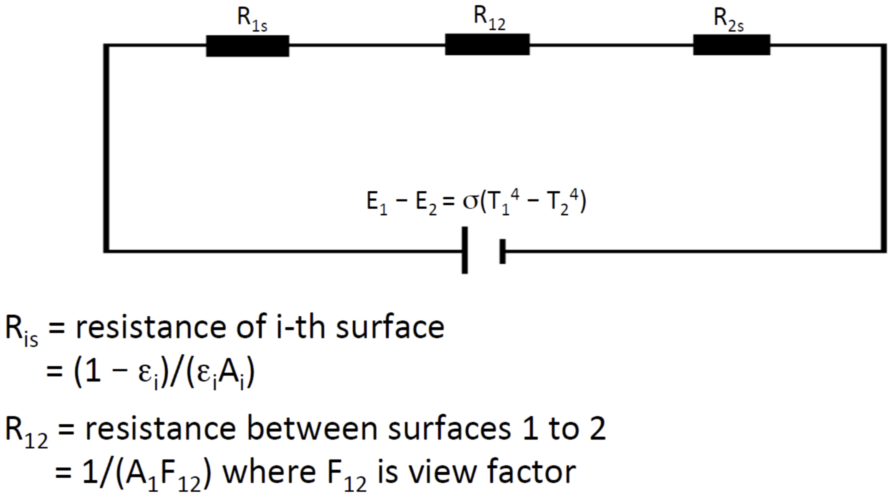

Figure 4.19: Schematic diagram of heat exchange circuit between back of focal plane and backend 4K shield.

is $F_{12} = 1$, which we make as a conservative assumption for this problem. It follows that,

$$\begin{aligned} Q_{12} &= -\varepsilon_{\text{eff}} \sigma A_1 T_2^4 \\ &= \frac{E_1 - E_2}{R_{1s} + R_{12} + R_{2s}}, \end{aligned} \tag{4.4}$$

and for the limit $T_1 \ll T_2$,

$$\varepsilon_{\text{eff}} = \left(\frac{1}{\varepsilon_1} + \frac{A_1}{A_2} \left(\frac{1}{\varepsilon_2} - 1 \right) \right)^{-1}. \tag{4.5}$$

Receiver	**RTMLI layers**	**MMF configuration**	**IC**	**UC**
POLARBEAR-2b	6	12 icm 8.7 icm 6.3 icm	7.5 μW	2.1 μW
POLARBEAR-2c	9	14 icm 12 icm 10.7 icm	7.7 μW	3.7 μW

Table 4.12: Expected radiative loading on IC and UC mK stages for POLARBEAR-2b and POLARBEAR-2c.

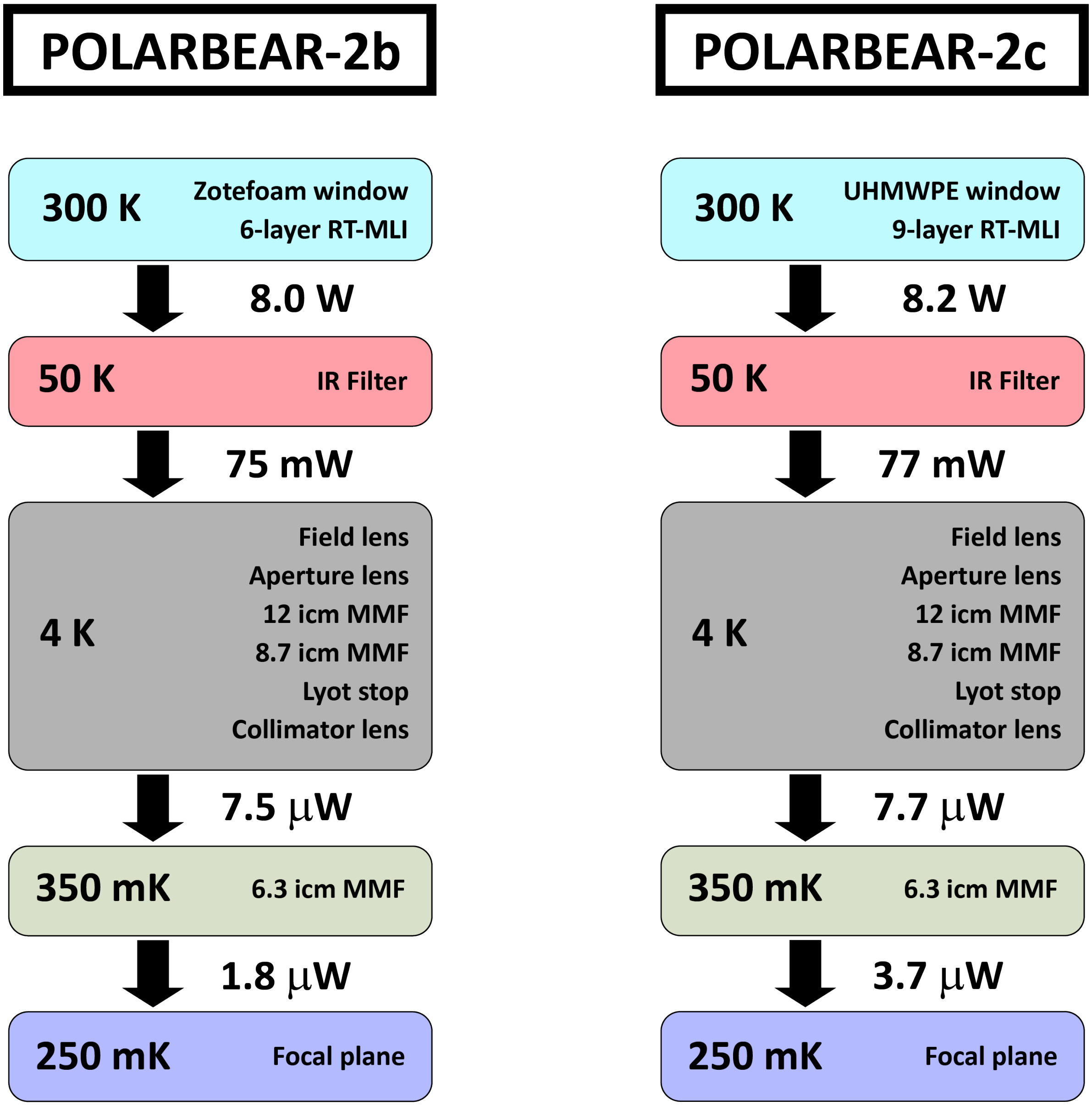

Figure 4.20: Diagram of radiation loading through multiple temperature stages of POLARBEAR-2b and POLARBEAR-2c.

For the case $A_1 = 0.41\mathrm{m}^2$, $A_1 = 1.7\mathrm{m}^2$, then $\varepsilon_{\mathrm{eff}} = 0.32$ and the radiation loading to the back of the focal plane is 0.45 μW. Adding this contribution to the UC stage, we summarize our calculation of the radiation loading in Table 4.12 and Figure 4.20. These expected values are well below the minimum expected values listed in Tables 4.8 and 4.9. As a result of this study for POLARBEAR-2c, the number of RTMLI filters is increased to accommodate a hotter, 300 K, UHMWPE window and the MMF low-pass filters are chosen with higher cutoff frequencies for the higher frequency in-band photons.

Cooldown Validation Tests

Run Number	Objectives
1	First assembly with only optics tube shells.
2	50 K sky-side blank-off incorporated and heaters introduced on heat links.
3	Debugging low conductance of 50 K heat link with new design.
4	More 6N aluminum added to 50 K heat link, MLI applied on more bare aluminum surfaces, and Apiezon N grease introduced on optics tube shell adjoining surfaces.
5	Lenses and helicoils on all adjoining surfaces incorporated.
6	Repeat of Run 5 with more robust application of MLI on blank-off surfaces.
7	Alumina IR filter, aperture tube with Lyot tower, Eccosorb blackbody absorber, and 6N aluminum heat links along optics tube shell clamping interfaces incorporated. Increased clamping surface area for 4 K heat link onto optics tube shell. Increased number of 6N aluminum to 50 K heat link. Validation complete.
8	HWP system with mock mass tester integrated.

Table 4.13: Cooldown runs and objectives of POLARBEAR-2b

Run Number	Objectives
1	First assembly with only optics tube shells.
2	All optical elements minus IR filter and optical window, incorporated. Blank-offs used with blackened surfaces i lieu of filter and window.
3	Repeat of Run 2 due to unmounted thermometers.

Table 4.14: Cooldown runs and objectives of POLARBEAR-2c

The optics tube parts of POLARBEAR-2b and POLARBEAR-2c were machined at the UC San Diego, Scripps Institute of Oceanography R&D Machine Shop[10] and UC Berkeley, Department of Physics R&D Machine Shop[11]. Several quality of life changes were implemented at the design level, such as adding a detachment feature to the PTC section of the

---

[10] https://scripps.ucsd.edu/mpl/facilities/rd-machine-shop

[11] https://physics.berkeley.edu/resources/technical-services/machine-shop

vacuum shell for ease of assembly. After verifying the vacuum to hold below 10^{-5} torr pressure, disconnected from the pump, for sufficiently long times, a series of cooldowns of the Simons Array optics tubes were carried out, with each iteration containing a more complete assembly of the cryostat before integration with its backend cryostat. Figure 4.21 shows the standalone configuration of the POLARBEAR-2c optics tube. The POLARBEAR-2b optics tube was also cooled and validated in an identical configuration. Tables 4.13 and 4.14 list each iteration of optics tube cooldown and its objectives for POLARBEAR-2b and POLARBEAR-2c, respectively.

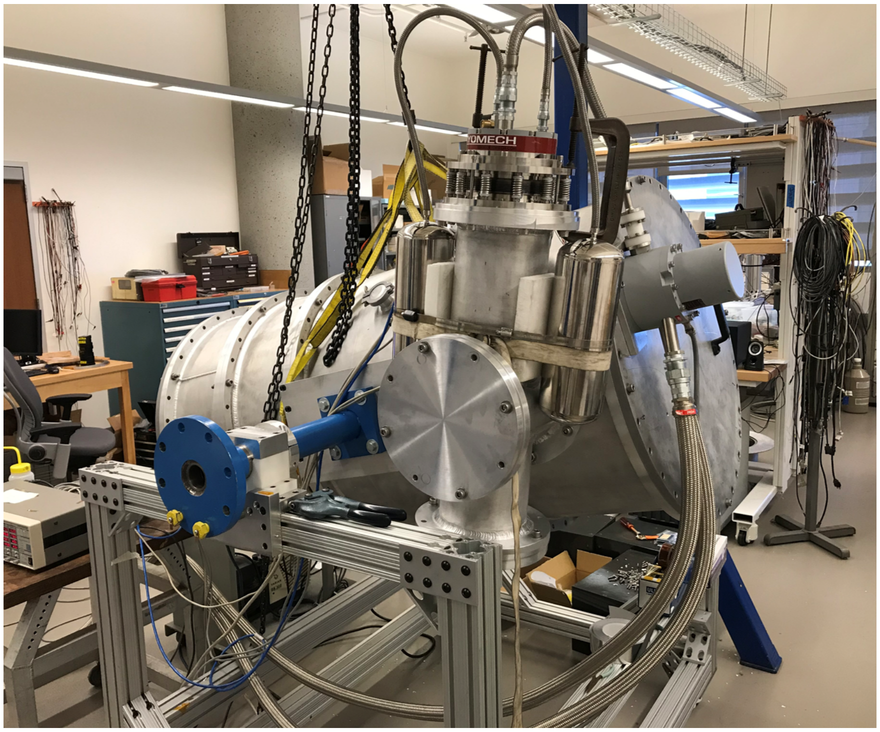

Figure 4.21: Standalone configuration of the POLARBEAR-2c optics tube.

POLARBEAR-2b and POLARBEAR-2c optics tubes were cryogenically validated in January - November, 2018 and June - December, 2019, respectively. The lessons learned from the POLARBEAR-2b validation process contributed to the relatively short validation process of the POLARBEAR-2c process. Some significant details of the optics tube components and assemblies are listed below.

- RUAG MLI[12] is utilized on every non-optical surface to reduce radiative loading on the PTC stages. 50 layers cover the 50 K shell and 20 layers cover the 4 K shell.

---

[12] https://www.ruag.com/en/products-services/space/spacecraft/multi-layer-insulation

- High conductivity materials are used to make the thermal links of the optics tube, such as aluminum 1100, 6N aluminum and OFHC copper with their thermal conductivity, k, of $\sim$50 and 300, 10^5 and 800, and 600 and 2000 $\mathrm{Wm^{-1}K^{-1}}$ at 4 and 50 K, respectively [66][67][60][13].
- Phosphor bronze helicoils are utilized on every threaded hole of a thermal interface between two separate parts. Apiezon-N cryogenic grease and 0.13 mm thick indium foil are also applied on thermal interfaces.
- Auxiliary 6N (99.9999% purity) aluminum foils of 1 mm thickness are incorporated as parallel paths of heat to boost thermal conductivity in parts of optics tube where thermal conductivity lacks due to design. This includes thin-walled optics tube shells, welding joints in the path of heat conduction such as optics tube flanges to cylindrical shells, interfaces between optics tube flanges, lens thermal links to their mounts, and thermal links between the temperature stages of the PTC to their respective optics tubes. Figure 4.22 shows two examples of their use.
  - Thermal interfaces between two parts are often the weakest link in a system which aims to maximize thermal conductance due to the unavoidable inclusion of micropores between two adjoinging surfaces without perfect parallelism and surface polish. Apiezon-N and indium foil are utilized due to their ability to fill these voids and also have high cryogenic thermal conductivity.
  - Apiezon-N has significantly lower thermal conductivity than indium at 4 K but indium is characterized by a dangerously close superconducting transition temperature of 3.4 K for which conductivity plummets.
  - While interface conductance certainly improves from filling these voids, it is nearly[14] always better to reduce the volume of micropores using parallel surfaces and increasing the force between adjoining surfaces with helicoils and split lock washers or belleville washers [56][57].
  - Between copper-copper interfaces, fillers are not used due to the malleability of OFHC copper. Between aluminum-aluminum interfaces which make up the majority of the surface area of interfaces, a small amount of Apiezon-N is used due to their ease of application and low cost. Between copper-aluminum interfaces, indium foil is cut into matching shapes due to the risk of generating fractures within Apiezon-N between these surfaces with mismatching coefficient of thermal expansion and the glass transition of Apiezon-N [44].

To characterize the flow of heat through the optics tube, we use Fourier's law of heat conduction,

$$P = kA\frac{dT}{dx} \tag{4.6}$$

---

[13] R=100 OFHC Copper

[14] Indium and gold plating improves thermal interface conductance but are impractical to apply on large surface areas.

Figure 4.22: 6N Al use for lens thermal link, optics tube shells, heat links.

where P is power flux, k is thermal conductivity, and x is the dimension of interest. Integrating this equation gives,

$$P = \frac{1}{L}\int_{T_{\mathrm{low}}}^{T_{\mathrm{high}}} kAdT. \tag{4.7}$$

In characterizing a cryogenic system, this equation is more usefully redefined as,

$$P = \int_{T_{\mathrm{low}}}^{T_{\mathrm{high}}} CdT \tag{4.8}$$

where C is thermal conductance which incorporates the geometric properties of the physical parts. This equation was used to better understand the conductive flow of power through the optics tube between iterations of cooldowns, and motivated the changes to the POLARBEAR-2b cryogenic system such as the complete redesign of the 50 K heat link in run 3, incorporation of helicoils in run 5, and increase in 6N aluminum stack count in run 4 and 7.

Location	**Temperature (K)**
4 K PTC coldhead	3.3
50 K PTC coldhead	38.5
4 K heatlink	3.6
50 K heatlink	54.6
4 K shell bottom	9.2
Field lens flange	10.6
Field lens center	9.1
Aperture lens flange	9.1
Aperture lens center	9.3
50 K shell top	69.0
50 K shell middle	59.1
50 K shell bottom	80.3

Table 4.15: Measured temperatures of the POLARBEAR-2b optics tube validation.[15]

Location	**Temperature (K)**
4 K PTC coldhead	2.8
50 K PTC coldhead	41.5
4 K heatlink	3.7
50 K heatlink	54.0
4 K shell top	6.9
Field lens	12.5
Lyot	8.0
Aperture tube shell	8.7
50 K shell top	68.4
50 K shell bottom	82.5

Table 4.16: Measured temperatures of the POLARBEAR-2c optics tube validation.

The measured temperatures of the optics tube upon final validation are shown in Tables 4.15 and 4.16. Based on measured load curves of the PTCs, the POLARBEAR-2b optics tube draws 0.8 W and 38 W of power on the 4 K and 50 K PTC stages, respectively, and the POLARBEAR-2c optics tube draws 0.4 W and 45 W of power on the 4 K and 50 K PTC stages, respectively. With the receiver system designed such that the backend PTC contributes to cooling of parts near the “bottom” of the optics tube, we determined these temperatures to be sufficiently low for required temperatures of optics tube validation and integration with the backend cryostat.

---

[15] Lyot temperature is validated upon integration with backend

POLARBEAR-2b receiver integration

We integrated the POLARBEAR-2b optics tube and backend into the receiver on November - December, 2019. A picture of the integrated receiver is shown in Figure 4.23 and achieved base temperatures in Table 4.17. This receiver configuration utilizes aluminum blank-offs in place of the optical window and IR filter.

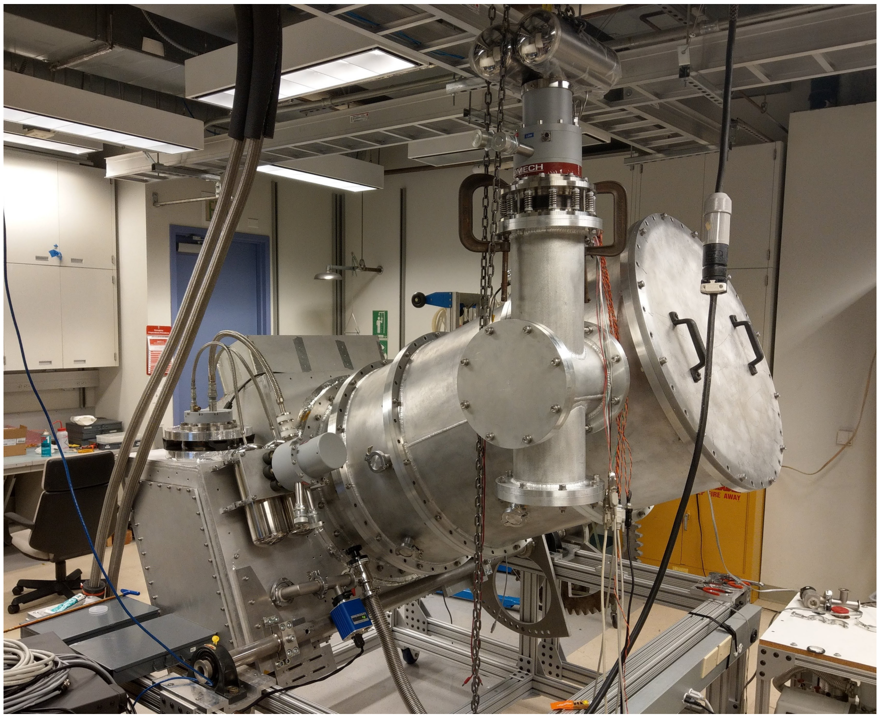

Figure 4.23: Integrated POLARBEAR-2b receiver, courtesy of Jennifer Ito.

Location	**Temperature (K)**
4 K optics tube coldhead	3.7
50 K optics tube PTC coldhead	34.5
4 K optics tube bottom	4.4
50 K optics tube bottom	52.0
4 K optics tube top	13.8
50 K optics tube top	40.9
Field lens	6.2
Aperture lens	4.6
Lyot	4.4
Collimator lens	4.4
4 K backend coldhead	3.2
50 K backend coldhead	35.5
4 K backend mainplate	3.2
50 K backend front	49.9

Table 4.17: Measured temperatures of the POLARBEAR-2b integrated receiver.

Chapter 5

Anti-Reflection Coatings

Lord Rayleigh first noticed in 1886 that a glass whose surface had been tarnished transmitted light more efficiently than a glass with a polished surface. This roughened surface effectively acted as an AR coating by replacing the air-glass dielectric boundary and its change in index of refraction. Fresnel equations describe the reflectance of incident s- and p-polarized radiation on an interface between different media, characterized by different indices of refraction n_1 and n_2,

$$\begin{aligned} r_s &= \left| \frac{n_1 \cos\theta_i - n_2 \cos\theta_t}{n_1 \cos\theta_i + n_2 \cos\theta_t} \right|^2 \\ r_p &= \left| \frac{n_1 \cos\theta_t - n_2 \cos\theta_i}{n_1 \cos\theta_t + n_2 \cos\theta_i} \right|^2 , \end{aligned} \tag{5.1}$$

where θ_i and θ_t are angles of incidence and transmittance, respectively. For normal incidence, the reflectance of both polarization states are given by

$$r = \left| \frac{n_1 - n_2}{n_1 + n_2} \right|^2 . \tag{5.2}$$

For an alumina or silicon lens with $\epsilon \sim 10$, typically used for modern CMB experiments, nearly 30% of incident light is reflected per vacuum-lens interface according to Equation 5.2 and nearly 50% of incident light per lens, leading to loss of precious CMB signal and to sidelobe systematics due to high levels of reflection at every optical surface. This is directly opposed to the fundamental design goals of high fidelity, high efficiency optics and highlights the importance of an appropriate AR coating for modern CMB experiments.

5.1 Quarter-Wave Impedance Transformer Design

Lord Rayleigh's tarnished glass surface transmits light more efficiently because the surface works as a pseudo-AR coating by reducing the rate of change in dielectric constant at the air-glass interface. AR coatings are formed by placing one or more dielectric layers on a vacuum-dielectric boundary of a refractive optical element. Using the principle behind quarter-wave impedance matching, its boundary conditions are met by tuning each layer's dielectric constant and thickness such that the reflected light at every boundary destructively interferes. Figure 5.1 shows a diagram of a transmission line of impedance Z_0 and length l, which is terminated at some load with a different impedance Z_L. Without correctly tuning Z_0 and l, an incoming wave is reflected from termination back to the input source. The combination of the reflected and incident waves results in the input impedance,

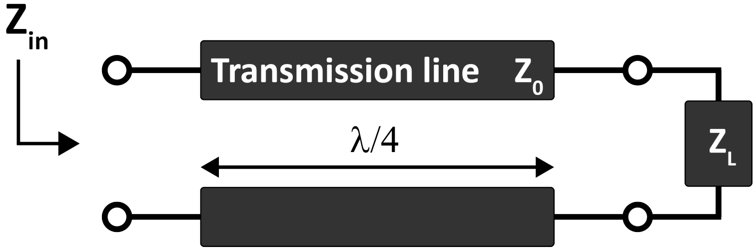

Figure 5.1: Schematic diagram of quarter wave impedance transformer.

$$Z_{\text{in}} = Z_0 \left(\frac{Z_L + iZ_0 \tanh(kl)}{Z_0 + iZ_L \tanh(kl)} \right) \tag{5.3}$$

where $k = 2\pi/\lambda$. For a quarter-wave thickness, $l = \lambda/4$ and $kl = \pi/2$ such that the above equation simplifies to,

$$Z_{\text{in}} = \lim_{kd \to \frac{\pi}{2}} Z_0 \left(\frac{Z_L + iZ_0 \tanh(kl)}{Z_0 + iZ_L \tanh(kd)} \right) = \frac{Z_0^2}{Z_L} \tag{5.4}$$

and

$$Z_0 = \sqrt{Z_{\text{in}} Z_L}. \tag{5.5}$$

A simple application is that of a single layer AR. Since impedance and dielectric constant are related by

$$Z = \sqrt{\frac{\mu_0 \mu}{\epsilon_0 \epsilon}}, \tag{5.6}$$

then for a quarter-lambda thickness AR coating, $\epsilon_c = \sqrt{\epsilon_s}$, where ϵ_c and ϵ_s are dielectric constants of the coating and substrate, respectively, and its thickness is $\lambda/(4\sqrt{\epsilon_c})$. The bandpass of this AR coating is designed for minimum reflection of power at λ. The AR coating technologies, detailed throughout this chapter, are millimeter-wave applications of this impedance matching.

5.2 Multi-Layer AR Coating

As Simons Array and other modern CMB experiments observe multiple frequency bands simultaneously for component separation, the optics will also need to facilitate broadband observation with the appropriate passband. Thus the AR coating is that of a multi-layer design with a high efficiency bandpass spectrum which does not introduce any significant levels of beam systematics. Lord Rayleigh remarked on the potential for gradual transition layer between two media of different properties to mitigate the reflection of incident light, stating "No one would expect a ray of light to undergo reflection in passing through the earth's atmosphere as a consequence of the gradual change of density with elevation [55]." We design a multi-layer AR coating which gradually changes the dielectric constant between the vacuum-alumina interface to increase the width of its bandpass and accommodate a multichroic observation of the CMB. The quarter-wave impedance transformation scheme described above can be generalized to the multi-layer design. I use the characteristic matrix formalism to develop a code which calculates the transfer matrix and solves for the transmitted and reflected field through an arbitrary stack of dielectrics. This code is used for all calculations shown in this chapter.

The incident and reflected electric field at the first interface of an N-layer stack of dielectrics, shown in Figure 5.2, can be related to the incident and reflected fields at the last interface using matrices via,

$$\begin{pmatrix} E_0^+ \\ E_0^- \end{pmatrix} = \frac{1}{\eta_0} \begin{pmatrix} 1 & r_0 \\ r_0 & 1 \end{pmatrix} \prod_{j=1}^{N} \frac{D_j}{\eta_j} \begin{pmatrix} E_{N+1}^+ \\ E_{N+1}^- \end{pmatrix} \tag{5.7}$$

where $\eta_j = 1 + r_j$ and D_j is the refraction matrix,

$$D_j = \begin{pmatrix} X_{ij} & 0 \\ 0 & X_{ij}^{-1} \end{pmatrix} \begin{pmatrix} 1 & r_j \\ r_j & 1 \end{pmatrix}. \tag{5.8}$$

The refraction matrix contains a wave propagation term, given by

$$X_{ij} = \exp\left[i\left(2\pi/\lambda\right) l_{ij} n_j \cos\theta_j\right] \tag{5.9}$$

where l_{ij} is the thickness of the layer between the i-th and j-th interface, n_j is its index of refraction, and θ_j is the angle of refraction within it. With the refraction matrices expressed as,

$$\prod_{j=1}^{N} D_j = \begin{pmatrix} N_{11} & N_{12} \\ N_{21} & N_{22} \end{pmatrix} \tag{5.10}$$

and the boundary condition, $E_{N+1}^- = 0$, imposed, the transmittance function is analytically solved to be

$$T_N = \frac{E_{N+1}^+}{E_0^+} = \prod_{i=0}^{N} \frac{\eta_i}{N_{11} + r_0 N_{21}}. \tag{5.11}$$

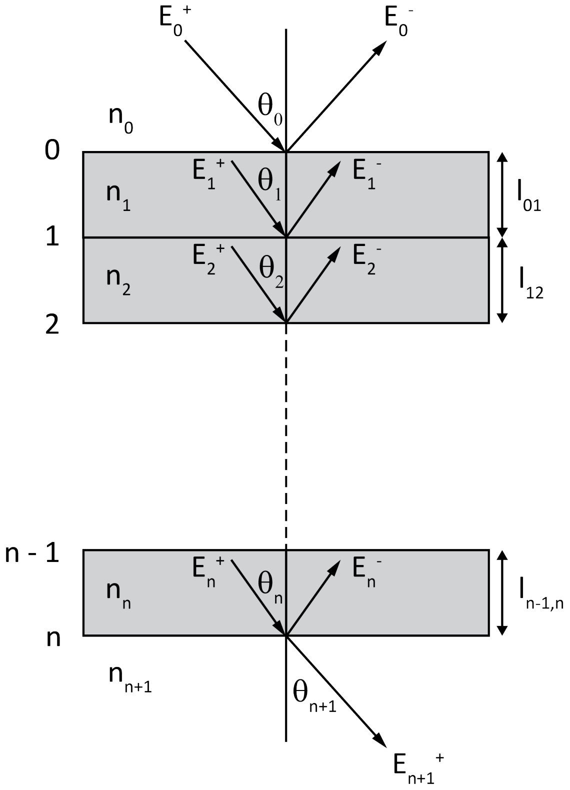

Figure 5.2: Schematic diagram of an N-layer stack of dielectrics.

Application of multiple layers of coating presents a significant challenge in fabrication and operation. These coatings require a different dielectric constant for each layer, with fine tunability of dielectric constant necessary for flexible optimization for different experiments. The loss tangents of the coating must be sufficiently low to minimize absorptive loss of the optics. Perhaps most importantly, cryogenic operation of refractive optics inside the receiver require matched coefficients of thermal expansion between every AR layer to the substrate. Multiple AR coating technologies are available in the field of CMB using dielectric layers, metal mesh layers, or sub-wavelength metamaterial structures. However, these existing technologies involve a complicated fabrication process or are at risk of cryogenic delamination. This chapter presents the application of Stycast epoxies and plasma sprayed ceramics to construct AR coating solutions which demonstrate high optical efficiency for larger aperture optics with robust adhesion in cryogenic temperatures.

Design and Requirements

The performance requirements of this AR coating technology are set by the optical design goals of the Simons Array experiment but are generalizeable for other CMB cameras. The challenge of Simons Array and other projects with multichroic detector arrays is to design a broadband AR coating with $\leq 1\%$ reflectance for each optical element, averaged across the observation bands. Figure 3.5 shows the cross-section of a Simons Array refractive optics chain. Given the number of refractive optics with each surface being a vacuum-dielectric boundary, it is critical to meet the requirement of minimal reflectance to maximize optical efficiency. Perhaps the most difficult requirement for AR coatings in CMB polarimetry experiments is to be robust against cryogenic thermal cycling. Like Simons Array, most CMB experiments operate with refractive optics at 4 K or below to reduce thermal emission and absorption loss. Coatings without a sufficiently matched coefficient of thermal expansion to alumina and silicon will delaminate upon thermal cycling, a catastrophic outcome for CMB experiments. This becomes a more difficult challenge with multi-layer coatings for broadband optics with more dielectric layers to match in thermal coefficient.

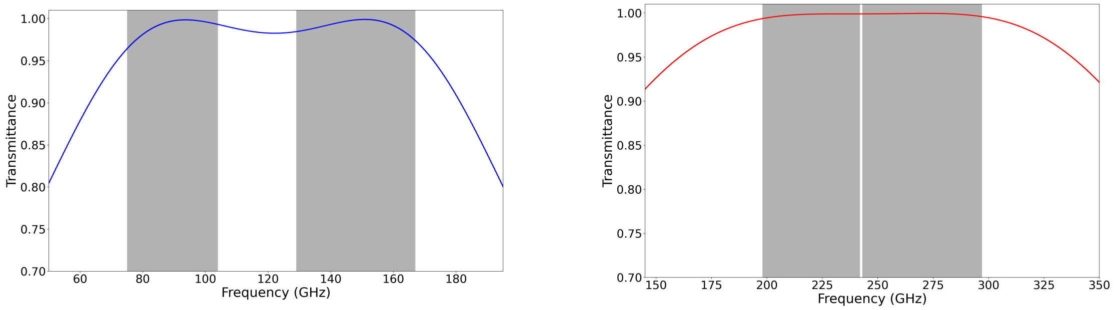

Figure 5.3: Theoretical transmittance spectra of alumina AR coatings for optimal performance at 95/150 GHz bands (*left*) and 220/280 GHz bands (*right*).

The optimized transmittance spectra of a two-layer AR coating on alumina for the 95/150 GHz and 220/280 GHz dual bands of Simons Array, found using Equation 5.11, are shown in Figure 5.3. We present the parameters and reflectance of the calculated ideal stack of dielectrics for the bands of Simons Array in Table 5.1. The 95/150 GHz sample shows reflection suppressed to below 5% over 87% fractional bandwidth for 0.9% and 0.9% band-averaged reflectance at 95 and 150 GHz, and 220/280 GHz sample shows reflection suppressed to below 5% over 71% fractional bandwidth for 0.2% and 0.1% band-averaged reflectance at 220 and 280 GHz. Furthermore, coating thicknesses of $O(100\ \mu\text{m})$ must be controlled to $O(25\ \mu\text{m})$ to control additional reflection due to thickness non-uniformity to below 1% as shown in Figure 5.4.

5.3 POLARBEAR-2a AR Coating

Between 2014 and 2016, we AR coated the POLARBEAR-2a refractive optics using a combination of Stycast epoxy coating based on the work of [10] and Mullite-Skybond coat-

Passband	**Top layer**		**Bottom layer**		**Reflectance (%)**
	ϵ	thickness (μm)	ϵ	thickness (μm)	
95/150 GHz	2.04	427	5.22	427	0.89
220/280 GHz	2.04	210	6.17	123	0.17

Table 5.1: Two-layer AR coating design parameters and reflectance performance

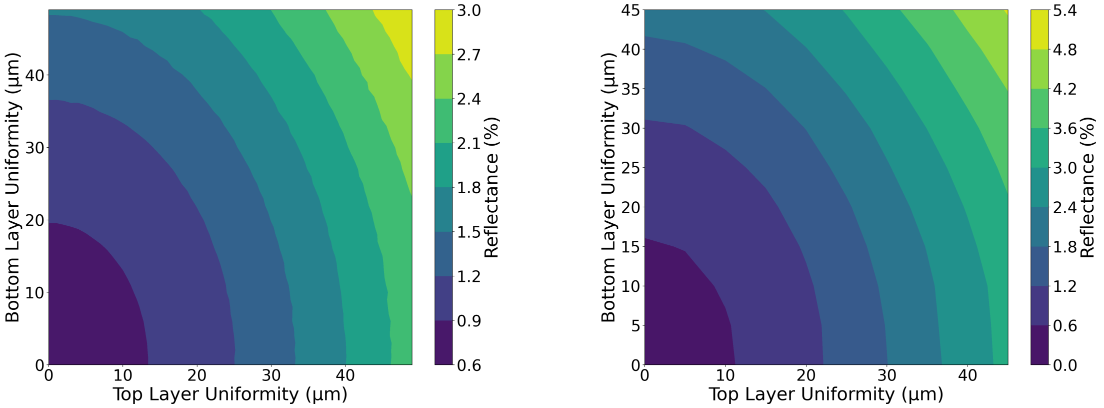

Figure 5.4: Monte Carlo study on the effect of thickness non-uniformity on efficiency of one optical element, coated on both sides, with 95/150 GHz bands (*left*) and 220/280 GHz bands (*right*). An AR layer with non-uniform thickness is simulated by averaging 500 trials of a Gaussian distribution around optimal thickness value with fixed standard deviation. These trials are done for standard deviations ranging from 0 to 50 μm. The axes represent this standard deviation around the optimal thickness for a set of trials. This study shows that a non-uniformity of 25 μm in both layers leads to a loss of $\sim$1% in efficiency.

ing, developed by collaborators at the High Energy Research Organization (KEK) [25]. [10] presents a multi-layer epoxy-based AR coating for millimeter-wave optics using a combination of Henkel Loctite's[1] Stycast 1090, Stycast 1266B, and Stycast 2850FT[2] and measured their dielectric constants to be 2.06, 2.6, and 4.95, respectively. The range of dielectric constants achievable with Stycast epoxy and the achieved passband spectra are shown in Figures 5.5 and 5.6. The two-layer design consists of a bottom layer of Stycast 2850FT + Catalyst 23LV and a top layer of Stycast 1090 + Catalyst 9, aiming for dielectric constants of 2 and 5. Stycast 2850FT is an epoxy resin loaded with microscopic alumina grain. This alumina loading raises the thermal conductivity and dielectric constant and lowers the loss tangent and coefficient of thermal expansion mismatch with the alumina substrate. Mixed

---

[1] Previously known as Emerson Cummings

[2] https://www.henkel-adhesives.com/sg/en/about/our-brands/loctite.html

with Catalyst 23LV, the epoxy has a 2 hour hardening time, which is sufficient for the lens coating process. 1090 is an epoxy resin loaded with ∼50 μm diameter hollow silica microspheres which lowers the effective dielectric constant. Catalyst 9 is chosen for its low dielectric constant. The high optical efficiency over the POLARBEAR-2 bands and cryo-mechanical robustness were demonstrated with a 100 mm diameter alumina plate [24].

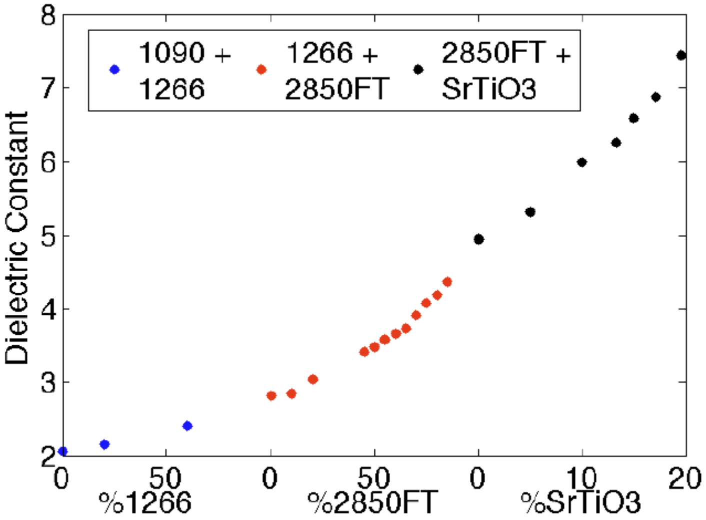

Figure 5.5: Range of achievable dielectric constants of various epoxy mixtures at room temperature as a function of percent weight of mixture [10].

I worked with the UC Berkeley Machine Shop to develop a process which coats a convex alumina surface using a negative mold, then machines the coating to shape using a precision CNC mill, scaling up from small to large format validation. Restrictions in the coating machining process dictated the development process for fabrication of large format coatings, as the available CNC machines were not large enough in throw to cut the entire surface in a single step. We addressed this by rotating the lens 180° around its optical axis to cut the surface in two halves. This process had to meet the precision and accuracy requirement, shown in Figure 5.4, thus aimed to be within 13 μm of target thickness and 25 μm RMS uniformity for each layer. The CNC milling machine was prepared in such a way that the coating surfaces were not at risk of contamination from the oils of the machine.

The coating fabrication procedure was first validated at small scale using a mock lens with 150 mm diameter and 629.72 mm radius of curvature. We based this procedure on the single-layer AR fabrication process developed by the team at Stanford University for the BICEP3 95 GHz receiver [26]. The lens is lowered using a crane onto a negative mold facing up towards the sky. Figure 5.8 shows the negative mold and the lens fixture assembly. Shims of desired coating thickness are super-glued onto the round spacer parts such that when the lens fixture assembly is fully lowered onto the negative mold, the shims make contact with

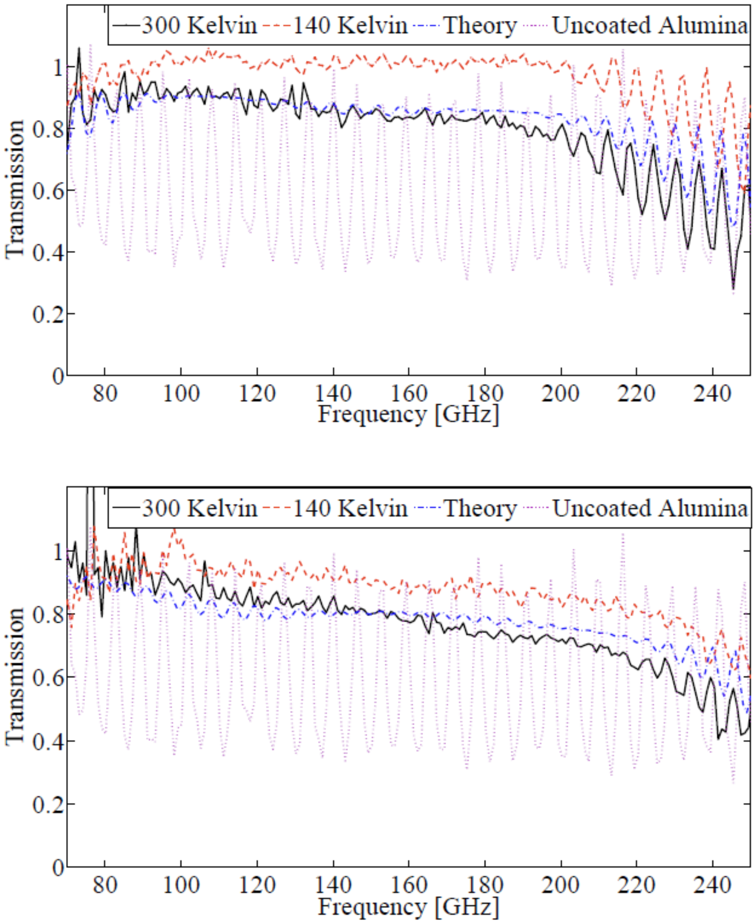

Figure 5.6: Transmittance spectra of two-layer (*top*) and three-layer (*bottom*) epoxy coated alumina at 300 and 140 K [10].

the mold and define the gap between the lens and mold surfaces, thus also determining the coating thickness. The shim thickness is chosen to be a $\sim 50\ \mu$m thicker to allow the precision computer numerical control (CNC) machine cutting process to define the coating thickness. The epoxy mixing process is designed in the following way to provide a uniform mixture with minimal number of scattering voids:

1. Heat Stycast at 50 °C for 1 hour.
2. Stir Stycast inside its container using a paddle attached to a power drill (shown in Figure 5.7).
3. Hand stir the Stycast and catalyst mixture for 10 minutes.
4. Place mixture inside vacuum chamber, shown in Figure 5.7, and pump for 2 minutes.

Figure 5.7: Epoxy mixing process inside vacuum chamber. The chamber has a vacuum-tight feedthrough for paddle rod attached to power drill, held by the author, which is utilized for a uniform mixing procedure.

5. Mix using paddle for 10 minutes.
6. Pump for 5 minutes.
7. Mix using paddle for 5 minutes.
8. Pump for 5 minutes.
9. Slowly open to vacuum and inspect epoxy mixture for air bubbles.

The process, as shown in pictures in Figure 5.8, is the following:

1. Apply 8 layers of Honey wax mold release[3] on negative mold and 3 layers on every other part minus the lens optical surface which comes into contact with epoxy.
2. Put together lens fixture assembly and cover spacer parts, without shims attached, with foam tape to prevent epoxy adhesion. Apply Lord AP-134 adhesion enhancer[4] on lens surface.
3. Attach lens fixture to crane and flip upside down such that surface to be coated is facing down towards the mold.

---

[3] https://www.stonermolding.com

[4] https://www.lord.com/products-and-solutions/chemlok-ap-134-primer

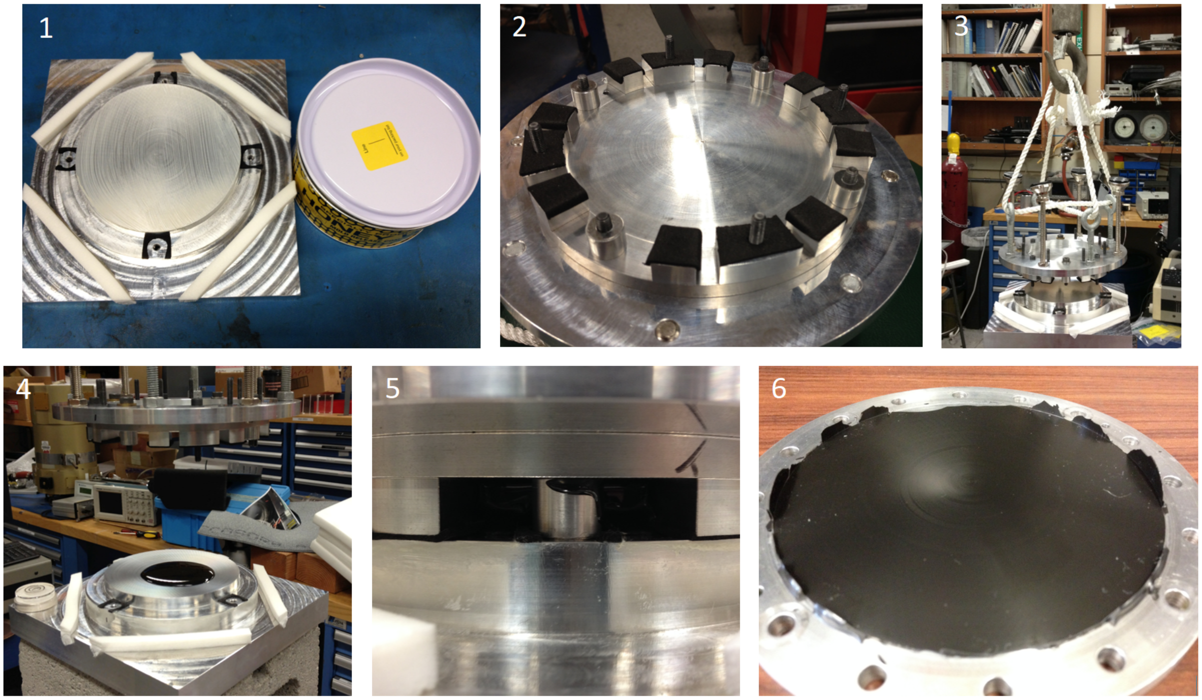

Figure 5.8: Lens coating process for small scale validation shown in pictures.

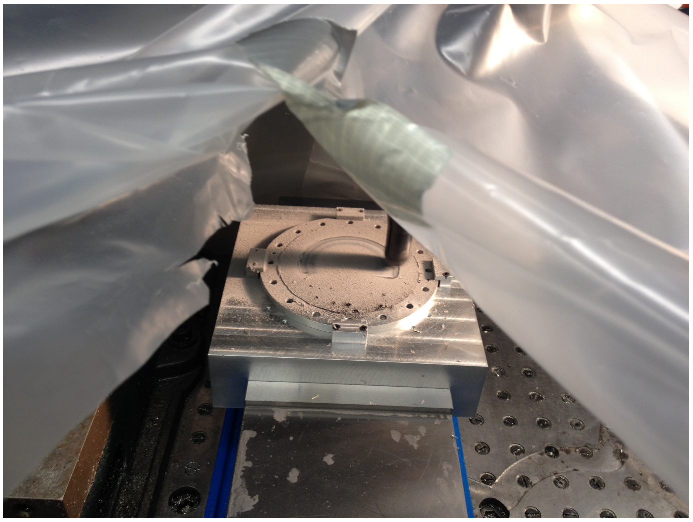

Figure 5.9: CNC machining of small scale validation lens coating.

4. Mix epoxy and pour carefully on mold as to not introduce air bubbles.
5. Lower the crane onto negative mold until shims make contact with mold. Epoxy should

leak uniformly around lens diameter. Leave the epoxy to cure for 2 days.

6. Raise and separate coated lens from negative mold.

Application of a thin, uniform layer of adhesion enhancer is crucial for cryo-mechanical robustness. A cellulose sponge is used to apply a 50:50 mixture of AP-134 and isopropyl alcohol in straight line motions along 0°, 90°, 45°, and 135° on the lens surface. The cured coating surface is then cut on a dedicated CNC milling machine with a diamond coated carbide tool bit. The CNC lens fixture, cut from Mic 6 aluminum for its thermal and mechanical stability, is skim cut on the top surface before lens mounting to ensure parallelism between the CNC xy-plane and lens xy-plane. A 6 mm dowel pin is placed in matching clearance holes on the lens flange and fixture for precision alignment when the lens is rotated by 180° or re-placed on the fixture. Figure 5.9 shows the machining process of the 150 mm diameter mock lens which was coated with Stycast 2850FT and 1090 to thicknesses of 270 ± 13 μm and 422 ± 15 μm, respectively, measured using a CMM. We made hundreds of height measurements using a CMM on the optical surface before and after coating to determine the thickness of the coating. Repeatability and alignment to < 13 μm is critical for accurate information of coating thickness to within the optical tolerances set by Figure 5.4.

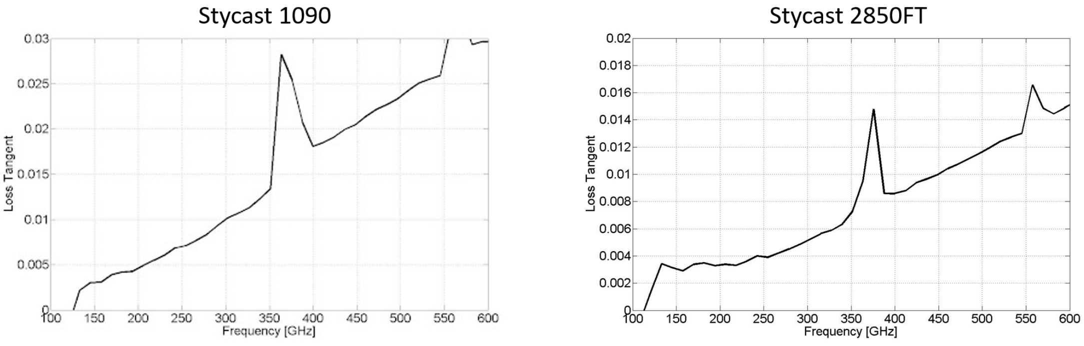

Figure 5.10: Loss tangent of 1090 and 2850FT measured at 4 K.

We used the FTS, shown in Figure 4.2, to measure the dielectric properties of Stycast 1090 and 2850FT. For each Stycast, three coupons of 6.35 mm thickness were made, with each coupon made from a different can of epoxy resin and different time, and measured to verify the repeatability of epoxy coating dielectric constant. Every sample for each Stycast showed identical dielectric constants of $\epsilon_r = 2.05 \pm 0.05$ and 5.05 ± 0.05 at 300 K for Stycast 1090 and 2850FT, respectively. Cryogenic measurements of epoxy are difficult at 51 mm diameter due to its relatively poor thermal conductivity. Loss tangent is measured at 4 K using 2.54 mm diameter samples, as shown in Figure 5.10. At 126 GHz[5], the loss tangent is measured to be $\tan\delta = 0.002$ and 0.0025 for Stycast 1090 and 2850FT, respectively.

---

[5] center frequency for optimized POLARBEAR-2 AR coating

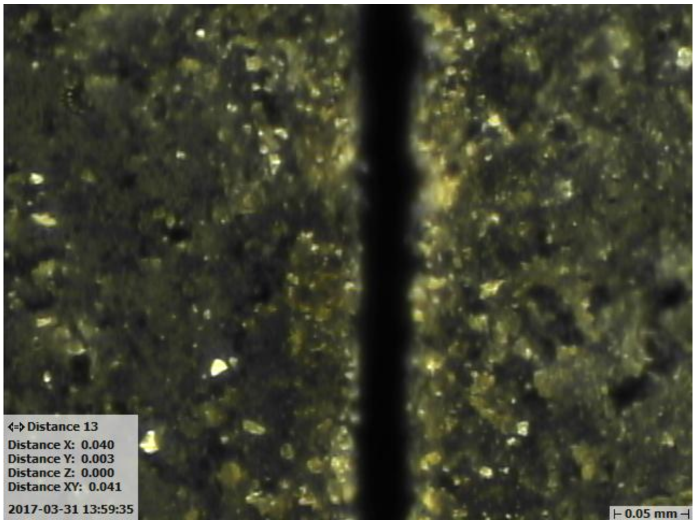

Figure 5.11: Stress-relief groove on a POLARBEAR-2a AR coating surface.

HFSS[6] simulation of 3 mm normal incidence light on 25 um groove cut into $\epsilon = 5$ dielectric shows a -40 dB diffraction effect, which is sufficiently low for stress-relief grooves. Shown in Figure 5.11, these stress-relief grooves are cut all the way down to the alumina substrate via laser dicing[7] at 1 cm pitch for every epoxy-coated surface in POLARBEAR-2a optics.

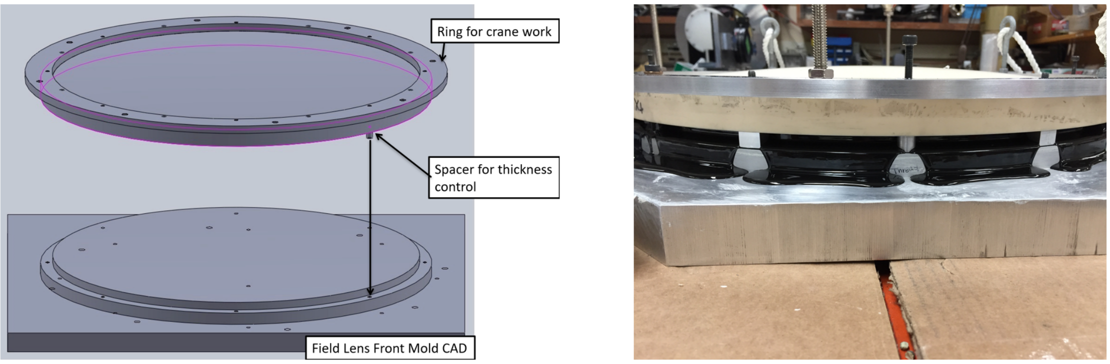

Figure 5.12: Mold coating process for POLARBEAR-2a field lens.

Upon completing the small-scale validation process, we AR coated the curved surfaces of POLARBEAR-2a optics using a method that is simply scaled-up from the 150 mm diameter process, with the addition of an abrasive grit blast on coating surfaces with pure alumina media to aid in mechanical adhesion of the coating. The mold design CAD and the mold

---

[6] https://www.ansys.com/products/electronics/ansys-hfss

[7] https://laserod.com

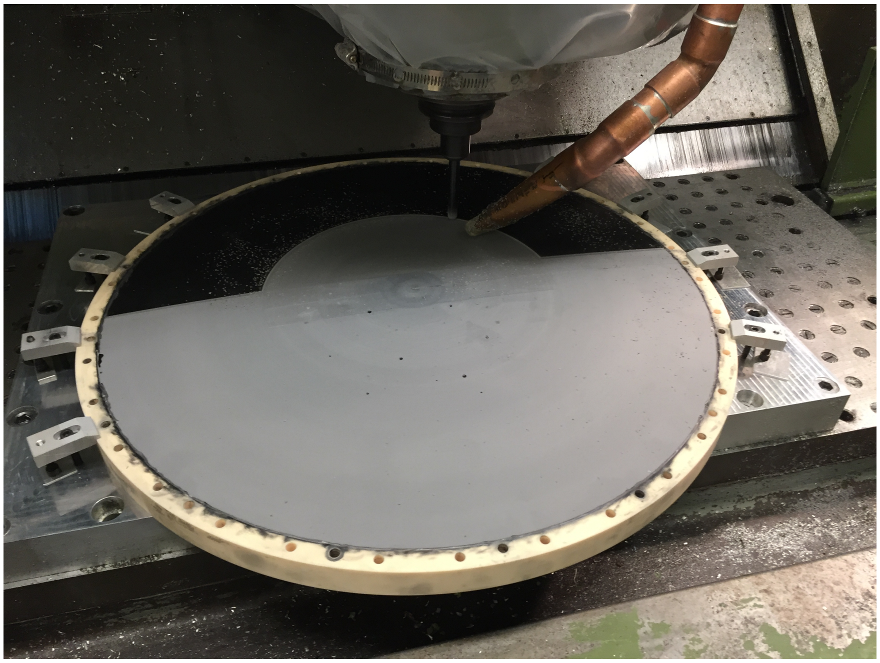

Figure 5.13: CNC machining in halves of the POLARBEAR-2a field lens.

coating process for a POLARBEAR-2a lens is shown in Figure 5.12. Figure 5.13 shows the machining process for the POLARBEAR-2a field lens and Figure 5.14 shows a completed POLARBEAR-2a lens after laser dicing.

Figure 5.15 shows a representative contour plot of an epoxy AR coating for POLARBEAR-2a. We present the measured thickness of every layer of the POLARBEAR-2a lenses in Table 5.2. While time-constraints prevented measurements of transmittance spectra of these lenses, band-averaged optical throughput measurements and Gaussianity from near-field beam measurements of the full receiver at KEK were deemed satisfactory for deployment in 2018 [9].

Layer	**Coating**	**Target (μm)**	**Measured thickness (μm)**			
			Collimator	**Aperture**	**Field**	
					1375mm	3160mm
1	2850FT	280	289 ± 16	281 ± 16	280 ± 9	280 ± 5
	Mullite	235	270 ± 6	260 ± 6	-	-
2	1090	442	457 ± 16	418 ± 12	418 ± 10	425 ± 8
	Skybond[8]	390	390 ± 10	390 ± 10	-	-

Table 5.2: Measured thicknesses of POLARBEAR-2a AR coatings.

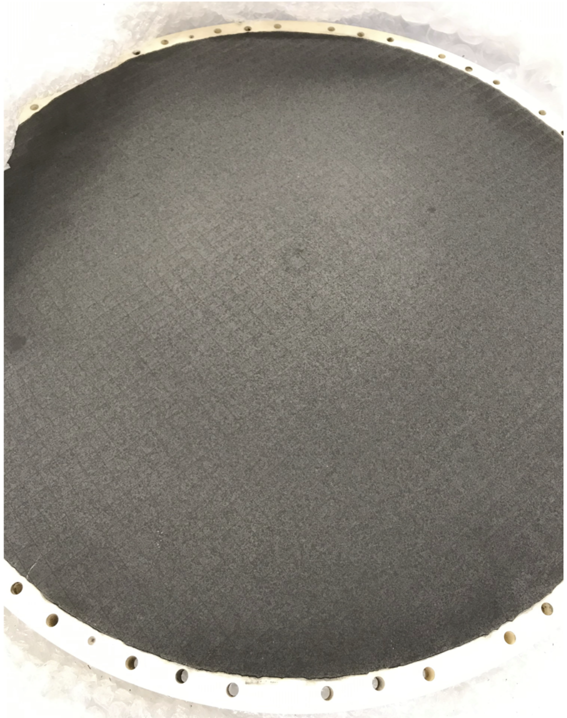

Figure 5.14: Completed POLARBEAR-2a field lens.

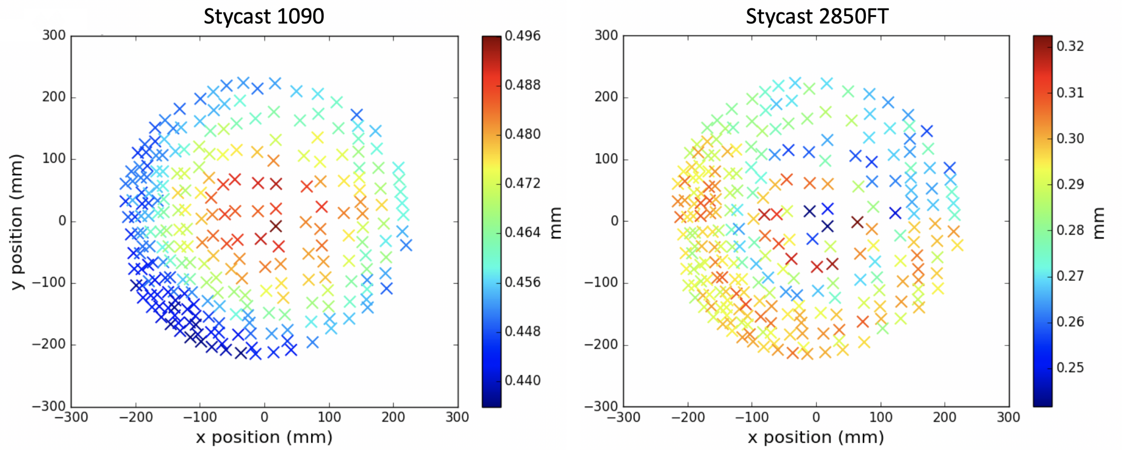

Figure 5.15: CMM measurement of the POLARBEAR-2a aperture lens curved-side AR coating thicknesses.

5.4 Plasma Spray AR Coating

This work is based on and expanded upon in Jeong et al [41] and Jeong et al [42], which the reader is encouraged to cite instead of this dissertation.

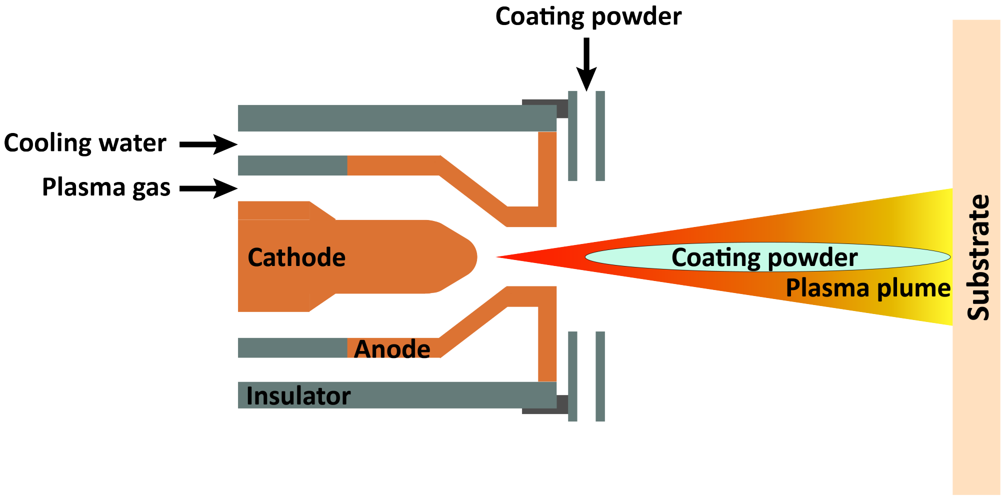

Figure 5.16: Schematic diagram of a plasma spray gun.

We present a broadband plasma sprayed AR coating technology which we developed for cryogenic millimeter-wave optics. Plasma spray is a thermal coating process which heats a material to a molten state and propels it towards a substrate using an inert gas plasma jet of temperature of order $\sim 10^5$ K. It utilizes a chamber with a cathode and anode, as shown in Figure 5.16, where direct current is applied to generate a powerful electric arc of $\sim 10^4$ W. An inert process gas such as Argon and Helium is flown into this chamber to be ionized upon contact with the arc and generate a plasma plume. Feedstock materials, most often oxides such as alumina powder, are injected into this plasma chamber where it is propelled with high temperature and momentum. The material droplet immediately flattens and cools upon contact with the substrate's gritted surface to form an adhered coating. This technology sprays a variety of different powders with composition consisting of aluminum oxide and silicon dioxide in solid and hollow shapes. Development of plasma sprayed AR coating required a separate process for the low dielectric constant top layer and the high dielectric constant bottom layer. We first sprayed matrices composed of HAI[9] alumina microsphere and Metco 6051[10] alumina solid powders to demonstrate the wide range of dielectric constants, as shown in Figure 5.17, that can be achieved. A higher concentration of microspheres leads to a higher value of dielectric constant, and vice-versa. However, due to the inherently high dielectric constant of the material used in the powder matrix, we could not achieve a sufficiently low dielectric constant for a multi-layer AR coating design. To spray the dielectric constant of $\epsilon = 2.0$ for an optimal two-layer design, we searched for microsphere powders composed of lower bulk dielectric constant material. Using an Omya Fillite[11] hollow

---

[9] https://www.haiinc.com

[10] https://www.oerlikon.com

[11] https://www.omya.com/

silica microsphere powder with changes to the plasma parameters for a colder plasma and molten powder with lower kinetic energy, this lower limit of dielectric constant was reached. A cross-sectional image of these coatings taken using a scanning electron microscope (SEM), shown in Figure 5.18, shows the micropores inherent to the coatings from spraying hollow microsphere powders.

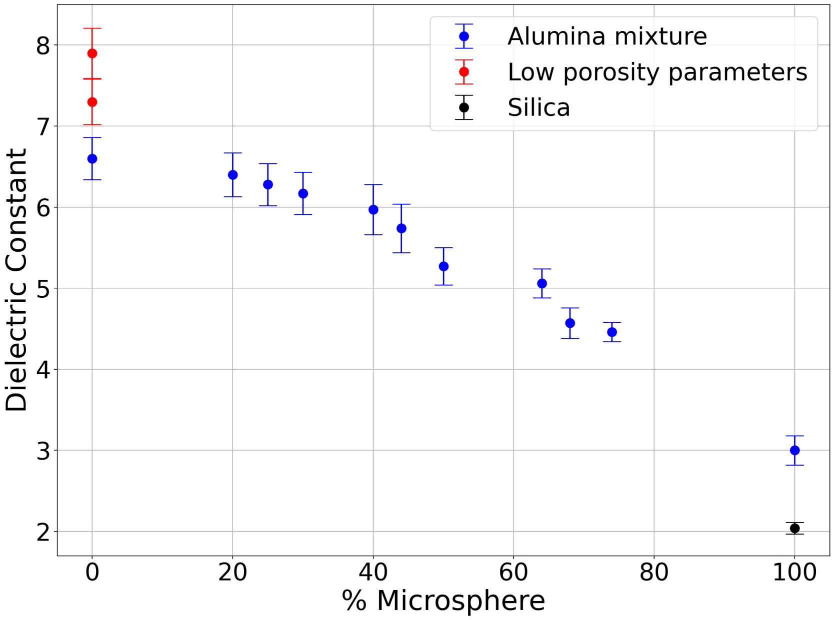

Figure 5.17: Range of achievable dielectric constant by varying the ratio of hollow alumina microspheres of the powder matrix and varying plasma spray setup parameters i.e. standoff distance.

Figure 5.17 is referenced to determine the powder matrix and spray parameters for the desired value. Due to this wide range of available values, a variety of AR coating designs can be fabricated from single layer to multiple layers. For the 95/150 GHz POLARBEAR-2b design, a powder matrix consisting of 48% alumina microspheres and 52% solid alumina is sprayed to fabricate the bottom layer. Then a powder matrix consisting only of silica microspheres is sprayed on top for an end-to-end plasma sprayed AR coating. For the 220/280 GHz POLARBEAR-2c design, a powder formulation of 68% alumina microspheres and 32% solid alumina is sprayed for the bottom layer. The top layer is identical to that of 95/150 GHz.

The loss tangent of plasma sprayed coatings is constrained to $< 10^{-3}$ at 100 K. This is due to limitations in the thickness build-up of spray coatings and the lack of sensitivity in the fitting algorithm to the measured spectra's low tilt from low level of absorption loss

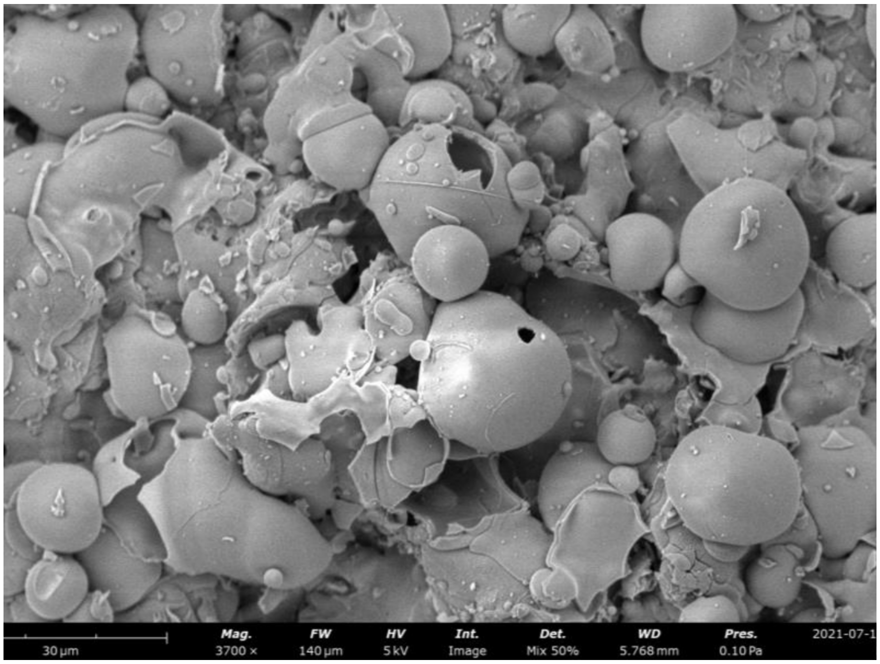

Figure 5.18: Cross-section image of a hollow silica microsphere coating taken via SEM. This image shows the thin-walled microspheres survive the plasma spray process and produces a coating with porous bulk structure. SEM image, courtesy of Christopher Raum.

through thin sprayed coatings. We calculate the scattering loss from 100 μm diameter silica microsphere top layer and 30 μ m diameter alumina microsphere bottom layer for the POLARBEAR-2b and POLARBEAR-2c AR coating designs, as shown in Figures 5.19 and 5.20, contributing a fraction of percent per two surfaces, averaged over both bands. This calculation is made using Equation 2.18, assuming random packing of equally sized spheres.

Performance

We sprayed 51 mm alumina coupons with AR coating designs described in Section 5.4 for 95/150 and 220/280 GHz coverage. The transmittance spectra of these samples were measured using the FTS as shown in Figure 5.21 at ambient and cryogenic temperatures. The 95/150 GHz sample has reflection suppressed to (0.4, 2.4, 1.6)% band-averaged reflectance at (95 GHz, 150 GHz, Total) at 100 K. The 220/280 GHz sample has reflection suppressed to (0.1, 0.3, 0.2)% band-averaged reflectance at (220 GHz, 280 GHz, Total) at 100 K. Since re-imaging lenses for CMB experiments typically operate at 4 K, we expect further reduction in absorptive loss at operating temperatures.

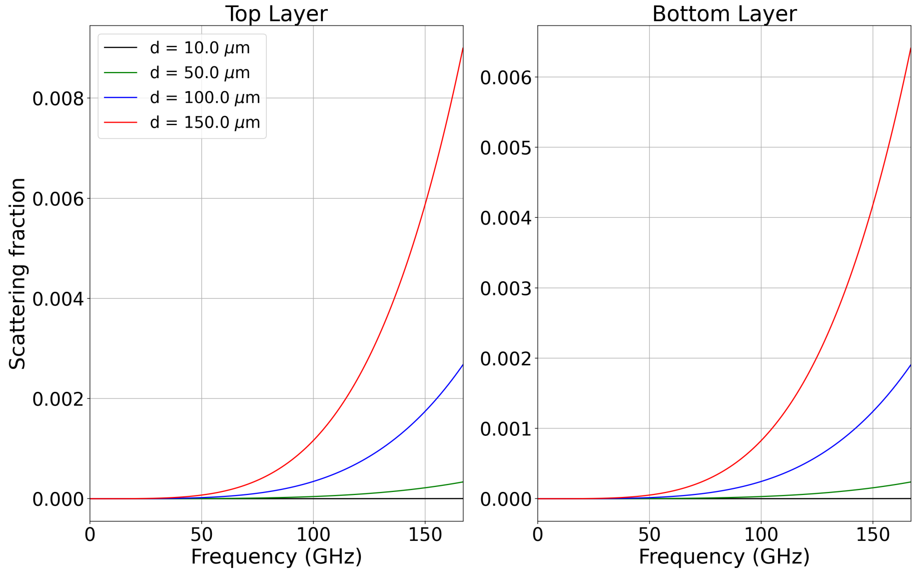

Figure 5.19: Scattering rate calculation for POLARBEAR-2b AR coating.

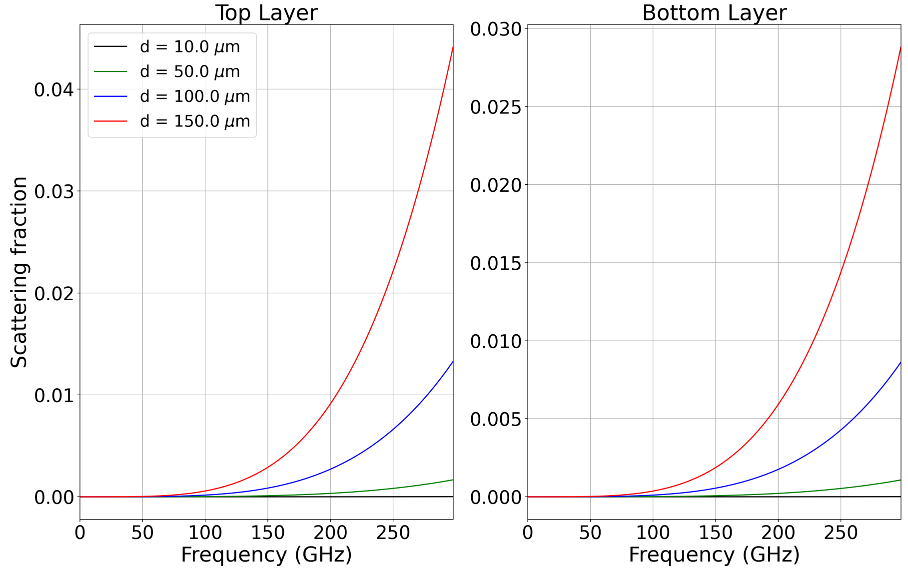

Figure 5.20: Scattering rate calculation for POLARBEAR-2c AR coating.

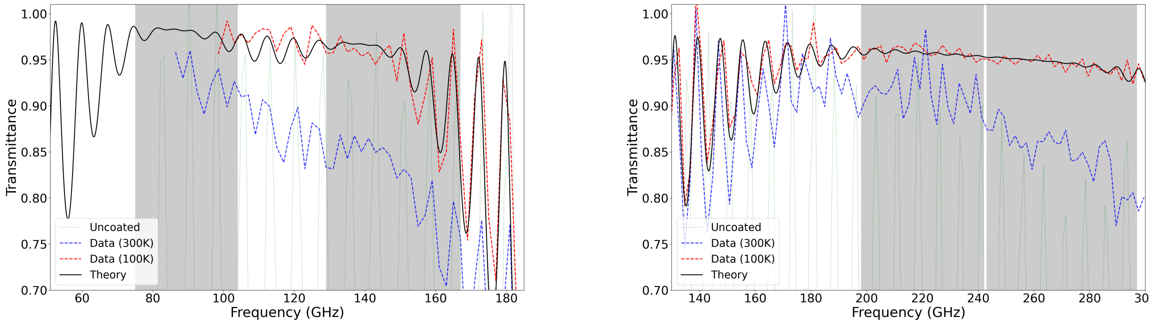

Figure 5.21: Transmittance measurements of alumina samples coated for optimal performance at 95/150 GHz bands (*left*) and 220/280 GHz bands (*right*).

Fabrication Process

Using a plasma spray gun mounted on a robot manipulator, an object of complex geometry can be coated with high precision and accuracy. We program the robot manipulator to trace the surface of the aspheric lens with tight control of deposition angle and stand-off distance due to their strong influence on coating deposition rate and dielectric constant. During the robot programming and coating spray process, the target substrate is securely held using a fixture with the coating surface pointing normal to gravity. An example of a Simons Array lens on a spray fixture, used for the POLARBEAR-2b AR coating process, is shown in Figure 5.22.

The robot is programmed to move in a raster scan pattern of 3 mm step size throughout each spray pass. The dielectric constant has a strong dependence on step size, thus this value is fixed during the fabrication process. For each raster scan line, the robot measures the height of the lens surface at three locations: two at the edge of the optical surface and one at the center corresponding to the highest point. These values are used by the manipulator system to define a circular arc through these points which the robot traverses at a constant speed. This allows the plasma gun to spray along the raster scan at a constant stand-off distance. Furthermore, the manipulator system adjusts the angle of the gun to be normal to the arc of the raster scan to maintain a spray angle within ±10° of the normal vector to the lens surface, which is within acceptable tolerance for uniform deposition rate and maximal adhesion strength [47][22][16]. While it is possible to adjust the angle of the gun along the axis perpendicular to the raster scan line for many manipulator systems, the additional memory and programming time required made it unfeasible for this dissertation. Turnaround points are placed far from the edge points in order to maintain uniform deposition rate over the coated optical surface. Figure 5.27 in Section 5.5 shows measurements of achieved thickness uniformity of a two-layer AR coating, made using a CMM. The coating of solid alumina powder achieves greater uniformity of ±7 μm while that of alumina microsphere and solid

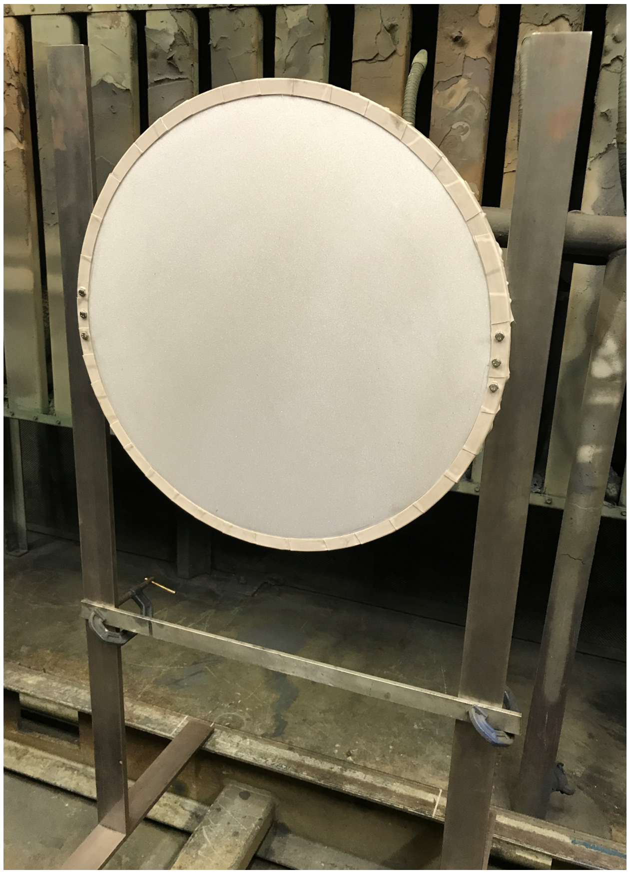

Figure 5.22: POLARBEAR-2b lens spray coated on a fabrication fixture.

powder matrix achieves uniformity of ±10 μm, both within acceptable tolerance for less than 1% reflectance for a single optical element, coated on both sides as shown in Figure 5.4.

The preparation and spray fabrication process requires a dry environment due to the effect of water vapor on the powder flow of the feed system [61] and measured dielectric constant of the coating [17]. To prevent disruption of smooth powder injection into the plasma, the powder matrix is baked for 2 hours at 130 °C and kept from exposure to humid environments. As [17] shows the trapping of water vapor in high humidity environments artificially increasing the dielectric constant of alumina-based coatings, a dehumidifier is continuously operated to reduce relative humidity below 40% or lower.

Atmospheric plasma spray equipment systems, available in most commercial vendor facilities, can adopt this technology due to the standard nature of its spray process. Any generic system can be utilized with minor adjustments to the spray parameter array, especially to stand-off distance, powder feed-rate, and plasma power values, to produce comparable results.

5.5 SPT-3G AR Coating

SPT-3G observes three bands - 90, 150, and 220 GHz - simultaneously and thus needs a three-layer AR coating for sufficient passband coverage. We detail the development and fabrication of the SPT-3G AR coating, for which I utilized plasma spray for the bottom two layers and assisted collaborators at University of Illinois at Urbana-Champaign to glue the PTFE top layer.

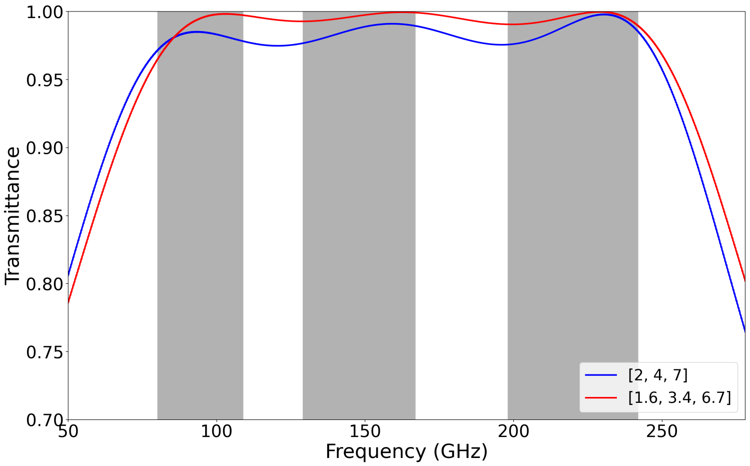

Figure 5.23: Theoretical transmittance spectra of alumina AR coatings for sub-optimal, where top layer is fixed at ϵ=2.0 (*blue*), and optimal (*red*) performance at 90/150/220 GHz bands.

Configuration	**Top layer**		**Middle layer**		**Bottom layer**		**Reflectance (%)**
	ϵ	t (μm)	ϵ	t (μm)	ϵ	t (μm)	
Sub-optimal	2.0	317	4.0	234	7.0	184	1.4
Optimal	1.64	352	3.45	243	6.75	179	0.6

Table 5.3: SPT-3G AR coating design parameters and reflectance performance

Based on the work of [10], the baseline design targeted a stack of dielectric constants $\epsilon = \{2, 4, 7\}$ using Stycast epoxy, whose theoretical transmittance is shown in Figure 5.23 and Table 5.3. However, due to its prohibitively high absorption loss, plasma spray AR coating described in Section 5.4 was chosen as the baseline technology. As dielectric constant values below 2.7 were inaccessible at this time, before the introduction of hollow silica microspheres into the set of powders, as outlined in Section 5.4, we chose a hybrid solution using PTFE, a

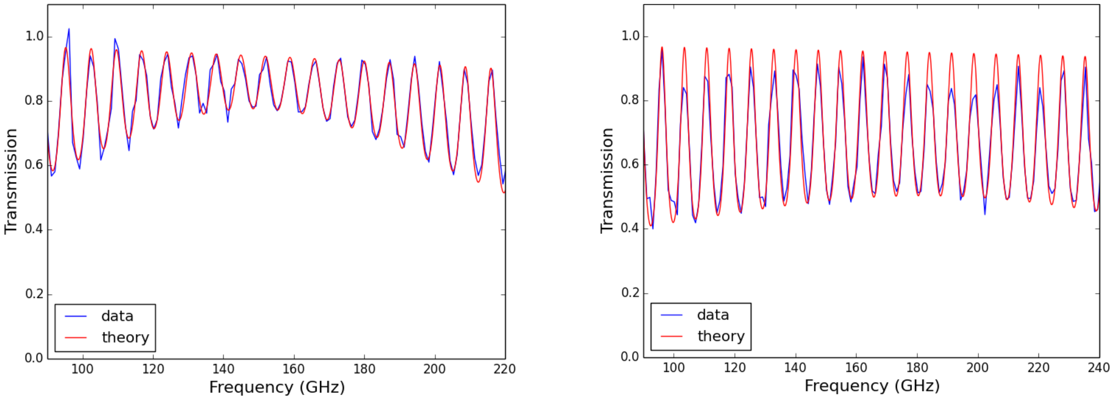

Figure 5.24: Measured FTS transmittance spectra and fit of alumina samples coated on one side with $\epsilon = 4$ (*left*) and $\epsilon = 7$ (*right*).

fluoropolymer with $\epsilon = 2$ [45], as the top layer and plasma sprayed coatings for the bottom two layers. The middle layer with $\epsilon = 4.0$ is produced using a 89:11 formulation of HAI microspheres and Metco powder, respectively. The bottom layer of $\epsilon = 7.0$ is produced by spraying Metco powder with higher value of injected plasma power. FTS measurements and fits are shown in Figure 5.24. Note that this coating stack was chosen as the baseline design rather than the more optimal stack, as seen in Table 5.3, due to prior development of fabrication techniques with $\epsilon = 2.0$ top layer. Using this set of dielectrics, we fabricated a three-layer AR coating on a 51 mm alumina coupon and measured its transmittance using the FTS at ambient and cryogenic temperatures, shown in Figure 5.25.

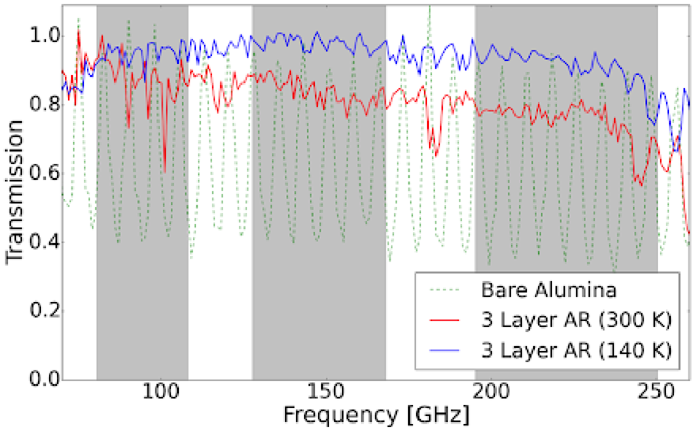

Figure 5.25: Transmittance measurements of alumina samples coated for sub-optimal performance at 90/150/220 GHz bands.

Figure 5.26: Curved fixture for large-scale thickness deposition uniformity testing on alumina coupons.

We first demonstrated the thickness accuracy and precision on a mock aluminum collimator lens, achieving 203 ± 11 μm for a target thickness of 203 μm. To further validate uniform deposition on an alumina surface, we demonstrated the accuracy and precision on a fixture setup shown in Figure 5.26. This fixture holds 9 alumina coupons in place in an orientation which replicates the radius of curvature of the SPT-3G aperture lens. The thickness of the alumina coupons was measured before and after coating at two opposite ends of each coupon, achieving 145 ± 5 μm for a target thickness of 152 μm.

Due to failure of thermal cycle tests of this PTFE top-layer design with numerous variations of alumina surface roughness, we explored the option of using expanded PTFE (ePTFE) as the top layer. Zitex ePTFE[12] contains pores of 1 - 6 μm size with a wide range of total porosity, a tracer for dielectric constant just as ratio of hollow microspheres tune the dielectric constant for plasma spray coatings. A 1.2 g/cc density sheet is calculated to be characterized by dielectric constant $\epsilon = 1.64$ based on effective medium theory, given by

$$\epsilon_{\text{eff}} = \epsilon_m \frac{2\delta_i(\epsilon_i - \epsilon_m) + \epsilon_i + 2\epsilon_m}{2\epsilon_m + \epsilon_i - \delta_i(\epsilon_i - \epsilon_m)} \tag{5.12}$$

where ϵ_{eff} is the effective dielectric constant of the medium, ϵ_m is of the matrix, and ϵ_i is of the inclusion. In combination with the re-optimized set of three-layer stack of $\epsilon = \{1.6, 3.4, 6.7\}$ generates a more optimal passband for SPT-3G observation bands, as seen in Figure 5.23 and Table 5.3. This ePTFE top layer AR stack demonstrated robustness to cryogenic delamination as two 152 mm diameter alumina discs, coated with this AR stack, survived five thermal cycles via dunking in liquid nitrogen (LN2).

---

[12] https://www.films.saint-gobain.com/products/chemfilm/microporous-ptfe

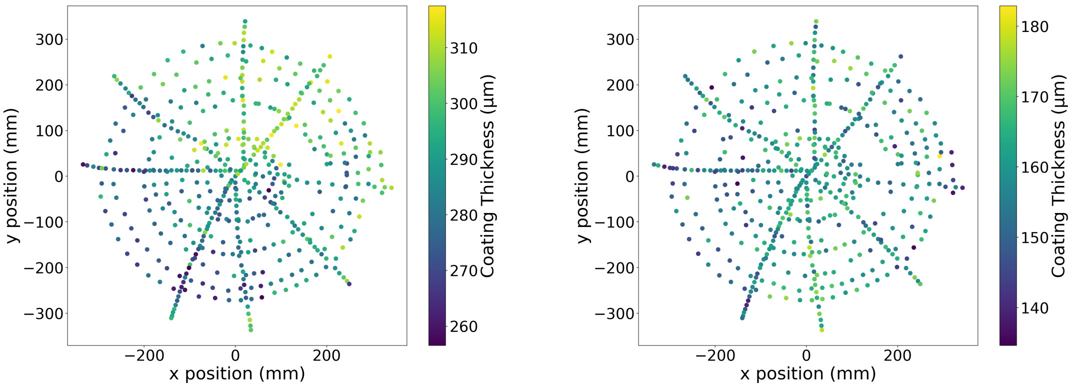

Figure 5.27: CMM measurements of the SPT-3G aperture lens curved-side $\epsilon = 4$ (*left*) and $\epsilon = 7$ (*right*) AR coating thicknesses.

We coated the window backing plate (WBP) and re-imaging lenses of SPT-3G between June to September 2016. Collaborators at University of Illinois at Urbana-Champaign laminated the ePTFE layers using low density polyethylene (LDPE) glue layer inside an oven-press assembly [3] and diced stress-relief grooves of 25.4 mm pitch using dicing blades. Upon final cooling stress tests for cryo-mechanical robustness, the differential CTE from the ePTFE laminate caused delamination and within the time constraints of South Pole deployment, the WBP and lenses were re-coated sans the top ePTFE layer. Figure 5.27 shows representative CMM contour plots of plasma sprayed coating layer thicknesses and Table 5.4 lists all measured thicknesses and uncertainties. The thickness measurements were made using a combination of CMM and indicator, detailed in Section 5.6, on the lenses and on a companion witness coupon using a micrometer. The lenses and SPT-3G instrument deployed in the winter of 2016 and achieved first light in January 2017 [12][2].

Lens	**Bottom Layer** (μm)		**Top Layer** (μm)	
	Side 1	Side 2	Side 1	Side 2
Design	179		243	
Field	160±8	178±5	290±13	246±15
Aperture	170±8	173±8	284±13	254±13
Collimator	183±10	180±8	279±15	254±13

Table 5.4: Measured thicknesses on the SPT-3G lenses. Side 1 indicates the curved side of the lens.

5.6 POLARBEAR-2b AR Coating

Due to the cryogenic delamination of epoxy-coated POLARBEAR-2b re-imaging lenses, plasma spray AR coating rapidly underwent large format validation in order to meet a tight deployment schedule. We sprayed the Omya silica microsphere top layer on a mock aluminum field lens surface to demonstrate large format thickness accuracy and precision. CMM metrology, as shown in Figure 5.28, showed a thickness of 343 ± 23 μm for a target thickness of 330 μm, which was determined to meet the tolerance requirement set by Figure 5.4. Using the process described in Sections 5.4, we fabricated the POLARBEAR-2b lens AR coatings using the plasma spray AR coating technology between February and March 2020 before COVID-19 shutdowns halted further work.

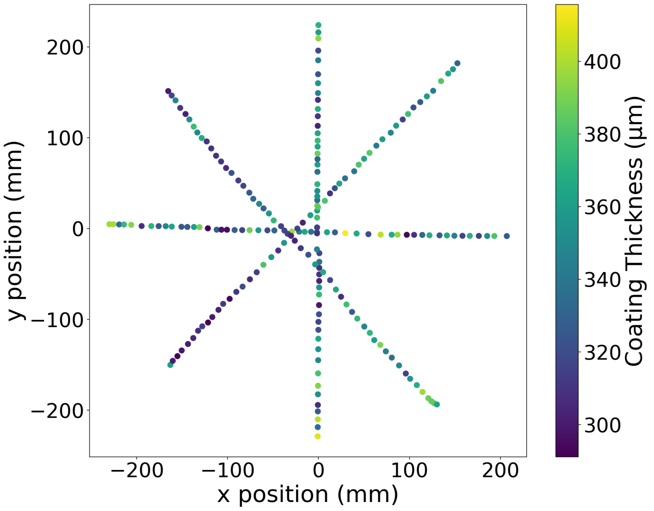

Figure 5.28: Measured thickness of silica $\epsilon = 2$ coating on an aluminum mock Simons Array field lens.

In the interest of time and given the evidence from the SPT-3G AR fabrication of thickness precision and accuracy in 2016, CMM measurements of coating thickness were replaced with the short turnaround indicator measurements. For curved surfaces, a single measurement is made at the zenith before and after coating, as shown in Figure 5.29. These measurements were verified to be accurate by micrometer measurements of un-adhered [13] chip pieces on the lens flange. For flat surfaces, indicator measurements were made at the edge of coated surfaces in reference to uncoated, adjacent flange point at 0°, 120°, and 240°. The indicator was additionally moved across the coating surface for flatness measurements. We present the achieved coating thickness of every POLARBEAR-2b lens in Table 5.5. The curved

---

[13] Flange is purposefully not grit blasted to prevent coating adhesion

Figure 5.29: Curved surface indicator measurement on a granite table of a POLARBEAR-2b lens.

surface of the collimator lens was coated, then stripped due to an operator error resulting an additional, single raster scan of spray and a strip of ∼25 μm greater thickness. The listed thickness is of the coating prior to removal. COVID-19 shutdowns prevented re-coating of this surface and POLARBEAR-2b deployed in summer 2021 with a newly plastic-Mullite coated collimator lens. As of this writing, we are assembling these lenses within the receiver cryostat at the site.

Lens	**Bottom Layer** (μm)		**Top Layer** (μm)	
	Side 1	Side 2	Side 1	Side 2
Design	267		483	
Field	267	267	470	483
Aperture	294	241 - 267	521	508 - 546
Collimator	267	241 - 267	495	495 - 508

Table 5.5: Measured thicknesses on the POLARBEAR-2b lenses. Side 1 indicates higher curvature side of the lens.[14]

---

[13] The listed values for the collimator lens are prior to abrasive grit blast stripping.

5.7 UHMWPE Window AR Coating

We measure the UHMWPE to have a dielectric constant $\epsilon = 2.301$ as shown in Figure 5.30. Its relatively smaller value and resulting smaller Fabry-Perot fringe amplitude allows a single-layer AR coating to be implemented for dual-band observations, preventing $\sim$ 4% power reflections per two bare surfaces. We present the parameters and resulting reflectance and transmittance spectra of the optimized Simons Array AR coating designs in Table 5.6 and Figure 5.31. Following the prior demonstration of the SPIDER [51] and QUIET experiments [32], we choose ePTFE as the AR coating material for the UHMWPE window. Using Equation 5.12, the density value of ePTFE is calculated for the optimal dielectric constant shown in Table 5.6. The POLARBEAR-2b calculation shows reflection suppressed to below 5% over 114% fractional bandwidth for 2% and 0.4% band-averaged reflectance at 95 and 150 GHz, and POLARBEAR-2c calculation shows reflection suppressed to below 5% over 88% fractional bandwidth for 0.4% and 0.3% band-averaged reflectance at 220 and 280 GHz.

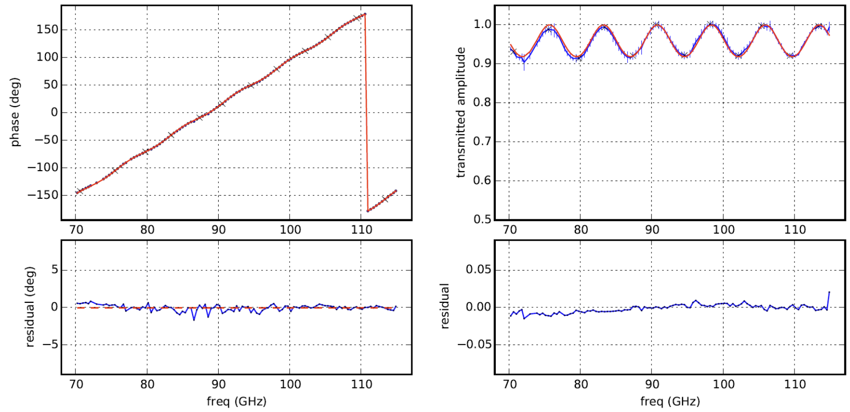

Figure 5.30: Transmittance spectrum measurement and fit of UHMWPE, courtesy of Richard Plambeck.

Passband	**Coating**		**Reflectance (%)**
	ϵ	thickness (μm)	
95/150 GHz	1.50	475	1.2
220/280 GHz	2.04	210	0.3

Table 5.6: Simons Array UHMWPE AR coating design parameters and reflectance performance.

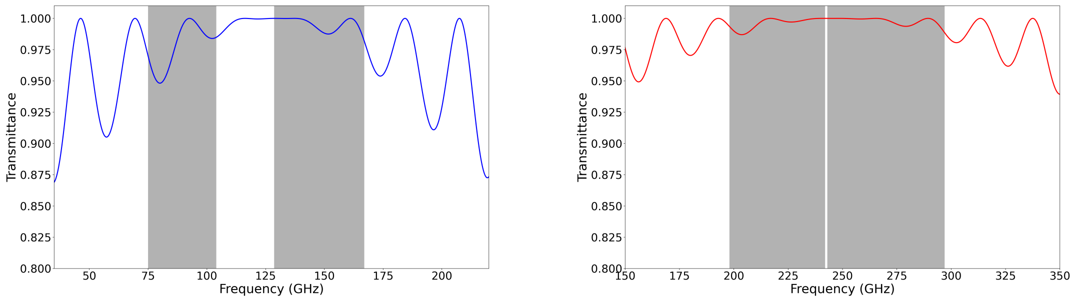

Figure 5.31: Optimized transmittance spectra of UHMWPE AR coating for 95/150 GHz bands (*left*) and 220/280 GHz bands (*right*).

Performance

We sanded ePTFE sheets to optimal thicknesses and glued them to 150 mm UHMWPE plates for Simons Array observation bands, using a vacuum-press process described in Section 5.7. We measured the transmittance spectra of these samples using the FTS, as shown in Figure 5.32.

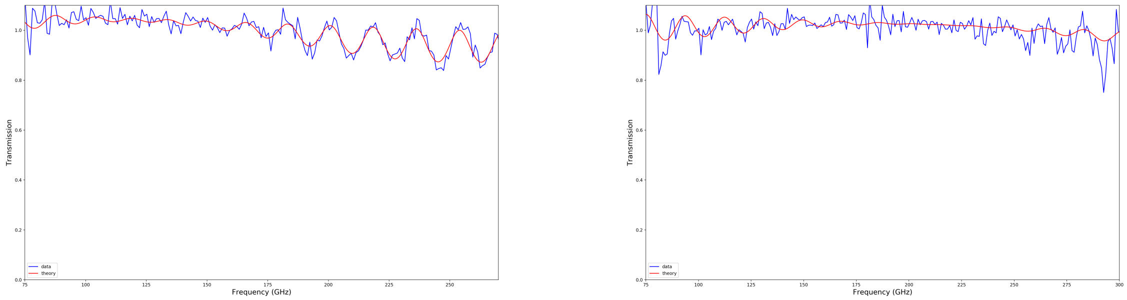

Figure 5.32: Transmittance measurements of UHMWPE samples coated for optimal performance at 95/150 GHz bands (*left*) and 220/280 GHz bands (*right*)

Fabrication Process

We developed a vacuum-press process inside an oven [38] to adhere the ePTFE sheet onto the UHMWPE plate by melting solely the thin LDPE glue layers and providing uniform pressure on the dielectric stack via silicone sheets. First, these dielectric layers are prepared for mechanical adhesion. An orbit sander loaded with 120 grit silicon carbide sandpaper is used to uniformly roughen the UHMWPE plate surfaces for mechanical bonding. The roughened UHMWPE is placed on a precision granite surface plate and a dial indicator is used to measure global parallellism and local non-uniformities. The ePTFE sheets are sanded in a more arduous and complex process. Due to commercial ePTFE sheets being available in discrete values of thickness that significantly differ from optimal thickness, they must be sanded in a precise and accurate manner. 3M double-sided removable tape[15] strips are placed on the same granite surface plate used for UHMWPE sanding in a manner that covers the entire surface without any overlaps and an ePTFE sheet is laid flush against the taped surface. This tape allows the ePTFE to remain static and stable through the sanding process and subsequently be easily removed without any damage to the adhered surface. Large gaps between strips of tape lead to pockets of air underneath the ePTFE and overlaps of strips of tape lead to an uneven ePTFE surface. A uniformly flat surface of ePTFE, which is parallel with the precision granite surface, is necessary for a precise and accurate sanding procedure. The ePTFE is abraded by moving a combination of 220 and 320 grit aluminum oxide sand paper across the sheet in large, even motions. The dial indicator is used to frequently inspect the thickness and uniformity of the sheet.

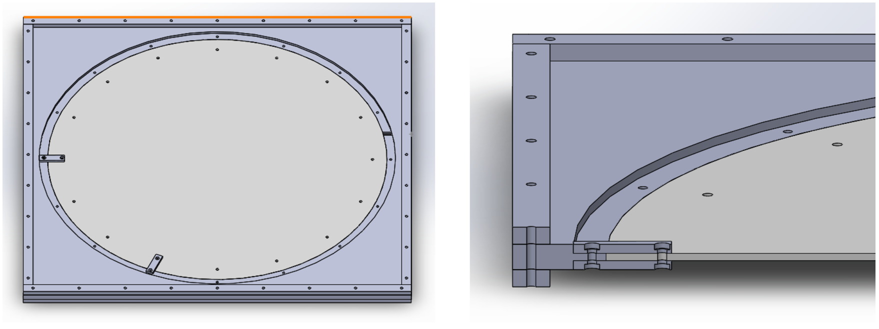

Figure 5.33: Vacuum press assembly CAD

The UHMWPE and ePTFE dielectric layers are stacked within the vacuum-press assembly, shown in Figure 5.33. This assembly consists of a metal aperture where the window dielectric stack is placed and secured using radial clamps. Transparent silicone sheet are placed on both sides of the aperture and window stack and clamped using bars running across the entire edge of silicone sheet. A vacuum pump is connected to a KF port which leads to the aperture and pulls the silicone sheets flush against the window assembly surfaces. 12 μm thick LDPE sheets are placed between the UHMWPE plate and ePTFE sheet which act as glue layers when melted and cooled, allowing the LDPE to fill in the micro roughness of the dielectric layers and mechanically adhere them upon cooling.

Table 5.7 shows the melting point of the layers of the window dielectric stack. Since the oven must completely and solely melt the LDPE without melting the UHMWPE plate, the oven temperature requirement is set to 125 °C with a uniformity of ±5 °C over the UHMWPE

---

[15] https://www.3m.com

Dielectric layer	Melting temperature (°C)
PTFE	327
LDPE	105 - 115
UHMWPE	130 - 135

Table 5.7: Plastic melting points

diameter. The oven is turned on and its temperature linearly ramped up to 125 °C over 20.5 hours. This temperature is held for 10 hours and then linearly ramped down to room temperature for 10.25 hours. When the window is cooled down to room temperature, the ePTFE AR coating should be adhered with a thin, uniform layer of LDPE glue.

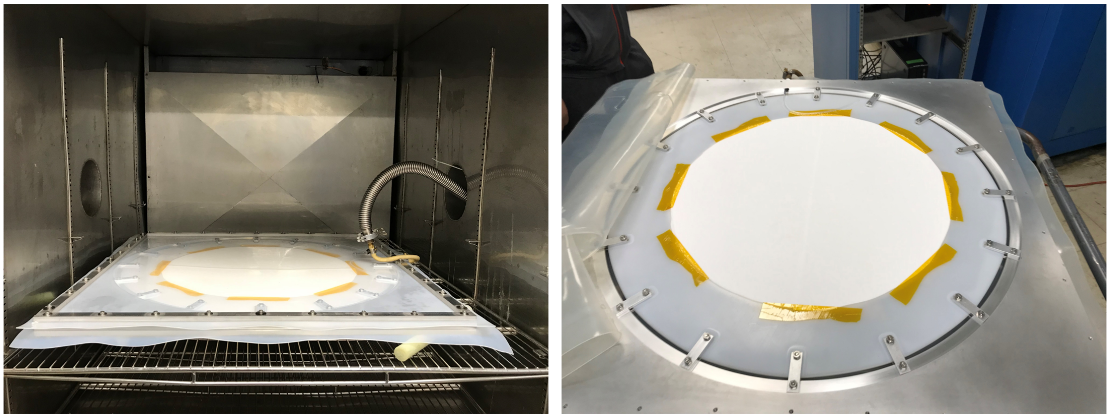

Figure 5.34: Vacuum press process[16]

Figure 5.34 shows the fabrication process of a Simons Array window. Due to limitations in width of commercially available ePTFE sheets, each ePTFE layer consists of two halves with an overlap, where the overlap is cut away post-fabrication using a razor blade.

---

[16] http://www.quantalabs.com

Chapter 6

Conclusion

We detail the development of the Simons Array cryogenic optics, aimed at broadband observations of the CMB polarization anisotropies with high fidelity and high optical throughput. Simons Array occupies a unique position among other modern CMB polarimeters, observing both at small angular scales of gravitational lensing of the CMB and large angular scales of the primordial B-mode at the recombination bump. It utilizes three multichroic receivers with observation bands centered at 95, 150, 220, and 280 GHz, focusing its sensitivity at 95 and 150 GHz channels where the ratio between the CMB and foreground emission signal is largest, and additionally providing polarized dust emission channels at 220 and 280 GHz. Its first receiver, POLARBEAR-2a, observes at 95 and 150 GHz and achieved first light in early 2019. POLARBEAR-2b observes at 95 and 150 GHz and POLARBEAR-2c at 220 and 280 GHz.

Chapter 4 describes the end-to-end development of the POLARBEAR-2b and POLARBEAR-2c optics tubes, from production and characterization of the optical elements to the production and cryogenic validation of the cryostats. The goal of detecting the faint primordial B-mode signal requires an increasingly sensitive millimeter receiver, achieved by increasing the optical throughput and consequently the focal plane size to accommodate a larger detector count. Alumina refractive elements are utilized to couple the telescope to the large detector count and focal plane of a Simons Array receiver. This large focal plane requires fast and large-format optics, carefully designed to minimize the effects of aberrations for two simultaneous observation bands over the entire focal plane. The optical chain of this receiver consists of multiple stages of thermal filtering to minimize radiative loading on the millikelvin focal plane and optical loading on the photon-noise limited detectors. The optics are cooled using a two-stage PTC where its 4 K stage anchors its beam-defining aperture stop and re-imaging lenses. We measured the dielectric properties and aspheric profile of each lens to evaluate the optical performance of each receiver based on measured properties, and subsequently re-optimize the optics. In conjunction, we machined the vacuum and cryogenic shells of the optics tubes and fabricated the remaining optical elements, improving the design of the Lyot stop and the POLARBEAR-2c vacuum window. We assembled these sets of optics tube hardware and carried out a series of cryogenic tests to their required temperatures. After integrating the POLARBEAR-2b receiver in UC San Diego, we are currently in the process of assembling it at the site for integration with its telescope. The POLARBEAR-2c receiver awaits lab commissioning at UC Berkeley.

Modern CMB experiments must characterize and subtract galactic foreground signal from CMB polarization signal, requiring multichroic observation with broadband optics. This presents an engineering challenge to produce a large format, multi-layer AR coating which demonstrates high optical efficiency and robustness against cryogenic delamination. This dissertation advances the broadband AR coating technologies of CMB optics. In Chapter 5, we detail these technologies which are based on the principles of the quarter-wave impedance transformer and their applications to Simons Array and SPT-3G alumina optics. Between 2014 and 2016, we worked with the UC Berkeley Machine Shop to develop a two-layer epoxy-based AR coating fabrication procedure for the POLARBEAR-2a alumina lenses. We designed and implemented a process which coats the lens surface by lowering it onto a negative mold containing Stycast and machines the cured epoxy to a precise and accurate shape. We also developed the novel, broadband plasma spray AR coating technology for application on cryogenic millimeter-wave optics. This technology provides a powerful AR coating solution for CMB experiments with its wide range of accessible dielectric constants, low loss coatings, ability to accurately and precisely spray coatings on complex surface profiles, and robustness against cryogenic delamination from alumina and silicon optics. It saw first application on the SPT-3G lenses, which deployed in winter 2016 for fight light in January 2017. Upon cryogenic delamination of the two-layer epoxy-based AR coating on the POLARBEAR-2b lenses, just a few months before scheduled deployment, we plasma spray coated the lenses. Due to recent advancements in expanding the achievable dielectric constant down to $\epsilon = 2.04$ for the top layer of multi-layer AR coating designs, this technology was applied in an end-to-end process. The lenses were coated in spring 2020 and deployed to the site for installation in its receiver.

With the POLARBEAR-2b receiver assembly expected to be complete for first light in October 2021, installation of the receiver on the telescope will soon follow and calibration will ensue to verify proper operation of all subsystems. We look forward to POLARBEAR-2b joining POLARBEAR-2a in making science observations and POLARBEAR-2c achieving lab commissioning and deployment to complete the Simons Array.

Bibliography

[1] A. Bender et al. “Digital frequency domain multiplexing readout electronics for the next generation of millimeter telescopes”. In: *Millimeter, Submillimeter, and Far-Infrared Detectors and Instrumentation for Astronomy VII* 9153 (July 2014). arXiv:1407.3161. DOI: `10.1117/12.2054949`.

[2] A. N. Bender et al. “Year two instrument status of the SPT-3G cosmic microwave background receiver”. In: *Millimeter, Submillimeter, and Far-Infrared Detectors and Instrumentation for Astronomy IX* 10708 (Aug. 2018). DOI: `10.1117/12.2312426`.

[3] A. Nadolski et al. “Broadband anti-reflective coatings for cosmic microwave background experiments”. In: *Millimeter, Submillimeter, and Far-Infrared Detectors and Instrumentation for Astronomy IX* 10708 (July 2018). arXiv:1809.00030v1. DOI: `10.1117/12.2315674`.

[4] B. Westbrook et al. “The POLARBEAR-2 and Simons Array Focal Plane Fabrication Status”. In: *Journal of Low Temperature Physics* 193 (Sept. 2018). DOI: `10.1007/s10909-018-2059-0`.

[5] C. Hill et al. “A cryogenic continuously rotating half-wave plate mechanism for the POLARBEAR-2b cosmic microwave background receiver”. In: *Review of Scientific Instruments* 91.124503 (Dec. 2020). arXiv:2009.03972v2. DOI: `10.1063/5.0029006`.

[6] C. Hill et al. “Design and development of an ambient-temperature continuously-rotating achromatic half-wave plate for CMB polarization modulation on the POLARBEAR-2 experiment”. In: *Millimeter, Submillimeter, and Far-Infrared Detectors and Instrumentation for Astronomy VIII* 9914 (July 2016). arXiv:1607.07399v1. DOI: `10.1117/12.2232280`.

[7] C. Patrignani et al. “Review of Particle Physics”. In: *Chinese Physics C* 40.10 (2016). DOI: `10.1088/1674-1137/40/10/100001`.

[8] D. J. Fixsen et al. “The Cosmic Microwave Background Spectrum from the Full COBE FIRAS Data Set”. In: *Astrophysical Journal* 473.2 (Dec. 1996), pp. 576–587. DOI: `10.1086/178173`.

[9] D. Kaneko et al. “Deployment of POLARBEAR-2A”. In: *Journal of Low Temperature Physics* 199 (Dec. 2020), pp. 1137–1147. DOI: `10.1007/s10909-020-02366-w`.

[10] D. Rosen et al. “Epoxy-based broadband antireflection coating for millimeter-wave optics”. In: *Applied Optics* 52.33 (Nov. 2013). arXiv:1307.7827v1, pp. 8102–8105. DOI: `10.1364/AO.52.008102`.

[11] H. Aihara et al. “The Hyper Suprime-Cam SSP Survey: Overview and survey design”. In: *Publications of the Astronomical Society of Japan* 70.SP1 (Sept. 2017). arXiv:1704.05858v3. DOI: `10.1093/pasj/psx066`.

[12] J. A. Sobrin et al. “Design and characterization of the SPT-3G receiver”. In: *Millimeter, Submillimeter, and Far-Infrared Detectors and Instrumentation for Astronomy IX* 10708 (Aug. 2018). arXiv:1809.00032v1. DOI: `10.1117/12.2314366`.

[13] J. Choi et al. “Radio-transparent multi-layer insulation for radiowave receivers”. In: *Review of Scientific Instruments* 84.114502 (Oct. 2013). arXiv:1306.5040. DOI: `10.1063/1.4827081`.

[14] J. Molla et al. “Dielectric property measurement system at cryogenic temperature and microwave frequencies”. In: *IEEE Transactions on Instrumentation and Measurement* 42.4 (Aug. 1993), pp. 817–821. DOI: `10.1109/19.234491`.

[15] K. N. Abazajian et al. “Neutrino physics from the cosmic microwave background and large scale structure”. In: *Astroparticle Physics* 63 (Mar. 2015). arXiv:1309.5383v3, pp. 66–80. DOI: `10.1016/j.astropartphys.2014.05.0145`.

[16] M. F. Bahbou et al. “Effect of grit blasting and spraying angle on the adhesion strength of a plasma-sprayed coating”. In: *Journal of Thermal Spray Technology* 13.4 (Dec. 2004), pp. 508–514. DOI: `10.1361/10599630421406`.

[17] M. Niittymäki et al. “Effect of temperature and humidity on dielectric properties of thermally sprayed alumina coatings”. In: *IEEE Transactions on Dielectrics and Electrical Insulation* 25.3 (June 2018), pp. 908–918. DOI: `10.1109/TDEI.2018.006892`.

[18] M. Tristram et al. “Planck constraints on the tensor-to-scalar ratio”. In: *Astronomy and Astrophysics* 647.A128 (Mar. 2021). arXiv:2010.01139. DOI: `10.1051/0004-6361/202039585`.

[19] N. Stebor et al. “The Simons Array CMB Polarization Experiment”. In: *Millimeter, Submillimeter, and Far-Infrared Detectors and Instrumentation for Astronomy VIII* 9914 (July 2016). DOI: `10.1117/12.2233103`.

[20] P. Ade et al. “The Simons Observatory: science goals and forecasts”. In: *Journal of Cosmology and Astroparticle Physics* 056 (Feb. 2019). arXiv:1808.07445v2. DOI: `10.1088/1475-7516/2019/02/056`.

[21] P. Siritanasak et al. “The Broadband Anti-reflection Coated Extended Hemispherical Silicon Lenses for POLARBEAR-2 Experiment”. In: *Journal of Low Temperature Physics* 184 (Dec. 2015), pp. 553–558. DOI: `10.1007/s10909-015-1386-7`.

[22] S. Houdková et al. “The Influence of Spraying Angle on Properties of HVOF Sprayed Hardmetal Coatings”. In: *Journal of Thermal Spray Technology* 19.5 (Sept. 2010), pp. 893–901. DOI: `10.1007/s11666-010-9514-z`.

[23] S. Takakura et al. “Performance of a continuously rotating half-wave plate on the POLARBEAR telescope”. In: *Journal of Cosmology and Astroparticle Physics* 2017 (May 2017). arXiv:1702.07111. DOI: `10.1088/1475-7516/2017/05/008`.

[24] Y. Inoue et al. “Cryogenic infrared filter made of alumina for use at millimeter wavelength”. In: *Applied Optics* 53.9 (Mar. 2014). arXiv:1311.5388v4, pp. 1727–1733. DOI: `10.1364/AO.53.001727`.

[25] Y. Inoue et al. “Two-layer anti-reflection coating with mullite and polyimide foam for large-diameter cryogenic infrared filters”. In: *Applied Optics* 55.34 (Sept. 2016). arXiv:1607.02938v2, pp. D22–D28. DOI: `10.1364/AO.55.000D22`.

[26] Z. Ahmed et al. “BICEP3: a 95GHz refracting telescope for degree-scale CMB polarization”. In: *Millimeter, Submillimeter, and Far-Infrared Detectors and Instrumentation for Astronomy VII* 9153 (Aug. 2014). arXiv:1407.5928v1. DOI: `10.1117/12.2057224`.

[27] A. Albrecht and P. J. Steinhardt. “Cosmology for Grand Unified Theories with Radiatively Induced Symmetry Breaking”. In: *Physical Review Letters* 48.1220 (Apr. 1982). DOI: `10.1103/PhysRevLett.48.1220`.

[28] Planck Collaboration. “Planck 2015 results. X. Diffuse component separation: Foreground maps”. In: *Astronomy and Astrophysics* 594.A10 (Oct. 2016). arXiv:1502.01588. DOI: `10.1051/0004-6361/201525967`.

[29] Planck Collaboration. “Planck 2018 results. I. Overview and the cosmological legacy of Planck”. In: *Astronomy and Astrophysics* 641.A1 (Sept. 2020). arXiv:1807.06205v2. DOI: `10.1051/0004-6361/201833880`.

[30] Planck Collaboration. “Planck 2018 results. VI. Cosmological parameters”. In: *Astronomy and Astrophysics* 641.A6 (Sept. 2020). arXiv:1807.06209v3. DOI: `10.1051/0004-6361/201833910`.

[31] Planck Collaboration. “Planck 2018 results. XI. Polarized dust foregrounds”. In: *Astronomy and Astrophysics* 641.A11 (Sept. 2020). arXiv:1801.04945. DOI: `10.1051/0004-6361/201832618`.

[32] QUIET Collaboration. “THE Q/U IMAGING EXPERIMENT INSTRUMENT”. In: *Astrophysical Journal* 768.1 (May 2013). arXiv:1207.5562v2. DOI: `10.1088/0004-637X/768/1/9`.

[33] The POLARBEAR Collaboration. “The Hyper Suprime-Cam SSP Survey: Overview and survey design”. In: *Astrophysical Journal* 848.73 (Oct. 2017). arXiv:1403.2369v3. DOI: `10.1088/0004-637X/794/2/171`.

[34] S. Cortiglioni and T. A. T. Spoelstra. “The limitations of cosmic-microwave-background measurements due to linear polarization of galactic radio emission”. In: *Astronomy and Astrophysics* 302 (1995).

[35] R. H. Dicke et al. “Cosmic Black-Body Radiation”. In: *Astrophysical Journal* 142.1 (July 1965), pp. 414–419. DOI: `10.1086/148306`.

[36] B. T. Draine and A. Lazarian. “Magnetic dipole microwave emission from dust grains”. In: *Astrophysical Journal* 512.2 (Feb. 1999). arXiv:astro-ph/9807009, pp. 740–754. DOI: `10.1086/306809`.

[37] A. H. Guth. “Inflationary universe: A possible solution to the horizon and flatness problem”. In: *Physical Review D* 23.2 (Jan. 1981), pp. 347–356. DOI: `10.1103/PhysRevD.23.347`.

[38] P. C. Hargrave and G. Savini. “Anti-reflection coating of large-format lenses for submm applications”. In: *Millimeter, Submillimeter, and Far-Infrared Detectors and Instrumentation for Astronomy V* 7741 (July 2010). DOI: `10.1117/12.856919`.

[39] E. Hubble. “A relation between distance and radial velocity among extra-galactic nebulae”. In: *Proceedings of the National Academy of Sciences of the United States of America* 15.3 (Mar. 1929). DOI: `10.1073/pnas.15.3.168`.

[40] Y. Inoue. “Development of POLARBEAR-2 receiver system for cosmic microwave background polarization experiment”. PhD dissertation. The Graduate University for Advanced Studies, 2016.

[41] O. Jeong et al. “Broadband plasma sprayed anti-reflection coating for millimeter-wave astrophysics experiments”. In: *Journal of Low Temperature Physics* 184 (Feb. 2016), pp. 621–626. DOI: `10.1007/s10909-015-1442-3`.

[42] O. Jeong et al. “Large-aperture broadband plasma spray anti-reflection coating technology for millimeter-wave astrophysics”. 2021.

[43] D. Kazanas. “Dynamics of the universe and spontaneous symmetry breaking”. In: *Astrophysical Journal* 241 (Oct. 1980), pp. L59–L63. DOI: `10.1086/183361`.

[44] M. M. Kreitman, T. Ashworth, and M. Rechowicz. “A correlation between thermal conductance and specific heat anomalies and the glass temperature of Apiezon N and T greases”. In: *Cryogenics* 12.1 (Feb. 1972), pp. 32–34. DOI: `10.1016/0011-2275(72)90134-8`.

[45] J. Lamb. “Miscellaneous data on materials for millimetre and submillimetre optics”. In: *International Journal of Infrared and Millimeter Waves* 17.12 (Dec. 1996), pp. 1996–2034. DOI: `10.1007/BF02069487`.

[46] G. Lemaître. “The Beginning of the World from the Point of View of Quantum Theory”. In: *Nature* 127.706 (May 1931). DOI: `10.1038/127706b0`.

[47] C.-J. Li et al. “Effect of Spray Angle on Deposition Characteristics in Cold Spraying”. In: *Thermal Spray 2003: Advancing the Science and Applying the Technology (ASM International)* (2003).

[48] A. D. Linde. “A new inflationary universe scenario: A possible solution of the horizon, flatness, homogeneity, isotropy and primordial monopole problems”. In: *Physics Letters B* 108.6 (Feb. 1982), pp. 389–393. DOI: `10.1016/0370-2693(82)91219-9`.

[49] F. Matsuda. “Cosmic Microwave Background Polarization Science and Optical Design of the POLARBEAR and Simons Array Experiments”. PhD dissertation. UC San Diego, 2017.

[50] Y. Minami and E. Komatsu. “New Extraction of the Cosmic Birefringence from the Planck 2018 Polarization Data”. In: *Physical Review Letters* 125.221301 (Nov. 2020). arXiv:2011.11254. DOI: `10.1103/PhysRevLett.125.221301`.

[51] J. Nagy. “Optical Development for the SPIDER Balloon-Borne CMB Polarimeter”. PhD dissertation. Case Western Reserve University, 2017.

[52] M. R. Otto. “Low-temperature characterization of dielectric loss at microwave frequencies in aluminum oxide”. Masters thesis. University of Waterloo, 2015.

[53] S. Paine. “The am atmospheric model (11.0)”. In: *Zenodo* (Sept. 2019). DOI: `10.5281/zenodo.3406483`.

[54] S. Pancharatnam. “Achromatic combinations of birefringent plates”. In: *Proceedings of the Indian Academy of Sciences - Section A* 41 (Apr. 1955), pp. 137–144. DOI: `10.1007/BF03047098`.

[55] Lord Rayleigh. “On reflection of vibrations at the confines of two media between which the transition is gradual”. In: *Proceedings of the London Mathematical Society* 11-12 (Feb. 1880), pp. 51–56.

[56] M. Rechowicz, T. Ashworth, and H. Steeple. “Heat transfer across pressed contacts at low temperatures”. In: *Cryogenics* 7.4 (Dec. 1967), pp. 369–370. DOI: `10.1016/S0011-2275(67)80122-X`.

[57] L. J. Salerno, P. Kittel, and A. L. Spivak. “Thermal Conductance of Pressed Metallic Contacts Augmented with Indium Foil or Apiezon-N Grease at Liquid Helium Temperatures”. In: *Cryogenics* 34.8 (1994), pp. 649–654. DOI: `10.1016/0011-2275(94)90142-2`.

[58] U. Seljak and M. Zaldarriaga. “Direct signature of an evolving gravitational potential from the cosmic microwave background”. In: *Physical Review D* 60.043504 (July 1999). arXiv:astro-ph/9811123v1. DOI: `10.1103/PhysRevD.60.043504`.

[59] U. Seljak and M. Zaldarriaga. “Signature of Gravity Waves in the Polarization of the Microwave Background”. In: *Physical Review Letters* 78.2054 (Mar. 1997). arXiv:astro-ph/9609169v2. DOI: `10.1103/PhysRevLett.78.2054`.

[60] N. J. Simon, E. S. Drexler, and R. P Reed. *Properties of Copper and Copper Alloys at Cryogenic Temperatures.* NIST Monograph 177, 1992.

[61] M. K. Stanford and C. DellaCorte. "Effects of humidity on the flow characteristics of a composite plasma spray powder". In: *Journal of Thermal Spray Technology* 15.1 (Mar. 2006), pp. 33–36. DOI: `10.1361/105996306X92550`.

[62] A. A. Starobinksy. "A new type of isotropic cosmological models without singularity". In: *Physics Letters B* 91.1 (Mar. 1980), pp. 99–102. DOI: `10.1016/0370-2693(80)90670-X`.

[63] A. Suzuki. "Multichroic Bolometric Detector Architecture for Cosmic Microwave Background Polarimetry Experiments". PhD dissertation. UC Berkeley, 2013.

[64] J. W. Waters. "Absorption and Emission by Atmospheric Gases". In: *Methods in Experimental Physics* 12B (1976), pp. 142–176. DOI: `10.1016/S0076-695X(08)60684-5`.

[65] A. A. Wilson and R. W. Wilson. "A Measurement of Excess Antenna Temperature at 4080 Mc/s". In: *Astrophysical Journal* 142.1 (July 1965), pp. 419–421. DOI: `10.1086/148307`.

[66] A. Woodcraft. "Predicting the thermal conductivity of aluminium alloys in the cryogenic to room temperature range". In: *Cryogenics* 45.6 (2004), pp. 421–432. DOI: `10.1016/j.cryogenics.2005.02.003`.

[67] A. Woodcraft. "Recommended values for the thermal conductivity of aluminium of different purities in the cryogenic to room temperature range, and a comparison with copper". In: *Cryogenics* 45.9 (2005), pp. 626–636. DOI: `10.1016/j.cryogenics.2005.06.008`.